THESIS

COMPUTER-AIDED ENGINEERING AND DESIGN OF INTERNAL COMBUSTION ENGINES TO SUPPORT OPERATION ON NON-TRADITIONAL FUELS

Submitted by

Miguel Valles Castro

Department of Mechanical Engineering

In partial fulfillment of the requirements

For the Degree of Master of Science

Colorado State University

Fort Collins, Colorado

Fall 2020

Master's Committee:

Advisor: Bret C. Windom

Anthony J. Marchese
Jeremy Daily

ABSTRACT

COMPUTER-AIDED ENGINEERING AND DESIGN OF INTERNAL COMBUSTION ENGINES TO SUPPORT OPERATION ON NON-TRADITIONAL FUELS

Traditional fuels like gasoline and diesel make up ~37 % of the US energy production; because of that, they are rapidly depleting their finite resources. These traditional fuels are also primary contributors to greenhouse gases, global warming, and particulate matter, which are bad for the environment and human beings. For that reason, research in non-traditional fuels (e.g., Carbon neutral biofuels, low GHG emitting gaseous fuels including NG and hydrogen) that achieve greater if not similar efficiencies compared to traditional fuels is gaining traction. On top of that, emission requirements are becoming even more strenuous. Engineers must find new ways to investigate non-traditional fuels and their performance in internal combustion engines while permitting the engine-fuel system's low-cost design. This being the case, Computer-Aided Engineering (CAE) tools like Computational Fluid Dynamics (CFD) and chemical kinetics solvers are being taken advantage of to assist in the research of these non-traditional fuel applications. This thesis describes the use of CONVERGE CFD to investigate two different non-traditional fuel applications, namely, the retrofitting of a premixed gasoline two-stroke spark-ignited (SI) engine to function with multiple injections of JP-8 fuel and to retrofit a diesel compression-ignited engine into a premixed anode tail-gas SI engine.

The first application described herein uses a solid oxide fuel cell “Anode Tail-gas,” which has similar syngas characteristics in a spark-ignited engine. Anode Tail-gas is a byproduct from

an underutilized Metal Supported Solid Oxide Fuel Cell (MS-SOFC) used in a high efficiency distributed power (~100 kWe) system. Gas turbines or reciprocating ICEs typically drive distributed power systems of this capacity because they can quickly react to change in demand but traditionally have lower thermal efficiencies than a large-scale Rankine cycle plant. However, with the MS-SOFC, it may be possible to design a 125 kWe system with 70 % efficiency while keeping the system cost-competitive (below $1000/kW). The system requires a ~14 kW engine that can operate at 35 % efficiency with the highly dilute (17.7% H2, 4.90 % CO, 0.40% CH4, 28.3 % CO_2, 48.7 % H_2O) Anode Tail-gas to meet these lofty targets. CAE approaches were developed and used to identify high-efficiency operation pathways with the highly diluted anode tail-gas fuel. The fuel was first tested and modeled in a Cooperative Fuel Research (CFR) engine to investigate the anode tail gas's combustibility within an IC engine and to provide validation data with highly specified boundary conditions (Compression Ratio (CR), fuel compositions, intake temperature/pressure, and spark timing). A chemical mechanism was selected through CAE tools to represent the highly diluted fuel combustion best based on the CFR data. Five experimental test points were used to validate the CFD model, which all were within a maximum relative error of less than 8 % for IMEP and less than 4 crank angle degrees for CA10 and CA50. The knowledge gained from the CFR engine experiments and associated model validation helped direct the design of a retrofitted Kohler diesel engine to operate as a spark-ignited engine on the anode tail gas fuel. CFD Investigations into spark plug and piston bowl designs were performed to identify combustion chamber design improvements to boost the Kohler engine's efficiency. Studies revealed that piston designs incorporating small clearance heights, large squish areas, and deep bowl depths could enhance efficiency by 5.41 pts with additional efficiency gain possible through piston rotation.

The second fuel investigation was a jet propellant fuel called “JP-8,” which was deemed non-tradition when used in a two-stroke UAV engine to satisfy the military’s single fuel policy requirements. The JP-8 fuel proved challenging in this application due to its significantly lower octane number and volatility than gasoline and experienced knock when used as a homogeneous premixed mixture within the simulated UAV platform. Although with CFD modeling, it was possible to reduce the severity of knock by using eight rapid direct injections of JP-8 at 20 μm diameter droplets. With further investigation, it might be possible to reduce further the severity of knock using CFD through more advanced injection strategies.

ACKNOWLEDGEMENTS

I would like to thank my academic advisor, Dr. Bret Windom, for giving me an opportunity to do research work during my undergraduate. Dr. Windom was always there to guide me and challenge me to make further discoveries in my research. I am beyond grateful to him for the tremendous support he has given me and the confidence he has had in me. I would also like to thank my committee members, Dr. Anthony Marchese, and Dr. Jeremey Daily, for their constant support and insightful suggestions during my research work.

I would also like to thank Alex Balu, Matthew Countie, Geet Padhi for their prior work on this project. A special thank you to Siddhesh Bhoite and Diego Bestel for their assistance in learning how to use CONVERGE CFD and always being willing to help bounce ideas off. Finally, I would like to thank my friends and family for always supporting me. A warm thank you to my mom for always working so hard to take care of me. She is the main reason I was able to make it this far in my life.

TABLE OF CONTENTS

LIST OF TABLES

Chapter 1: Introduction

1.1 Motivation and Overview

The United States utilized 105.7 EJ of energy in 2019, with 80.1% of that energy resulting from fossil fuel combustion converting the fuel's potential chemical energy into work for commercial, industrial, residential, or transportation use.[1] This stems from the incredible amount of potential energy tied into the chemical bonds that release heat upon combustion, which can be converted into mechanical work in internal combustion (IC) engines. For example, gasoline, a fossil fuel, has a potential energy of 43 MJ/kg; however, only about 30% of that energy might be used to power a vehicle, and the rest lost to exhaust, friction, and heat transfer. The second law of thermodynamics states that an isolated system cannot reduce the total entropy over time. Entropy is simply be defined as the energy required to arrange an isolated, non-reacting system of particles into their equilibrium state. [2] An IC engine has losses and generates entropy in the form of heat and friction that cannot be reduced or used to arrange the system of particles back into their equilibrium state. To that extent, Sadi Carnot showed that the most efficient cycle for an IC engine does not generate entropy; the Carnot equation demonstrates the maximum efficiency possible while considering thermodynamics' first and second laws. In an IC engine operating between 1750 and 298 K, the maximum efficiency possible is 83%, which was achieved using equation (1) where T_C and T_H are the coldest and hottest temperatures of an engine cycle, respectively.[2]

$$\eta = 1 - \frac{T_C}{T_H} * 100\% \quad (1)$$

That is why fossil fuels have been so popular because if a system's efficiency is limited, the only possible way to maximize useful energy is to select fuels with high potential energy levels. However, fossil fuels produce high greenhouse gas levels (GHG), oxides of nitrogen (NOx), and particulate matter (PM) emissions, which contribute to smog and directly impact human health. For this reason, The Environmental Protection Agency (EPA) regulated engine emissions based on the Clean Air Act and the Energy Policy.[3], [4] These emission regulations have become even more strenuous and more challenging to meet with current fuels/energy conversion devices. More efficient and fuel flexible energy conversion devices are needed to reduce emissions without compromising performance and safety.

For spark-ignited (SI) engines, high performance, high-efficiency energy conversion, and low emission operation are limited by avoiding engine knock. Engine knock is an abnormal combustion phenomenon in IC engines dependent on the chemical kinetics of the fuel and engine characteristics like compression ratio (CR), spark timing, and many more. If not addressed, engine knock could lead to engine failure and safety concerns.

System efficiency and safety optimized energy conversion strategies may require non-traditional fuels, such as low calorific waste fuel streams or low octane number fuels in SI engines. New engine design techniques are necessary to achieve more efficient and fuel flexible energy conversion devices. Computer-aid engineering (CAE) tools like computational fluid dynamics (CFD) and chemical kinetic solvers are rapidly gaining traction in the automotive and energy industries because of the ability to simulate engine performance while reducing cost and increasing experimental productivity. CAE tools have recently been able to accurately demonstrate combustion phenomena like engine knock to permit the design of engines to operate on the verge of unstableness to maximize performance and efficiency.

CAE tools with experimental data assistance are used to investigate two engine platforms powered by non-traditional fuels. The first includes the design of a JP-8 directed injected two-stroke UAV engine that is traditionally gasoline-powered. The second explored the SI engine's design to operate off a highly diluted low calorific value fuel called “anode tail-gas even though it was previously operated as a compression-ignited (CI) diesel engine. The general approach in the research and design of the updated engines included obtaining a better understanding of the non-traditional fuels (ignition delay and flame speeds) and then creating a baseline case to compare with all other cases.

The thesis structure will follow a typical scientific paper format of introduction, methods, results, discussion, and conclusion. This chapter was the first part of the introduction section, which will be continued in the next chapter with a deep dive into other research work to help understand the current state of some of the topics that will be investigated in this thesis. Chapter 3 will be a general breakdown of the CFD setup used to carry out the research work presented in this thesis. Chapters 4 and 5 will be broken down into sub-sections of background for the specific project followed by a more detailed specific methods section. The results will be presented, and finally, a conclusion section will summarize the key points for each specific section. Chapter 4 will be the beginning of the research conducted for the exhaust fuel from a solid oxide fuel cell to be used in an IC engine. Chapter 5 will focus on the work performed to retrofit a premixed spark-ignited two-stroke unmanned aerial vehicle (UAV) gasoline power engine into a rapid multi-spray injected powered JP-8. Chapter 6 will again summarize the results from chapters 4 and 5 in one place with any future work discussed in these chapters.

Chapter 2: Detailed Overview/Literature Review

2.1 Internal Combustion Engines

IC engines have been around for over a century now and have been a great energy production source. Over these many decades, IC engines have transformed tremendously. There are many different varieties and styles of engines to select from; however, thanks to Heywood et al., IC engines can be classified into ten categories.[5] Some of these categories are commonly heard of, like working cycle (two-stroke vs. four-stroke) or basic engine design (inline or V) and method of ignition (spark ignited vs. compression ignited).[5] Ultimately, the application of the engine decides what classification of the engine will be required.

2.1.1 Two-Stroke/Four-Stroke

One of the most common ways to classify an IC engine is whether it is a two-stroke or four-stroke engine, which obtain their names from the number of piston strokes necessary to complete a full cycle. Two-stroke engines were developed "to obtain a higher power output from a given engine size with a simpler valve design." [5] Figure 1 illustrates the strokes taken by the two-stroke (bottom) or four-stroke engine (top).

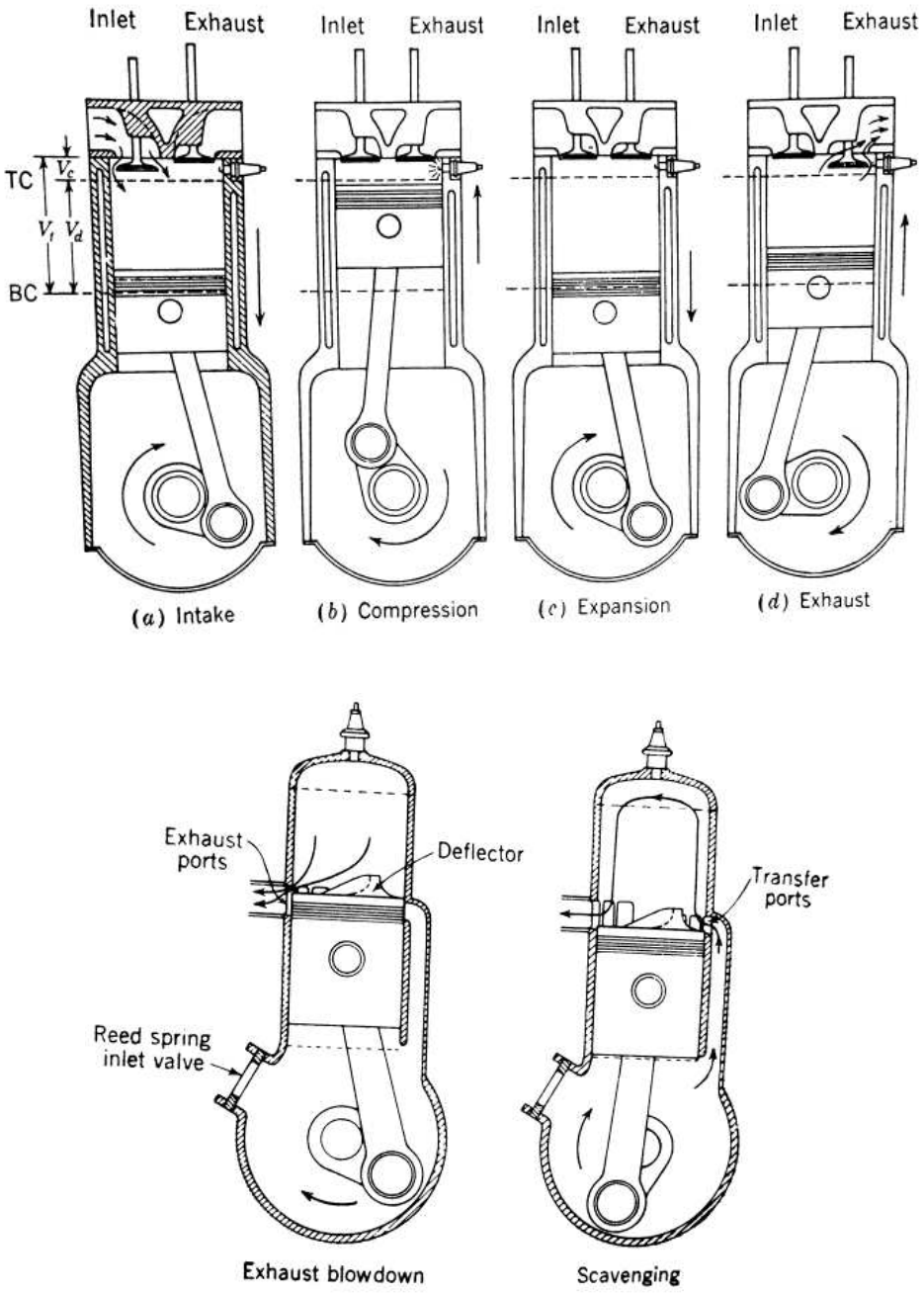

Figure 1: Four-stroke (top) and two-stroke (bottom) operating cycle [5]

A two-stroke engine will tend to operate faster and require a greater air mass flow rate than a four-stroke engine to achieve the same output power. The combined intake and exhaust process that a two-stroke engine undergoes since it has two fewer strokes is called “scavenging.”

The most common scavenging arrangements that a two-stroke engine could have to exhaust burned gases and supply a fresh charge of fuel/air are visible in Figure 2. A two-stroke engine also requires high intake pressures to displace the burned gases and supply a fresh charge of fuel/air, supplied by a separate pump or boosted by the compression in the crankshaft.

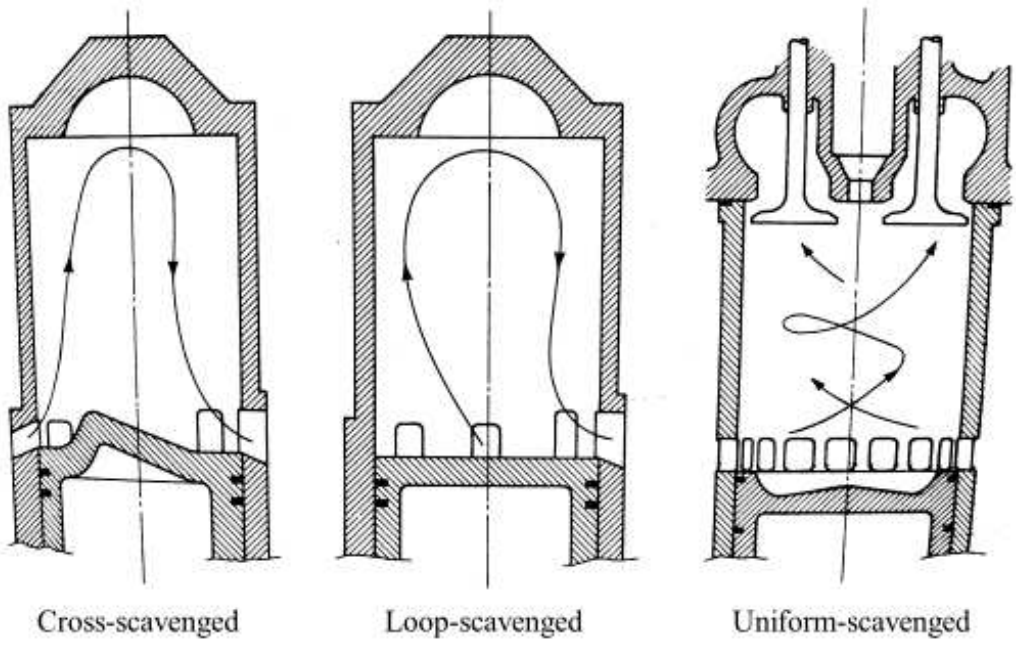

Figure 2: Two-stroke engine scavenging cycle flow configurations for cross-scavenging, loop-scavenging, and uniform-scavenging [5]

2.1.2 Spark Ignited and Compression Ignited IC Engines

A spark ignited (SI) engine is the most common ignition method and is the primary engine type used in passenger vehicles on the road today. In SI engines, spark plugs ignite the fuel/air mixture in the combustion chamber, and flame propagation is driven by the flow characteristics and turbulence within the combustion chamber.

Compression ignited (CI) engines are used heavily in industrial vehicles because of the low-end power possible, accelerating the vehicle at low rpm levels. CI engines use the

combination of pressure build-up from the piston, stratified fuel mixture from an injector, and chemical kinetics to cause the nonhomogeneous fuel mixture to combust. In CI engines, the flame propagation relies highly on the spray and piston characteristics, which drive the mixture stratification that leads to combustion.

As discussed earlier, the Carnot cycle describes the maximum efficiency that an ideal IC engine can produce. However, there are many engine classifications, and none of them come close to meeting the performance of an ideal IC engine. Two types of cycles are used to analyze the SI and CI engines thermodynamically. The Otto cycle is for SI engines and has an efficiency defined by the CR ($\mathbf{r_c}$) from equations (2) and (3), where γ is the ratio of specific heat.[6] As noted prior, knock limits the allowable CR by the need to prevent uncontrollable combustion. In the otto cycle, a CR of 11 has a maximum efficiency of 61%.[2]

$$r_c = \frac{V_{BDC}}{V_{TDC}} \tag{2}$$

$$\eta = 1 - \frac{1}{r_c^{\gamma-1}} * 100\% \tag{3}$$

The Diesel cycle used in CI engines is more limited by the engine's size than the CR since it can achieve very high CRs it requires a lot more volume to achieve those CRs.[6] The maximum efficiency an ideal CI engine can achieve is 56% at a CR of 15 and an expansion ratio ($\mathbf{r_e}$) of 5, which is calculated from equations (2), (4), and (5).

$$r_e = \frac{V_{BDC}}{V_{EE}} \tag{4}$$

$$\eta = 1 - \frac{1}{\gamma}\frac{r_e^{-\gamma} - r_c^{-\gamma}}{r_e^{-1} - r_c^{-1}} * 100\% \quad (5)$$

2.1.3 Limitations

Engine Knock is an abnormal combustion phenomena that occurs when auto-ignition is present ahead of the flame front. A great illustration of Engine Knock can be seen in

Figure 3. Various aspects in an engine could cause knock to occur, such as high CR, advanced spark timing, and improper use of an overly reactive fuel. Autoignition will not always lead to knock since, in CI engines, autoignition is used to initiate the combustion process. Engine knock autoignition is caused by an increase in pressure and temperature by both the flame front and cylinder pressure, which cause the rapid increase of radical species that lead to ignition. In that sense, engine knock could be simplified as a race to consume the fuel in the end gas before the fuel chemical kinetics result in autoignition.

Engine Knock prevention plays a significant role in the automobile industry today because of its damage to an engine and its power reduction. However, many factors play a role in causing knock, ultimately preventing it proves to be a difficult task. For that reason, research has focused on predicting knock and then taking actions to mitigate the occurrence and/or the severity of knock. [5]– [7], [8, p. 3]

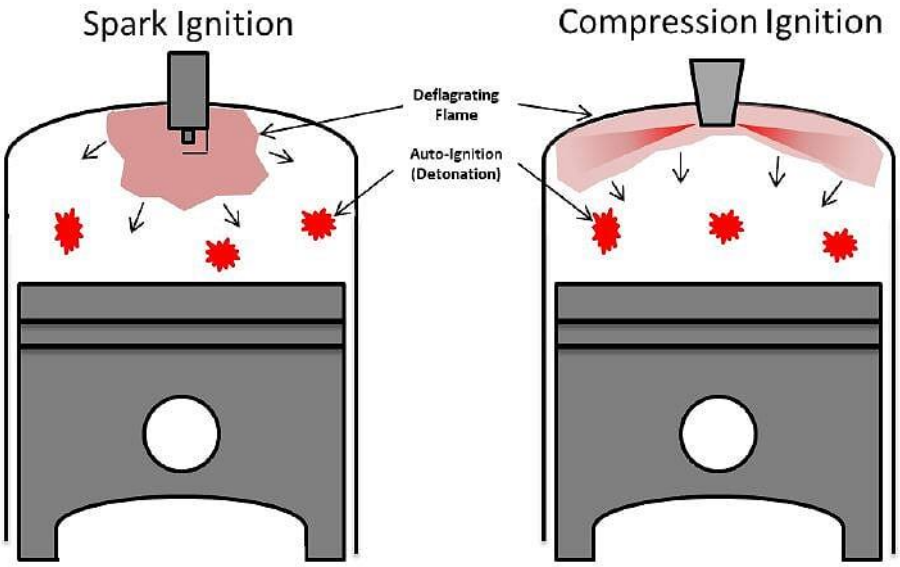

Figure 3: Engine knock description in both a spark and compression ignition system [11]

Research that has shown promise in mitigating knock is using direct injection to create stratified combustion that promotes flame propagation from the spark plug while reducing the ignitability of the end gas. Another approach to mitigate knock and even improve emission is by using cooled charged exhaust gas recirculation (EGR). Cooled charge EGR reduces the overall in-cylinder temperatures, which reduces high temperatures at the end gas that could lead to knock. Modifications to the engine geometry like piston and spark plug design have also played a big role in mitigating knock and improving efficiency. Finally, a proper choice of fuel is another area being researched to improve engine efficiency and emissions while avoiding knock. This stems highly from the fact that fuels themselves have knock resistant properties due to their chemical kinetics, which can be quantified with an octane number (ON). Many of the aforementioned research is being conducted experimentally with the assistance of CAE tools.

2.2 ICE Fuels

Since engine knock prevention is such an important and sought-after goal in SI engines, it makes sense that today's fuels are being classified on their resistance to knock. Octane number (ON) is a practical measure of determining whether a fuel will knock or not under given operating conditions. The higher the octane number, the higher the resistance to knock. However, since knock is not so easily determined by one variable, ON is also not just a single-valued quality and may vary depending on operating conditions. ON has a scale made up of the fuel's percentage of the two primary reference fuels (PRF). At the top of the scale is Iso-octane with an ON of 100, and at the bottom of the scale is normal heptane with an ON of 0. ON is based on how the fuel falls on this scale in the Cooperative Fuel Research (CFR) engine testing. SI engines typically want a high ON fuel; that is why commercial gasoline falls between 80 and 98 ON and depends on the specific engine being operated.

On the other hand, CI engines are not as preoccupied with knock as SI engines. It is quite the opposite effect; CI engines are more worried about the ignitability of the fuel. That is why the cetane number (CN) was created to determine the ignition quality of fuels used in CI engines. Two species like octane number determine the cetane number scale. Cetane is given a cetane number of 100 because of its high ignition quality, while Iso-cetane heptamethylnonane (HMN) has a 15 cetane number because of its low ignition quality. Fuels used in CI engines are given cetane number values determined by equation (6). [5]

$$\mathrm{CN} = \text{percent } 0\text{n} - \text{cetane} + 0.15(\text{percent HMN}) \tag{6}$$

The most common traditional fuels are gasoline and diesel because gasoline has a high ON and diesel a high CN. However, even natural gas and Jet propellant are becoming traditional

fuels in their industry. Jet propellant or JP-8 has been investigated in the feasibility of operating a two-stroke SI engine. Ausserer et al. performed experimental testing on a 20 ON primary reference fuel as a surrogate for JP-8 in three different unmanned aerial vehicle engine (UAV) platforms.[12] This investigation found that JP-8 could be used in a SI engine without any knock occurring, but only at very high speeds (7500-7900 RPMs). [12] At average speeds of 6000-7000 RPMs, some knock was observed, but it was not severe enough where action had to be taken to prevent mechanical damage, whereas, at low speeds of 4500-4600, the action did have to be taken. [12] Although Two-stroke engines operate at high speeds, the acceptable speed range for knock free conditions is too small. Even if the knock at average speeds is small, a continuous knock could still lead to mechanical failure if left to persist.

Renewable fuels have been around for years; however, due to lack of technology and more desire fuels like fossil fuels, they have only recently begun to impression IC engines. Digester or landfill gas is formed from anaerobic digestion of biodegradable materials by microorganisms.[13] Its composition is about 60 % CH4 and 40 % CO2.[13] Digester gas engines that use swage and manures as feedstock require regular maintenance to prevent hydrogen sulfide breakdown. As well as regular maintenance, landfill gas engines are “hardened” to combat siloxane contamination.[14] Reduced methane emissions from digester or landfill gas benefit the environment because the global warming potential is 30X that of carbon dioxide.[15] The production cost gap for renewable fuels has improved; however, they are still not low enough to be more favorable than fossil fuels. At any rate, the improvement to emissions combined with the strenuous emission regulations will make them more favorable as the production cost gap continues to close.

2.2.1 Dilute fuels

Dilute fuels have become very popular as of late. A primary reason could be because of exhaust gas recirculation (EGR), which has proven to improve fuel economy, reduce emissions, and reduce the coefficient of variations of IMEP when coupled with enhanced tumble motion. Zhang et al. researched the effects of tumble combined with EGR in SI engine performance and emissions.[16] The use of EGR in his research showed an improvement of 13.1%-19.5% in fuel economy and reduced NOx emissions while improving combustion stability. [16]

Producer gas is another type of diluted fuel with H2, CO, CH4, and CO2 that is gasified from solid organic waste matters like rice husk, sugarcane trash, or bagasse.[17] Producer gasses are a less knock-resistant fuel with a reduced LHV at stoichiometric mixture than natural gas, which is why it must be de-rated. Even though producer gas engines are de-rated, they still produce lower NOx emissions as well, and Babu states that the increasing CR will limit the required engine de-rating when utilizing dilute fuels.[18] Syngas is similar to producer gas when it comes to species composition except that they are produced from wool and coal since the 18th century. Syngas has also been compared to natural gas and has also reduced NOx emission in gas turbines and SI engines.[19] There has even been a study that used syngas as a dual fuel with diesel to increase engine performance. [20]

2.3 CAE of IC Engines

CAE tools, including engine modeling software (GT Power) and computations fluid dynamics (CFD) simulations (Ansys, Converge, STAR-CCM+), are becoming commonplace in modern IC engines' design. These CAE tools allow for low-cost simulations that offer predictable results to experimental testing and provide a more in-depth insight into the physical characteristics inside an IC engine.

2.3.1 Piston Designs

Pistons have come a long way from the basic default pancake piston design used in all production premixed SI engines. Engineers now incorporate many different aspects into piston designs like intake flow, spray injectors, spark location, and many others. Research into piston designs has intensely focused on CI engines like Homogenous charge compression ignition (HCCI), reactivity-controlled CI, and premixed charge CI engines because of the need for high turbulence to promote fuel-air mixing from a spray injector. However, the recent popularity of direct injectors in SI engines and the increased interest in different fuels have led to more piston design research being conducted on SI engines to generate higher turbulence, leading to improved mixing and faster burning rates while still avoiding knock. [21] Liu and Dumitrescu et al. investigated the ability to convert a diesel CI engine into a natural gas SI engine.[22] CFD analysis and experiments were performed on the squish region of a re-entrant bowl to investigate the effect that squish has on engine performance. It was concluded that a larger squish region would improve engine performance but would increase NOx emissions. The larger squish region would increase the turbulence inside the bowl, which led to very fast flame propagation that would thin out and slow down when it reached the squish region.[22] By coupling CFD and experimental data, further knowledge was gained on a key component of piston design. It just comes to show that even minimal changes to a piston geometry can make a big effect on an IC engine's overall performance. This could not be truer for the work carried out by Amann et al. that found a “strong correlation between the frequency of Low-speed Pre-ignition (LSPI) and the depth of the chamber” on the crevice of a pancake piston.[23] LSPI is another combustion phenomena like knock that leads to what people are calling “super knock.” It is adequate to say

that through CFD and experimental testing, even more discoveries can be made on the effects that different piston geometries have on SI engines.

2.3.2 Spark Plugs

Spark plugs have a straightforward job in an engine, setting a spark to the fuel and air mixture to promote the combustion process. They are relatively small, and the common J-gap design is used in most engine applications; however, extensive research is being carried out on different spark plugs and their effect on performance.

Figure 4 shows a cross-section cut of a spark plug with component names to understand terminology better. Spark plug names stem from the electrode and gap configuration. For example, the J-gap spark plug stems from the fact that the ground electrode is in a “J” shape. Other spark plug types include surface gap, Duel-bar electrode, fine wire electrodes, and many others. [24] Spark plugs even have different heat ranges that depend on air/fuel mixture, advanced spark timing, and CR. Other factors that determine what type of spark plug to select include the engine application, the type of fuel, and whether it is naturally aspirated. For example, hydrogen-powered engines with platinum spark plug tips could experience preignition because platinum is a catalyst for hydrogen combustion.[25] Platinum significantly lowers the energy required for autoignition, and if the spark plug wire gets too hot from cycle to cycle, this could lead to preignition.[25]

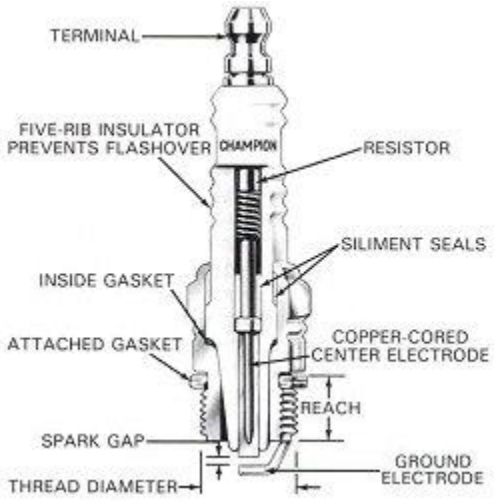

Figure 4: Cross-sectional cut out of a J-Gap spark plug with labeled components [26]

With the J-gap spark plug being used in most vehicle applications, the question is, "why do other spark plugs matter." The answer to that question is the improvements to combustion that other spark plugs give and all the different engine applications. The fine wire electrodes were designed to improve starting and anti-fouling characteristics in small two-stroke engines. [24] It was proven that the dual-bar electrode spark plug had better flame kernel growth and propagation than the J-gap spark plug from Tozzi et al. [27] The reason being that the dual-bar electrode had a lower surface to volume ratio (S/V) value than the J-gap spark plug, which can be calculated with equation (7). [27] For this same reason, increasing the spark plug gap will increase flame kernel development and propagation by increasing the volume of the gap confined between the electrode surface. [27] As further research is carried out on spark plugs, even correlation will be made to assist when deciding what spark plugs to use to improve combustion for each application.

$$S/V = \frac{\text{electrode surface area}}{\text{Volume of the gap confined between electrode surface}} \quad (7)$$

Through research, it was determined that not only does spark plug type play a huge role in engine performance, but so does spark plug location and the swirl rate that the engine creates. Witze et al. performed an experimental study with three different spark plug locations on an idealized research engine with optical access, a disc-shaped combustion chamber, and a surface gap spark plug. [28] This research engine could vary the engine's swirl and turbulence by changing a shroud's orientation on the intake valve. The study that Witze et al.[28] performed found that a centrally located spark plug is generally preferred except at high swirl conditions. At high swirl conditions, a sidewall located spark plug is preferred because the flame is convection-driven versus distance-driven, which is the case in low and no swirl conditions. [28]

2.3.3 Fuel Injectors

Stratified combustion is used today to address engine knock. Stratified combustion takes advantage of a non-homogenous air-fuel mixture in the cylinder to control combustion phasing. In normal non-stratified combustion, the fuel to air mixture in the cylinder is homogeneous, whether stoichiometric, lean (excess air), or rich (excess fuel). An example of stratified combustion can be seen in Figure 5, where the rich fuel is closest to the spark plug, and a lean fuel is closest to the piston. The main reason for having stratified combustion like in Figure 5 is that a rich fuel region will ignite (via spark) more easily than a lean mixture. In contrast, the lean mixture closest to the piston makes it harder for auto-ignition (resulting in knock) to occur in the spot where the pressure build-up is greatest. [29] The most common form of stratified combustion is injecting the fuel like usual but then igniting immediately after injection so that the fuel does not have enough time to mix with the air in the cylinder. [30] In Drake et al., an experimental and simulation study was performed, which focused on the two stages of the combustion process (turbulent partially premixed flame propagation and mixing-dominated

combustion of the rich products left from the partial combustion of initially fuel-rich mixtures). The investigation was successful in obtaining similar trends in combustion propagation, similar liquid fuel spray structure, and penetration for both CFD and experimental testing in a gasoline-powered spray-guided spark ignited direct injection (SG-SIDI) engine. Their research combined with other similar work showed that SG-SIDI engines have the advantage of wider stratified operating range, reduced soot emissions, and lower HC emissions over a wall guided-SIDI engine. This thesis proposes that stratified combustion can also be achieved by using multiple pulses of injection, each with a different amount of fuel. This can be referenced as altering the "rate shape: of the injector or the amount of fuel mass injected over time. [11]

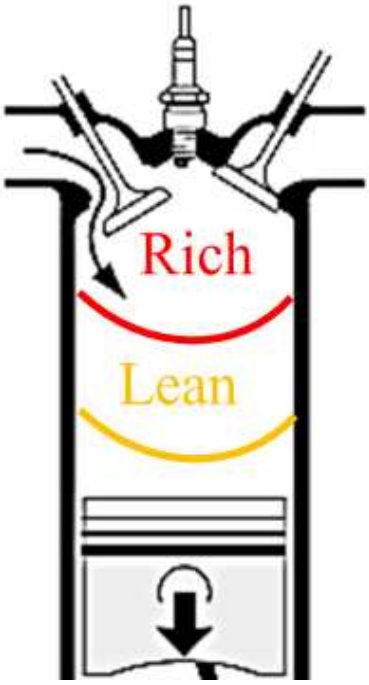

Figure 5: Stratified combustion of the rich and lean fuel mixture to avoid engine knock

Atomization is the process of breaking down a stream into fine droplets. The simplest and most common example of this is a spray bottle that turns a liquid cleaning supply into a spray of

droplets. Atomization happens with the help of pressure and holes in a nozzle used to break up the liquid. This same process happens in an engine to achieve atomization but with adequate droplet size and faster speeds. Figure 6 shows a solenoid-based fuel injector that is used in most motor vehicles today. As fuel is needed, the fuel is pumped from the fuel tank to the fuel injector at about 60 psi pressures. When the fuel gets to the fuel injector, it cannot enter the cylinder until the valve is lifted, activating the nozzle. The valve can only be opened when current is supplied to the electromagnetic coil creating a magnetic field that pulls the magnet up, opening the valve. All this happens in a matter of milliseconds since the injector is completing 1500 or 3000 injections per minute in a 3000 RPM four-stroke or two-stroke engine, respectively.

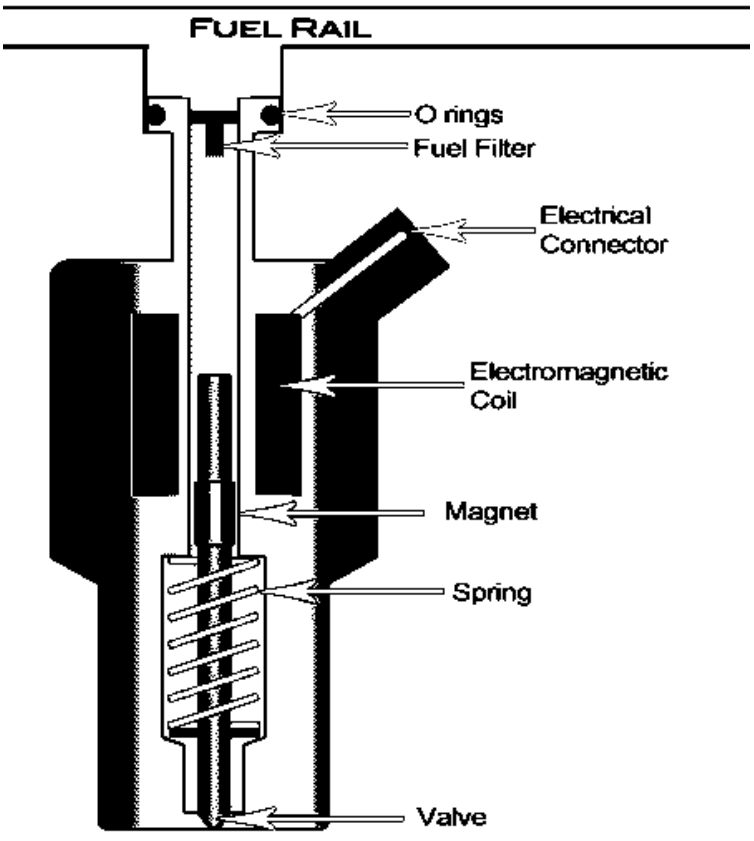

Figure 6: Solenoid-Based fuel injector components [31]

The right level of atomization is important for low emissions, high-efficiency engine operation. Low levels of atomization with droplet sizes greater than 40 μm in diameter lead to a slow-reacting diffusion flame, which is not suitable for SI internal combustion engines. As the droplet size approaches 10 μm, fast-acting premixed gaseous combustion that drives the power stroke in IC engines is achieved. [32] To achieve this level of high atomization, usually high pressures and high flow speeds are used. However, there is a new technology called Electrostatic Atomization, where high pressures are not required, but instead, a strong electric field is used to cause atomization. This works with the help of a carbon-coated tube mesh that is positively charged in which the liquid passes through charging the liquid and when the repulsive forces exceed the surface tension of the liquid.[33] A Rayleigh fission will occur, and the liquid will split into droplets at low pressures. This new advancement in technology has successfully achieved droplet diameters of 3 μm "improving the fuel burn efficiency and resulting in less harmful emissions." [33]

Viscosity is important as a fuel property because it describes the resistance to the flow of a fluid. The higher the viscosity of a fluid, the more resistant it is, and the lower the viscosity, the less resistant it is. Viscosity is important as a fuel because the easier a fuel can flow, the less pressure is required in an injector. This can also be seen in equation (8), which describes how velocity (V_m) is affected by viscosity (η) and pressure in a laminar pipe, where $\Delta P/\Delta x$ is the pressure gradient, and R is the radius of the pipe. [12] More viscous fuels will require a greater pressure to achieve high injection speeds used to break down the fuel into droplets.

$$V_m = \frac{R^2}{4\eta \frac{\Delta P}{\Delta x}} \quad (8)$$

The volatility of fuel also plays a role in stratified combustion since volatility is described by how easy it is for fluids to evaporate. The easier it is for fluid to evaporate, the more volatile it is. The harder it is for fluid to evaporate, the less volatile it is. Volatility can also be related to the flashpoint temperature of the fuel. The more volatile a fuel is, the lower the flash point temperature it has, and the easier it is to ignite. [13] Fuels with low volatility would be harder to mix and also would require higher temperatures to ignite in stratified combustion.

These issues can be solved with spray injection modeling in CFD. Bravo et al. were able to use Lagrangian modeling in CFD to simulate the injection of two JP-8 surrogates with good experimental data agreement using a single hole injection nozzle; however, when using a two-hole nozzle injector, there was an overprediction of 3-5 mm in droplet diameters. [34] The simulations were performed using CONVERGE CFD and their famous adaptive mesh refinement technique, and they compared k-ε Reynolds-average Navier-Stokes and Large Eddy simulation turbulence models. [34]

Chapter 3: General CFD Methods

As many things vary from engine simulation to engine simulation, this will be a broad overview of the Methods used to perform a case set up in the selected Computational Fluid Dynamic (CFD) software CONVERGE version 2.4 & 3.0. CONVERGE is a powerful engine CFD simulation program that is becoming very popular in the automotive industry because of its meshing refinement techniques that help obtain accurate results with low computational costs. CONVERGE uses its program call “studio” as a platform for performing geometry and simulation case setup. Once the setup is complete, files are exported then solved in the CONVERGE solver program that must be carried out using Parallel Message Passing Interface (PMPI). Since CONVERGE is such a powerful and popular tool, many inputs are left on default or their recommended values, as CONVERGE prescribes. Further details and any differences in the specific engine simulations will be discussed in each of the Manuscripts’ Method sections. (Chapters 4.2, 4.4, 5.2).

3.1 Geometry setup

The 3-D geometric models in CONVERGE consist of walls, which are directly in contact with the fluid. For that to be possible, the 3D model must be imported as a stereolithography (STL) file from a computer aid design (CAD) software like SOLIDWORKS. [35] When the model's STL file is imported, its geometric triangular meshing is already set up; however, this is not the final meshing that the geometry will have. The models require a strenuous vetting by the CONVERGE studio software to ensure there are no open edges, intersections, nonmanifold problems, overlapping triangles, isolated triangles, or normal orientations. To assist with

identifying issues like open edges, CONVERGE has a diagnostic tool that identifies all issues that must be resolved before running the simulation. If these errors are not addressed, the engine case will crash. The process of fixing these errors and preparing the 3D model for simulation work is called “cleaning the geometry.” Figure 7 is a representative case of the CONVERGE studio platform, which is used for geometry and simulation case setup. Further information on these errors and the techniques used to resolve the issues were obtained from the CONVERGE studio manual. [36]

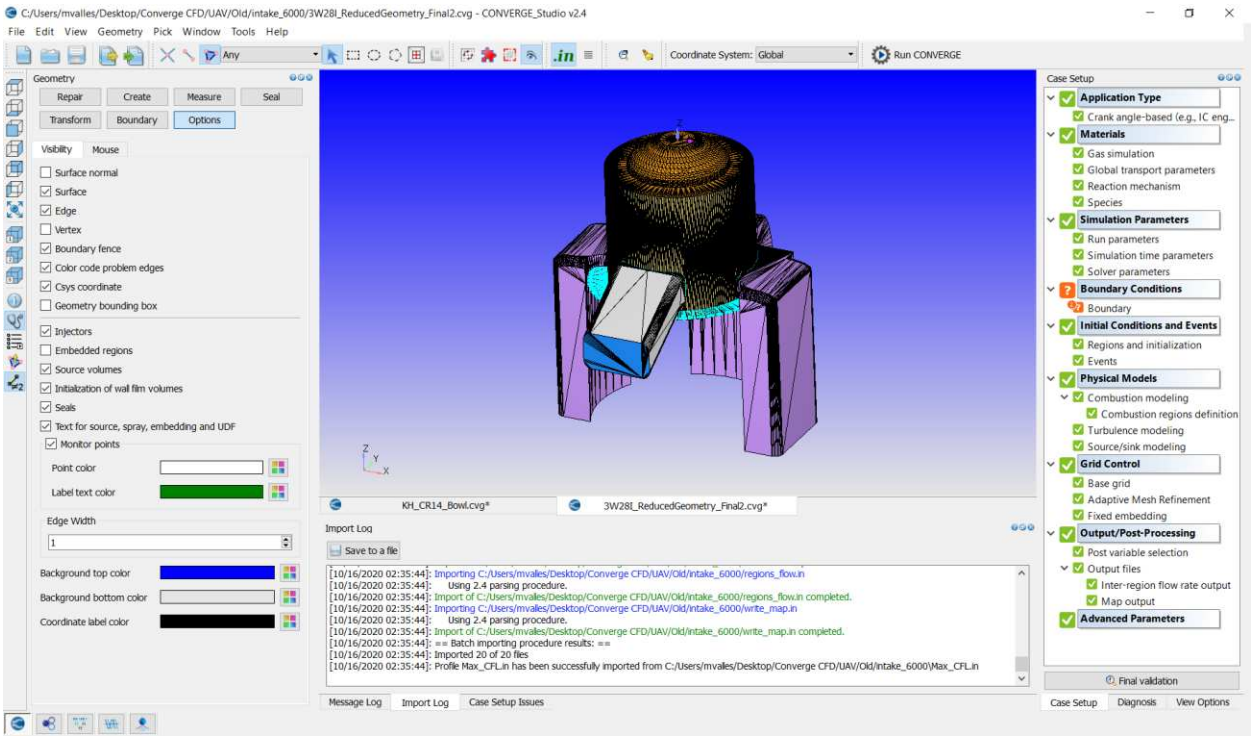

Figure 7: CONVERGE Studio interface for geometry and simulation case setup

3.2 Chemical kinetic solver

The combustion modeling technique in this study was the CONVERGE SAGE detailed chemical kinetic solver. SAGE uses the selected chemical mechanism and ODE solvers to represent the chemical reactions and combustion that occur in the engine. SAGE can simulate

engine knock by solving the chemical kinetic rate equations in the end gas, accounting for varying mixture composition and engine conditions. CONVERGE uses the same technique to calculate combustion. CONVERGE takes the forward and reverse rate Coefficients for all the mechanism files' reactions with the thermal properties (entropy, enthalpy, specific heat over gas constant) for each species at different temperatures to solve Turn's mechanism equations listed in the Appendix.[29], [36] With those equations solved, then the governing equations for mass (9) and energy at both constant volume (10) and pressure (11) are solved for each computational cell at every time-step to simulate the chemical kinetics that occurs during combustion. In the equations (9)-(11), m is species, $\dot{w}_m$ is the net production rate for m, is the molar concentration for m, V is volume, P is pressure, T is temperature, h_m is molar specific enthalpy, s is entropy, $C_{P,m}$ is molar constant-pressure specific heat for m, Q is the heat release rate

$$\frac{d[x_m]}{dt} = \dot{w}_m \tag{9}$$

$$\frac{dT}{dt} = \frac{V\frac{dP}{dt} - \sum_m(\overline{h_m}\dot{w}_m)}{\sum_m([x_m\overline{C_{P,m}}])} \tag{10}$$

$$\frac{dT}{dt} = \frac{\left(Q/V\right) - \sum_m(\overline{h_m}\dot{w}_m)}{\sum_m([x_m]\overline{C_{P,m}})} \tag{11}$$

Chemical mechanisms were carefully selected for each fuel, as they are critical for SAGE to predict knock and simulate combustion. CONVERGE recommends that these chemical mechanisms have less than or equal to 100 species for best performance with the dense CVODES solver in SAGE. CONVERGE uses variable time-step algorithms that incorporate CFL limits, initial, minimum, and maximum time-step user-specified values to find the optimal

time-step throughout the end cycle continuously. CONVERGE has three different CFL limits that can be prescribed to alter the time-step, and the algorithms for these CFL limits can be found in equations (12)-(14) for Maximum convection (CFL_u), Maximum diffusion (CFL_v), and Maximum Mach (CFL_c) CFL limits, respectively. In equations (12)-(14), u is the cell velocity, v is the viscosity, c is the speed of sound, Δt is the time step, and Δx is the cell size. CFL stands for the Courant-Friedrichs-Lewy condition, a condition required for convergence in solving partial differential equations. It is recommended that a CFL number should be less than 1 for accuracy in calculating partial differential equations because it will reduce the time-step and calculation errors. However, with a CFL number less than 1, far more calculations are to be performed, leading to higher computational times. For that reason, CONVERGE gives recommended CFL number ranges for the three CFL limits that are not restricted to only being less than 1: 0.1-2.0, 0.5-2.5, 1-100 for convection, diffusion, and Mach, respectively.

$$CFL_u = u\frac{\Delta t}{\Delta x} \tag{12}$$

$$CFL_v = v\frac{\Delta t}{(\Delta x)^2} \tag{13}$$

$$CFL_c = c\frac{\Delta t}{\Delta x} \tag{14}$$

CONVERGE uses a technique called “adaptive zoning,” which accelerates the chemistry calculations by grouping similar computational cells and then invoking the chemistry solver once per group rather than once per cell to improve computational timing. [36] Further details on each simulation's chemical mechanisms will be discussed in each manuscripts’ method sections. (Chapters 4.2, 4.4, 5.2).

3.3 Case setup

The 3D models were labeled into many subparts, which are called boundaries in CONVERGE. These boundaries are standard parts in an engine combustion chamber such as the piston, intake port, etc. Labeling these boundaries allows for a more accurate representation of the engine boundary conditions, thus leading to far more accurate results.

3.3.1 Boundary Conditions

CFD simulations were set up with temperature and pressure boundary conditions for three types of boundaries (walls, inlet, outlet) informed by GT-Power while mimicking the corresponding experimental test conditions. The temperature and pressure for the three regions' initial conditions (Intake, Cylinder, Exhaust) were obtained from experimental data at the simulation start time, set right before intake. A region is made up of the physical boundaries and their enclosed spaces created by the user. For example, “intake” is a region made up of an intake valve, intake port boundary, and the enclosed space these boundaries make up. The 3D models were oriented so that the Cartesian coordinate origin would be centered on the cylinder head. This way, the piston movements could be referenced easily from this fixed point and would only require a z-coordinate value. GT power can perform 1-D engine simulations while simultaneously solving a heat transfer model for many cycles to achieve steady-state results comparable to experimental data rapidly. For this reason, the tuned GT-Power models were subsequently used in two-folds:

(1) To develop a predicted 1-D engine simulation incorporating detailed chemistry that could be used to identify optimal engine operating parameters

(2) To provide boundary conditions for 3-D CFD engine simulations, such as inlet, outlet, and boundary wall temperatures, which enables the use of single-cycle simulations to predict engine performance.

3.3.2 Mesh configuration

CONVERGE CFD has various mesh manipulation techniques that effectively capture data while ensuring the computational times are as low as possible. These techniques are adaptive mesh refinement (AMR) and fixed embedding, which are used to manipulate the user-defined base grid mesh. CONVERGE gives the option of selecting many different types of fixed embedding; however, the three main fixed embedding types used in this work were boundary, spherical, and region-based. Boundary embedding refines the mesh for the boundaries/geometric parts mentioned earlier. Spherical embedding manipulates the based mesh of a sphere that the user creates and can be placed anywhere and have whatever diameter the user wishes. Region embedding is a little more complicated in that it refines the mesh of a region. Once the embedding is selected, a mesh refining scale is given to establish the user's level of refinement. Equation (15) demonstrates how the scale is used to refine the base mesh (dx_{base}) into a new mesh size (dx_{new}) for a specific user-defined time range. All of the boundaries received fixed embedding to some user-defined scale and for a duration of time. For example, at the start of the simulation, intake and exhaust boundaries were given boundary embedding to refine the mesh at the walls to reduce boundary layer errors when the valves open. The liner, piston, and cylinder head were also given boundary embedding; however, their duration was not set since these boundaries make up the combustion chamber. The specific values for embedding timing and sizing will be discussed more in-depth in each simulation section as they differ drastically depending on the engine and engine timing. Spherical embedding was used to refine the meshing

at the spark plugs to capture the velocity fields and combustion temperature gradients adequately. During intake and compression, two spherical embeddings were placed at the center of the spark plug gaps with different scales and diameters.

$$dx_{new} = \frac{dx_{base}}{2^{scale}} \tag{15}$$

Before ignition, multiple spherical embeddings were used to assist AMR and capture the flame kernel growth in the combined Lagrangian & Eulerian method. This technique of multiple spherical embedding is called “a bubble embedding.” It is developed by studying the flow velocities at the spark plug slightly before and after ignition timing to infer which direction the flame will propagate after ignition. [37] This technique drastically reduces computational time while ensuring high-quality results are not missed AMR, which waits to first detect the temperature fluctuations before refining the mesh. An example of this “bubble embedding” technique can be seen in Figure 8 and was developed with post-processing software. Figure 8 illustrates a bubble embedding template of five spheres, which was already set for a case with a spark timing of -23° after top dead center (ATDC). Four spheres follow the velocity field with an average of 3 m/s velocity staring at the center of the electrode and working out from smallest to largest in diameter to create the “bubble embedding” like the one seen in Figure 8. A fifth sphere that is 2 mm in diameter is placed around the four other spheres to assist the mesh refinement and capture the flame propagation away from the spark gap. The sphere locations are then used to create spherical fixed embeddings in CONVERGE. The spheres refine the mesh from 31.25 µm closest to the center of the electrode to 125 µm. This is a combined Lagrangian & Eulerian method because multiple spheres are similar to the Lagrangian method, where a single particle is

followed on a path. However, the Eulerian method stems from the fact that the volumes become fixed to accurately calculate the temperature change once the spheres are placed in their designated spots.

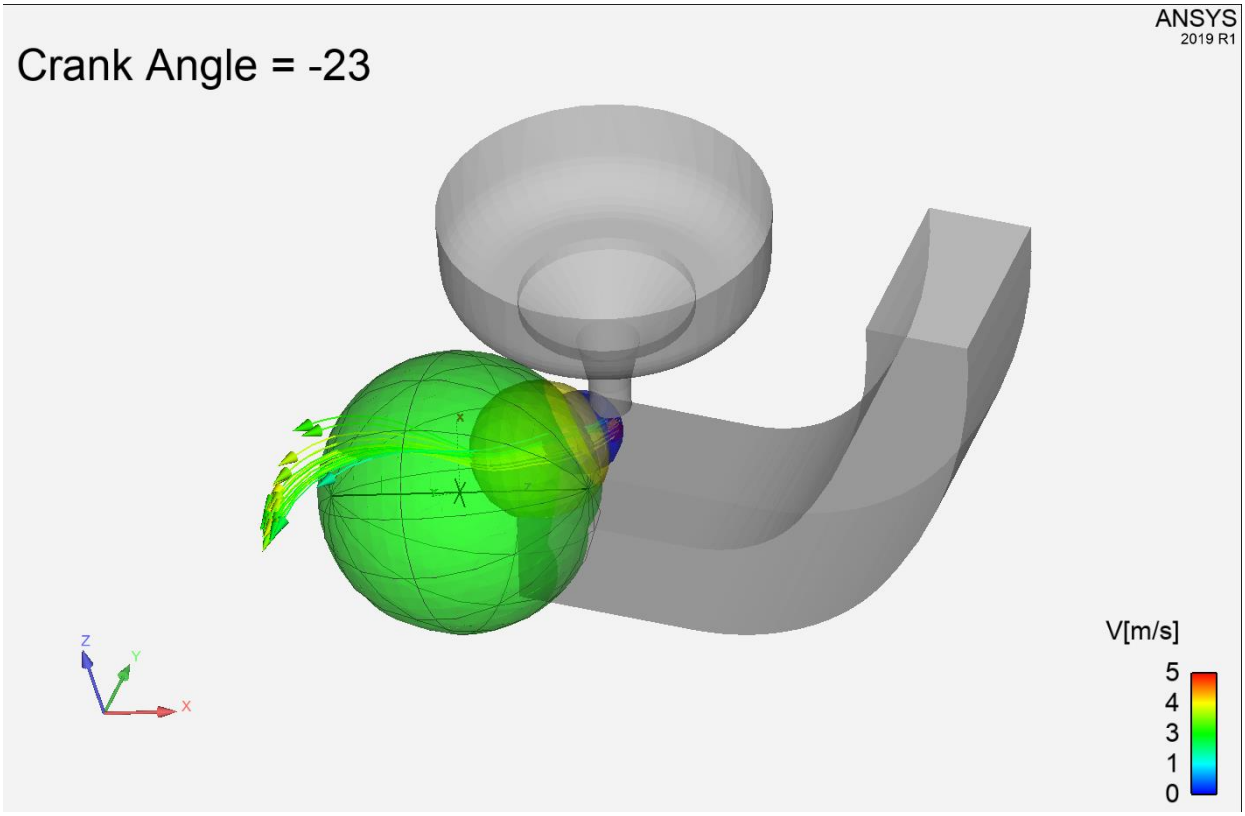

Figure 8: Velocity field at spark plug with “Bubble embedding” technique at -23° ATDC sparking timing

Using mapping techniques, the calculations performed in the combustion chamber during intake can be stored and used in another simulation. This ability allows for the removal of the intake and exhaust ports during the compression and combustion strokes so that there is additional computational power available to simulate the combustion process. This ultimately saves time for tuning the combustion parameters to validate the combustion model. AMR, along with the Reynolds-Average Navier-Stokes (RANS) and re-normalized group (RNG) k-e model,

were used to adequately model the flow during intake and compression capturing the velocity fields. A cell is refined from 4 mm to 0.5 mm when the sub-grid field's absolute value is above a user-specified value called the “sub-grid criterion.” The embedding is then removed if the sub-grid field's absolute value is below $1/5^{th}$ of the sub-grid criterion. [36] Velocity and temperature had a sub-grid criterion of 1 m/s and 2.5 K, respectively. AMR was limited to a maximum of 1.6 to 2.5 million cells to stay within the limit of 30 to 40 cores per simulation limited by the server resources. CONVERGE 2.4 recommends using 30,000 to 50,000 cells per core; however, after further investigation, it was found that 15,000 to 30,000 cells per core was a better range for faster simulation times. AMR also can redefine the sub-grid criterion to stay within the AMR cell limit. CONVERGE had four heat transfer models available: O’Rourke and Amsden, Han and Reitz, Angelberger, and GruMo-UniMORE. The Angelberger model was designed to improve the mean heat loss of the turbulent flame brush to the cold combustion chamber walls. [38] This does sound better; however, since wall temperatures come from GT power, the Angelberger model's added resolution was not needed. The GruMo-UniMORE model was not a desirable heat transfer model since it was developed for current production engines that are highly-charged/highly-downsized. [39] The O’Rourke and Amsden heat transfer model was ultimately chosen in conjecture with the standard wall function to represent the wall temperature heat transfer because of its lower heat transfer coefficient predictions achieved better knock validation in simulations than the Han and Reitz model. Dayal et al. also discovered that the O’Rourke and Amsden model was an optimal option because it had better accuracy and reduced computational time versus Han and Reitz and Angelberger. [40]

3.3.3 Spark Modeling

The spark modeling was performed using a spherical source of energy at the center of the spark plug gap at the start of ignition. The diameter of the sphere is dependent on the gap of the spark plugs. An L-type spark energy deposition profile was used in the engine models with 20 mJ applied for 0.5 CADs to simulate the breakdown phase. The arc and glow phase of the spark plug used 20 mJ for 10 CADs. The amount of energy deposited in this source was 40 mJ out of the 125 mJ measured during the experimental testing, which conforms to the general rule of thumb that 30-50% of the spark energy is transferred to the mixture. [41]

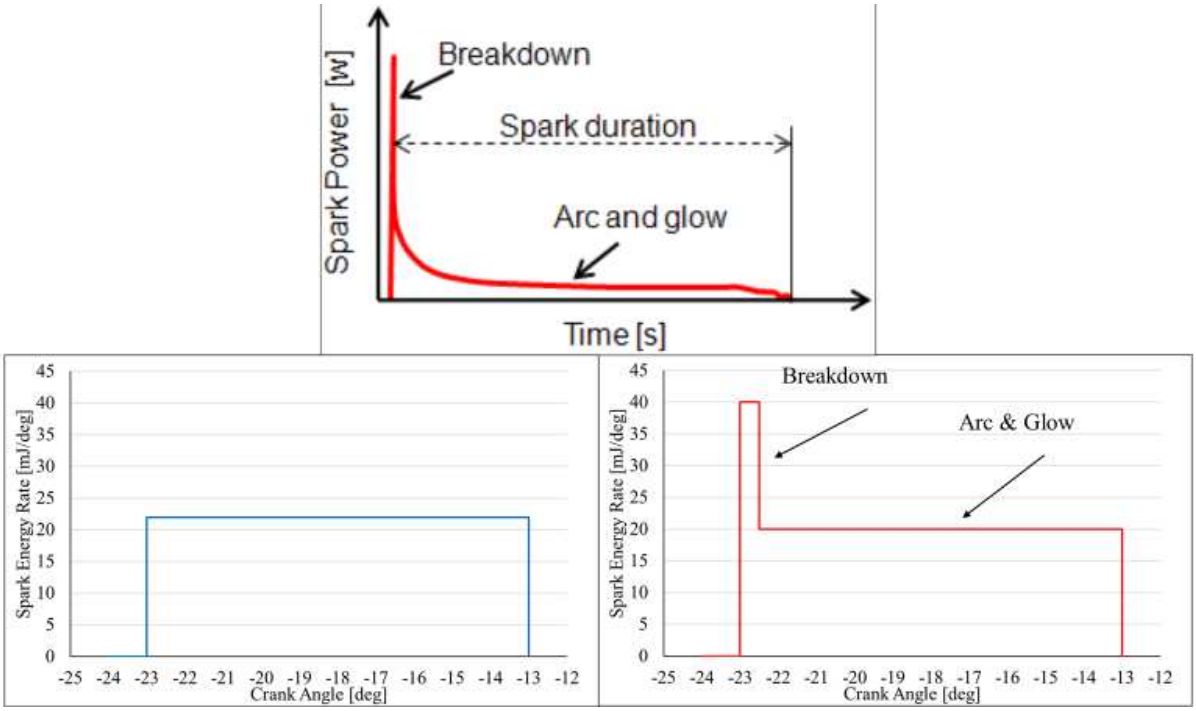

Figure 9: Energy deposit profile for a spark plug (top), Uniform energy deposit profile (bottom left), and L type energy deposit profile (bottom right) [41]

3.3.4 Additional information

All data presented in this thesis were calculated from the same equations and used only pressure results to reduce discrepancies in different equations. The AHRR ($\frac{dQ}{d\theta}$) equation comes

from Heywood et al. and can be seen in (16) where γ is the specific heat ratio held constant at 1.35, P is the pressure in pascal, V is the volume in cubic meters, and θ is the crank angle in degrees.[5] The AHRR was then zeroed until spark timing and filtered to reduce noise. The AHRR was then integrated for each crank angle for the full cycle to obtained Cumulative Heat Release (CHR). The Mass Fraction Burned (MFB) equation that led to finding the values for CA10 and CA50 can be seen (17). IMEP was calculated using equations (18) and (19), where W is work in joules and V_d is the displaced cylinder volume. Indicated efficiency (η) was calculated using equations (18) and (20), where m_f is trapped fuel mass in kg and Q_{HV} is the lower heating value for the fuel in J/kg.

$$\frac{dQ}{d\theta} = \frac{\gamma}{\gamma - 1} P \frac{dV}{d\theta} + \frac{1}{\gamma - 1} V \frac{dP}{d\theta} \tag{16}$$

$$MFB_\theta = \frac{CHR_\theta}{CHR_{max}} \tag{17}$$

$$W = \int P \, dV \tag{18}$$

$$IMEP = \frac{W}{V_d} \tag{19}$$

$$\eta = \frac{W}{m_f Q_{HV}} \tag{20}$$

All the engine simulation images were developed using EnSight, a post-processing software developed by ANSYS. EnSight allows the user to analyze, visualize, and communicate simulation data in a distinctive way that could not be possible otherwise. EnSight is capable of illustrating velocity fields, variable dependent gradients, and iso-surfaces. Many of the images

seen in this project come from the EnSight software, which will enhance the data presented in the graphical results. [42]

A two local Linux cluster was used for all the simulations carried out in this work. Each of these clusters was maintained and operated by Colorado State University's Engineering Technology Services. These two clusters comprised a system of high-performance processors with 50+ nodes, all varying from 12 to 24 cores and 64 to 256 MB of RAM. Running of CONVERGE was carried out using Parallel Message Passing Interface (PMPI) to handle the parallel processing. A full 720° cycle's simulation run time was a maximum of 4 days, about 1 day for each engine stroke.

Chapter 4: Hybrid Solid Oxide Fuel Cell & ICE Power Plant (Manuscript 1)

4.1 Background

Recent innovations in Metal Supported-Solid Oxide Fuel Cell (MS-SOFC) have increased their longevity and reliability. An MS-SOFC has been developed that operates at an intermediate temperature of 600℃, has increased power density due to its ability to operate at elevated pressures, and possesses a high internal reforming capability, which allows it to operate using pipeline natural gas (NG). [43] MS-SOFC has the potential to become a distributed electricity generation system because of the capability to react quickly and can produce higher efficiencies than Rankine power plants. There are still significant challenges to the adoption of MS-SOFC power generation systems for distributed electricity generation.

One of these challenges is a build-up of carbon on the fuel cell elements called “coking, " which reduces efficiency and increases maintenance costs to clean carbon build-up. This coking problem can be resolved by underutilizing the fuel cell, which will still reduce efficiency; however, it will also decrease capital costs for the fuel cell elements. Furthermore, an additional reduction in fuel cell capital cost can be obtained by operating the fuel cell while pressurized and increasing its power density- an important aspect of the proposed system. Underutilization of the fuel cell also leads to high concentrations of H_2 and CO being present in the exhaust gas on the anode side. This exhaust gas from the anode side carries thermal energy, with temperatures of 600℃, and, although it is highly diluted (~80% CO_2 and H_2O), it also contains ~2600 kJ/kg lower heating value (LHV) of chemical potential energy. When an MS-SOFC releases this exhaust gas into the atmosphere, it represents a loss of potential energy that could be beneficial for power generation and heating. The highly dilute nature of the anode tail-gas generally would cause extremely low

flame speeds making its use in an ICE nearly impossible; however, this effect is offset by the presence of ~17% of H_2, which will increase the tail-gas laminar flame speed. The IC engine is also a cheap solution for powering a compressor to pressurize the fuel cell without reducing efficiency.

The purpose of this project is to determine if the diluted tail-gas exhausted by the anode side of the MS-SOFC named “Anode Tail-gas” can fuel an internal combustion engine (ICE). If feasible, this could lead to the development of a hybrid power generation system that operates at an overall system efficiency >70%-LHV, at a rated power of 125 kWe with a cost of <850 $/kW. [44] However, for this to be possible, the IC engine must operate at 35% efficiency. Figure 10 shows a simplified schematic of the proposed hybrid system. Both the ICE and the MS-SOFC supply power to a DC/AC inverter to provide 120V AC electric power. A low-cost system of this size could lead to increased adoption of distributed electricity generation systems that would relieve strain on the electric grid, reduce the dependence on lower efficiency fossil-fuel generation systems and eliminate losses from transmission and distribution. [44] Distributed electricity generation of this kind also provides the ability to convert waste heat to useful thermal energy.

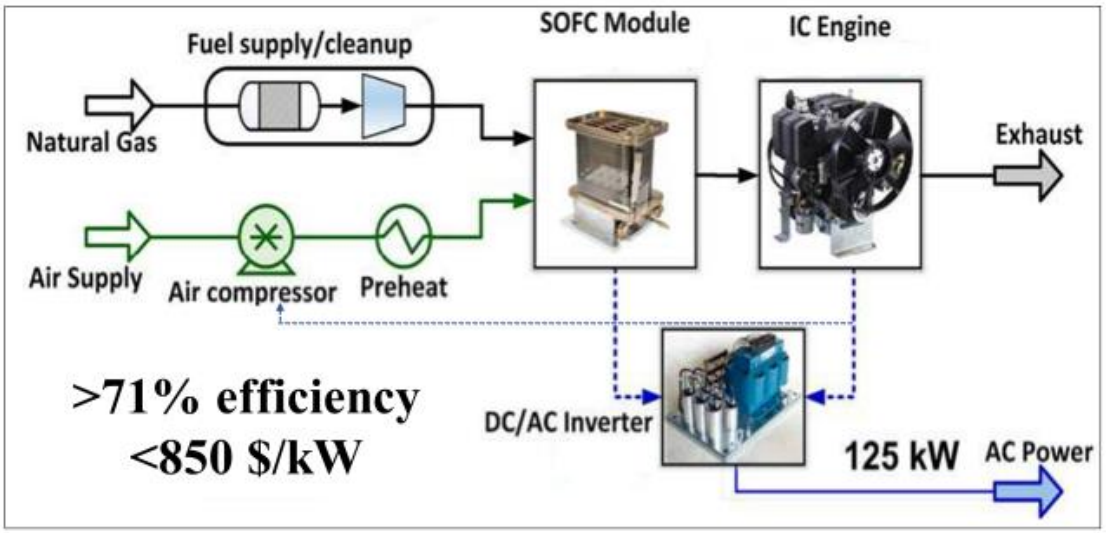

Figure 10: Hybrid SOFC/ICE schematic [44]

The development of this hybrid system requires a detailed investigation into the dilute anode tail-gas fuel properties, including understanding the requirements to achieve combustion and the ability to determine where the limits of misfire and knock onset reside. [43] The Cooperative Fuel Research (CFR) engine was utilized to perform combustion testing and understand how this non-traditional fuel operates in an ICE engine. The experimental investigation, coupled with Computer Aid Engineering software (GT Power and Converge CFD) were used to achieve the project goals. Additional details of the initial feasibility testing performed for this research can be found in Balu et al. [45]

This research's overall objective is to use the collected data from previous work to calibrate a 1-D engine model in GT-Power and validate predictive engine simulations in CONVERGE CFD capable of supporting the future design of high-efficiency engines operating on the anode tail-gas fuel. The flow chart in Figure 11 illustrates the process for designing the gasified engine that operates on Anode Tail-gas with CAE and experimental testing. The flow chart starts with the CFR engine's experimental data, which is then used to develop a TPA model in GT-Power.

Flame Speeds in CHEMKIN, a chemical kinetical solver used to develop a combustion/knock model in GT-power. The Two GT-Power models and experimental data are then combined to develop a predictive model in GT-Power and CONVERGE CFD. The predictive models are then calibrated, and the data collected will help inform on the new combustion chamber design in CFD. The new combustion chamber design will inform the new gasified engine's decisions, the 993T Kohler engine. The experimental data collected from the gasified engine will lead to iterative re-designs in the predictive model until the desired 35 % brake efficiency is achieved for the CFD predictive model.

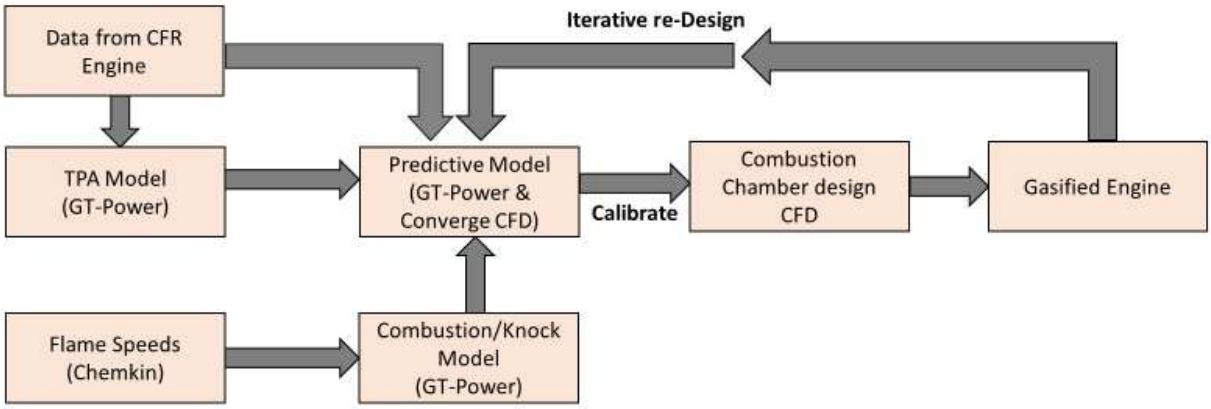

Figure 11: Project workflow chart for CAE tool design

4.2 CFR engine: CFD approach

This is the first study attempt to develop 3-D engine simulations with a syngas like fuel called “anode tail-gas fuel,” to the best of our knowledge. An adequate chemical mechanism had to be found that correctly captured the anode tail gas fuel's chemical behaviors under engine conditions. The CFR engine was selected to assist in this goal. The specifications of the CFR engine are indicated in Table 1.

Table 1: CFR Engine Characteristics

Crankcase Type	Model CFR-48D, Cast Iron
Cylinder Type	Cast Iron, Flat Combustion Surface, Integral Coolant Jacket
Displacement [cc]	611.73
Bore Diameter [mm]	82.55
Stroke [mm]	114.3
Adjustable Compression Ratio	4:1 to 18:1
Speed [RPM]	900-1200

Since the fuel was highly diluted, there were concerns with fuel combustibility. Thus, the anode tail gas was cooled to drop out some of the water and improve the fuel's lower heating value and increase the overall reactivity. To this extent, seven different fuel blends were developed and experimentally tested to determine if lowering the fuel's dilution would improve its performance. More on this research can be found in Balu et al., where it was determined that two fuels, namely the 40° and 90° C dew point fuel blends, performed adequately for further inspection to be taken.[45] The composition of these two fuel blends can be seen in Table 2 and compared to the original fuel blend with no water dropout.

Table 2: Anode Tail-Gas mole fraction composition for no water dropout, 90° C dew point dropout, and 40° C dew point fuel blends

	No Water Dropout	90° C Fuel Blend	40° C Fuel Blend
H2	17.7 %	26.35 %	33.64 %
CO	4.90 %	7.29 %	9.31 %
CH4	0.40 %	0.60 %	0.76 %
CO2	28.3 %	42.13 %	53.79 %
H2O	48.7 %	23.63 %	2.5 %

A previous study examined the use of three chemical mechanisms (namely, San Diego [46],GRI [47], and NUIG [48]) on modeling the combustion behavior of the anode tail gas using the predictive combustion-modeling feature in GT-Power. San Diego (SD), created to model natural gas, has 57 species and 268 reactions. GRI, also created for natural gas, has 53 species and 325 reactions, whereas NUIG, designed to model syngas fuels, contains 15 species and 48 reactions. The three-pressure analysis (TPA) approach was used to tune a GT-Power model of the CFR engine operating on the dilute tail gas fuels. More specifics on the GT-Power modeling approach can be found in Padhi et al. [49] NUIG mechanism was found to represent the fuel in terms of combustion and knock tendencies the best and, for those reasons, was selected to be used in CFD simulations [49]. Padhi et al. also proved that methane could be removed from the fuel since it made up such a small amount of the anode tail gas composition.

While performing initial CFD simulations, it was notable that the mechanism was very reactive for all the cases, causing very high pressure and would even demonstrate knock in cases where knock was not observed in the experiments. This led us to look more closely into the NUIG mechanism, where an odd behavior was identified when used by the CONVERGE CFD

software. Figure 12 depicts a difference in the ignition delay and flame speeds for the NUIG mechanism discussed in Padhi et al., named "NUIG 2013," depending on the software used to solve the chemical reaction calculations. As discussed in Padhi et al., NUIG 2013 had an OH radical mentioned as "OH*" that was assumed to cause trouble in the GT Power simulations; however, after further investigation in CHEMKIN and GT Power it was found to be negligible. However, this OH radical did show a difference when investigated in CONVERGE when calculating flame speeds and ignition delays, as shown in Figure 9. The overall mechanism showed differences in both ignition delay and flame speeds when solved with the CONVERGE chemical kinetic solver. Fortunately, when looking at Galway's website, another newer NUIG mechanism called "NUIG 2017" had 44 species and 251 reactions.[48] The NUIG 2017 mechanism had better results when comparing CHEMKIN and CONVERGE and showed slight differences in flame speeds compared to NUIG 2013 in CHEMKIN. Also, the NUIG 2017 mechanism did not change any of the results from Padhi et al. and showed better agreement in CFD engine simulations. These results led to making NUIG 2017 the mechanism that was used in all simulations going forward.

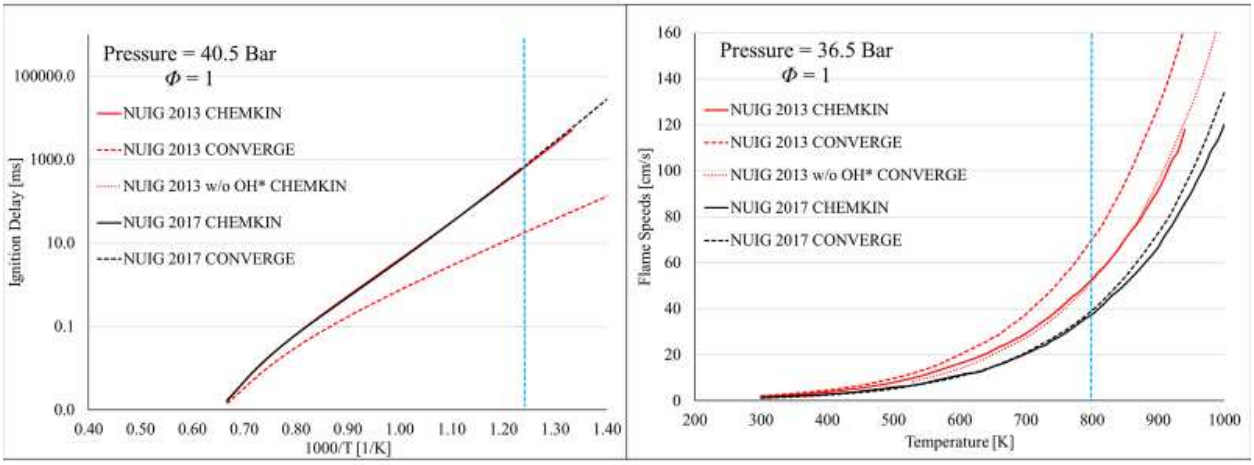

Figure 12: Ignition Delay and Flame speed comparison for NUIG 2013 (Red) and NUIG 2017 (Black) in two different software: CHEMKIN (solid lines) and CONVERGE (dashed lines)

The 3-D geometric model for the CFR engine was generated from an X-ray scan performed by Argonne National Laboratory and incorporates realistic geometry features like intake ports and a knock meter cavity, as seen in Figure 13. The temperature and pressure for the three regions' initial conditions (Intake, Cylinder, Exhaust) were obtained from experimental data at the simulation start time of -360° ATDC, right before intake. The spark source diameter used at the gap was 0.5 mm, and the spark timing was varied on a case-per-case basis. The maximum CFL limits used in all the intake and exhaust simulations were 2, 2, and 50 for convection, diffusion, and Mach, respectively. The maximum CFL limits used in all the compression and combustion simulations were 5, 2, and 50 for convection, diffusion, and Mach, respectively. A Mach CFL limit of five was used after spark timing to reduce the time step and better capture the rapid increases during knock, which was an acceptable value from Yue et al.[50]

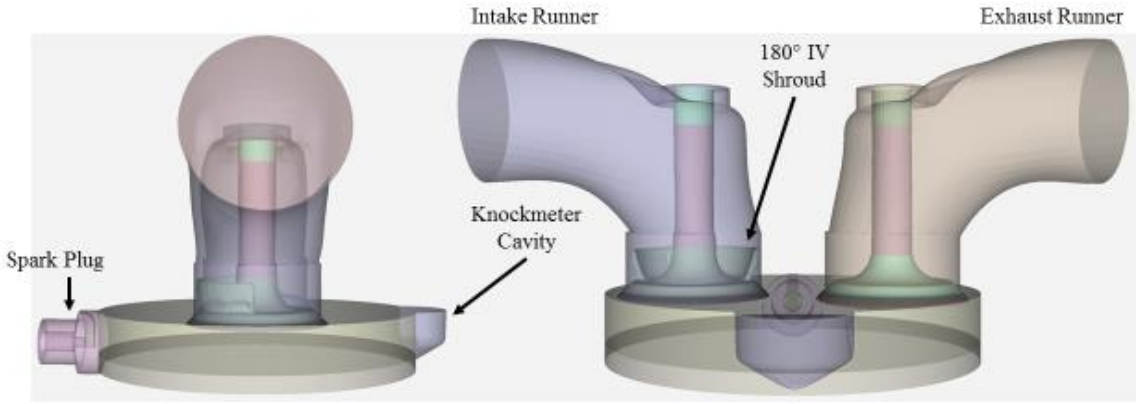

Figure 13: Transparent view of the CFR 3-D geometry with key geometric features highlighted.

Both lift profiles for intake and exhaust valves can be seen in Figure 14, and the added

valve lashing profile used to further improve the engine's fluid flow. A base mesh 4 mm was used for all simulations with boundary embedding placed one layer thick on all boundaries to

reduce cell sizes to 0.5 mm. A region embedding was specified to refine the mesh to 1 mm at the cylinder to better capture flow and combustion inside the cylinder.

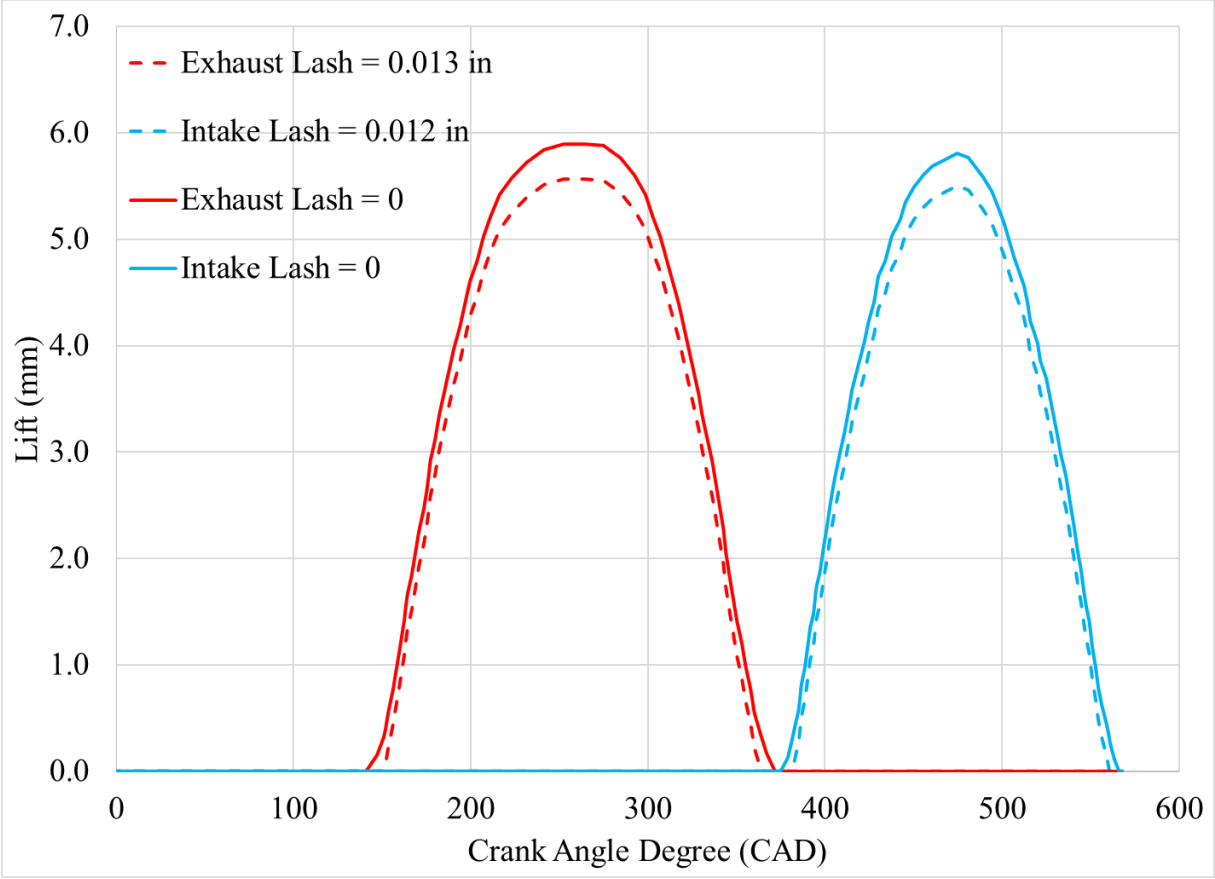

Figure 14: Valve lift profile for both intake and exhaust (Blue & Red Solid lines) while a dashed line indicates the valve lashing adjustment

Five cases were selected from CFR engine experimental data to be validated with the CFD model developed, and the test results of these cases can be seen in Table 3. Cases 1 and 2 were randomly selected from all experimental test points to begin the initial simulation setup and demonstrate the ability to modeling different CRs. Case 3 was selected because it was a test point that achieved a high knock index of 1036, according to Padhi et al. In Padhi et al., a test point with a knock index higher than 300 was considered consistent knocking cases. Case 4 and

5 were selected because they achieved the highest efficiency for both the 40° C and 90° C test blend with the Response Surface Method optimization used in Balu et al.

Table 3: Validated Case Experimental Parameters

Parameter	1	2	3	4	5
Fuel Test Blend Dewpoint [ºC]	40	40	40	40	90
CR	10.65	12.14	12.14	9.53	12.75
Ignition Timing [º ATDC]	-15.0	-13.0	-21.0	-15.9	-21.4
CA50 [° ATDC]	10.18	14.09	2.32	11.04	11.61
Speed [RPM]	939	939	938	952	1075
Inlet Temperature [°C]	79	80	80	47	70
Boost Pressure [kPa]	146	147	147	192	234
Total Fuel Flow [g/min]	170	170	169	219	275
Energy Flow (LHV·$\dot{m}fuel$) [kW]	12.94	12.88	12.89	16.61	17.78
Electric Power [kW]	1.93	1.90	1.79	3.31	3.55
Maximum Brake Efficiency [%]	16.64	16.50	15.56	22.24	22.33
Average Peak Pressure [kPa]	5430.0	5421.7	8271.4	7563.8	8955.0
Peak Pressure COV [%]	3.37	3.39	2.53	3.91	6.99
Average IMEP [kPa]	800.0	795.2	779.7	1145.3	1105.2
IMEP COV [%]	1.18	1.19	1.24	4.93	3.53

4.3 CFR Results and Discussion

The CFD simulations were set up to replicate the mean pressure and AHRR for the 1000 cycles taken in experiments. Table 4 shows the CFD error in total trapped mass to experimental

data, which was the first method for comparing the experimental data to simulated data. Table 4 shows that cases 1-4 all had less than a 5 % error when replicating the total trapped mass during a single cycle. GT Power and CONVERGE recommend that total trapped mass error should be less than 2.5 %. However, since this fuel is highly diluted with high combustion products, it was agreed that increasing the error limit to 5 % was sufficient for the anode tail-gas fuel. Only case 5 had a greater than 5 % error in total trapped mass, and this could stem from the fact that it is the only case with the 90° C fuel blend, which is even more diluent than the 40° C fuel blend. A similar trend was seen in Padhi et al., where the cases that used the 90° C fuel blend in GT Power had errors greater than 5 %. It is safe to say that the 90° C fuel blend is more challenging to simulate than the 40° C fuel blend, and further investigation is required if the 90° C fuel blend is selected to be used in the final gasified engine.

Table 4: Simulated total trapped mass percentage error to experimental data

	1	2	3	4	5
Trapped Mass Error [%]	3.05 %	3.54 %	3.13 %	2.26 %	10.95 %

The simulated data was deemed acceptable if the results were close to the experimental meanwhile staying within the 1000 cycles' limits for each case. Figure 15-Figure 19 demonstrates the pressure and AHRR curves for all 5 cases. The simulated data plotted in red, the experimental mean represented by a black dotted line, and the 1000 cycles in light gray solid lines. All 5 cases were deemed acceptable; however, most cases demonstrated a need for better

spark modeling techniques since the pressure rise was slow right after sparking timing, and a similar trend was seen in the AHRR.

Greater confidence in the simulation data came when the maximum relative error in IMEP prediction was less than 8 % and less than 4 crank angle degrees for CA10 and CA50.[8] Yue and Som et al. performed similar research on modeling the CFR engine and met the same maximum relative errors for IMEP, CA10, and CA50. However, the combustion model they used was G-equation, and they used a more traditional fuel in their research. Both simulated models proved acceptable in representing the CFR engine in various test conditions, even with those discrepancies. Since efficiency is such an important value for developing this anode tail gas engine, the maximum relative error for indicated efficiency would be less than 10 %. From Table 5, it is clear to see that all the cases met the maximum relative errors for IMEP, CA10, CA50, and indicated efficiency except for case 5, which had an efficiency error greater than the limit; however, it is also the only case with the 90° C fuel blend. Meaning that it could have more uncertainty in water dropout during experiments or could be more difficult to model since Padhi et al. had a similar problem when modeling the 90° C fuel blend.[49] The two cases with the least deviations were cases 1 & 3; however, all the cases validated the CFD model to be an accurate representation of the experimental testing. In Figure 17 & Figure 19, by observing the experimental data for cases 3 and 5, it is plain to see that knock occurs in both cases due to the rapid increase in pressure. To replicate these similar knock conditions seen in experimental data due to cycle to cycle variation in the single-cycle CFD analysis, the in-cylinder gas temperature was increased by 4 % and 1 % at the beginning of compression for cases 3 and 5, respectively.

Table 5: IMEP, CA10, CA50, and indicated efficiency (η) absolute errors for all simulated cases. Compared to similar maximum relative errors as Argonne National Labs [8]

Cases	IMEP	CA10	CA50	η [pts]
1	0.51 %	0.3°	0.3°	1.6 (7.64 %)
2	6.62 %	1.6°	0.5°	0.6 (2.00 %)
3	4.35 %	2.8°	0.1°	0.1 (0.3 %)
4	0.64 %	0.5°	1.0°	2.4 (0.3 %)
5	6.30 %	3.5°	1.3°	5.25 (13.4 %)
Maximum Relative Error [8]	<8 %	<4.0°	<4.0°	<10 %

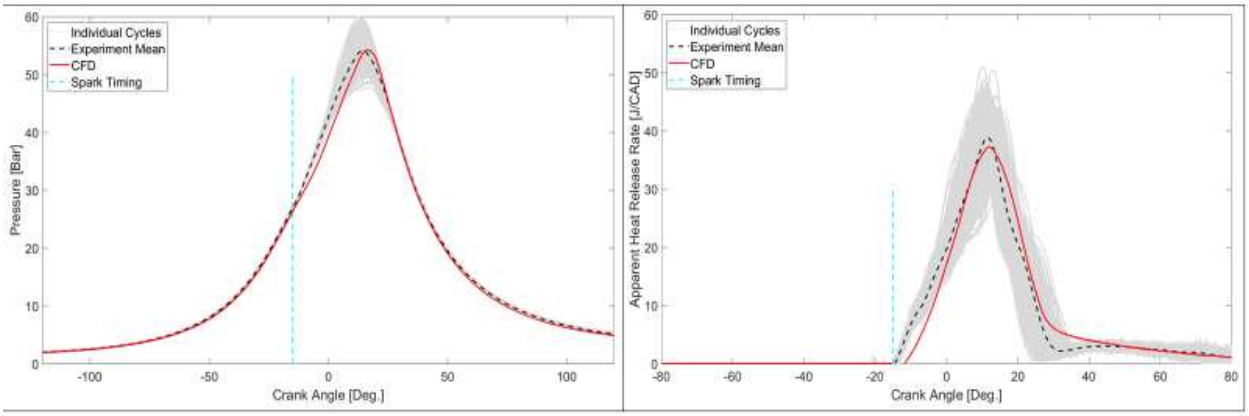

Figure 15: Case 1 simulation (red) validation of pressure (left) and apparent heat release rate (right) compared to the 1000 cycles of experimental data (gray), and experimental mean (black)

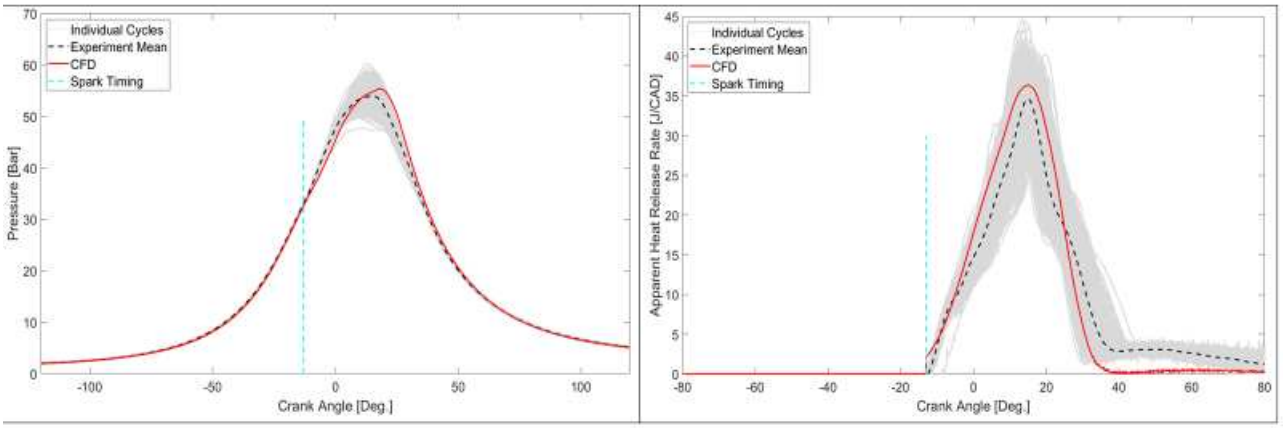

Figure 16: Case 2 simulation (red) validation of pressure (left) and apparent heat release rate (right) compared to the 1000 cycles of experimental data (gray), and 1000 cycle average (black)

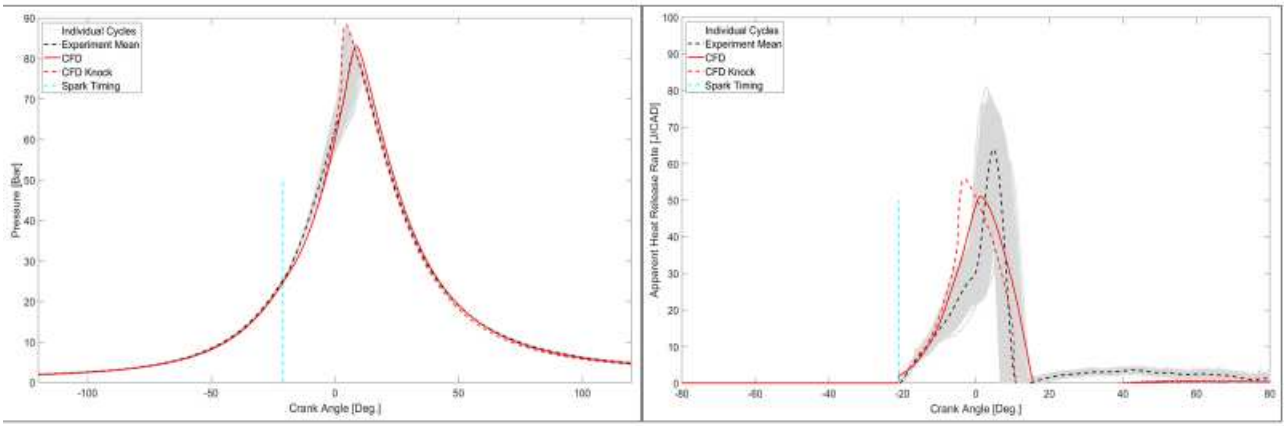

Figure 17: Case 3 simulation (red) validation of pressure (left) and apparent heat release rate (right) compared to the 1000 cycles of experimental data (gray), and 1000 cycle average (black)

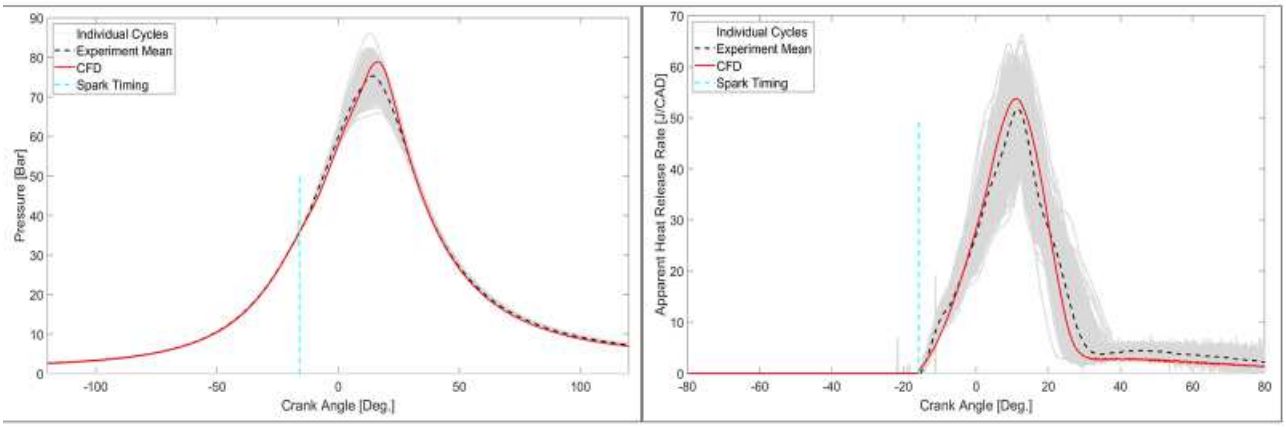

Figure 18: Case 4 simulation (red) validation of pressure (left) and apparent heat release rate (right) compared to the 1000 cycles of experimental data (gray), and 1000 cycle average (black)

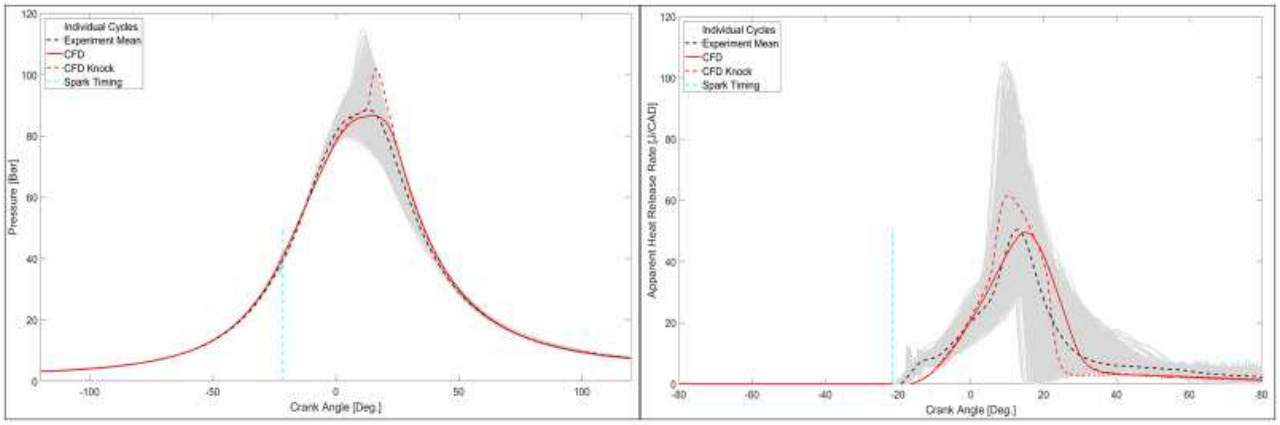

Figure 19: Case 5 simulation (red) validation of pressure (left) and apparent heat release rate (right) compared to the 1000 cycles of experimental data (gray), and 1000 cycle average (black)

With the model validated, greater confidence comes from the fact that the characteristics observed by CFD data are representative of what is developing in the engine's combustion chamber during operation. This allows us to make deeper inquiries into the developments of knock predictions, knock limits, and changes that come from new engine designs. For instance, Figure 21 & Figure 22 illustrate the flame propagation for cases 2, 3, and 5 by using a temperature iso-surface of 2000 K in the post-processing software, EnSight. It is notable from

Figure 20 that the flame will propagate in the swirl direction created in the combustion chamber, which for the CFR engine is a clockwise swirl looking up from the top of the piston. This causes the fuel to be consumed first near the intake and then travel to the exhaust side. This knowledge will be elaborated further and become more helpful in the next section when looking at the gasified engine's investigation. When looking at the other iso-surface in Figure 21, another analysis can be made, which involves predicting knock and when an engine is at borderline knock conditions. The blue iso-surfaces in Figure 21 & Figure 22 are of the average mass fraction for H_2O_2, a combustion radical, and a precursor to high-pressure hydrogen auto-ignition. If the pressure and temperature are hot enough at the end-gas where H2O2 resides, it will cause a breakdown of H2O2 into two OH radicals causing a chain propagation that ultimately leads to ignition. However, this combustion at the end gas will flow in the opposite direction of the swirl as better depicted in Figure 22, and when the two opposing flames clash, it will cause a knocking sound in the engine, which is where the term engine knock stems. In essence, when H_2O_2 builds up at the end gas of an engine, it hints that the engine is at border-line knock conditions and might experience knock with continued use. On the other hand, when an engine experiences normal combustion conditions, there is fewer H_2O_2 build-up, and it stays within the flame, as can be seen for case 2 in Figure 21 when compared to the high knock index case.

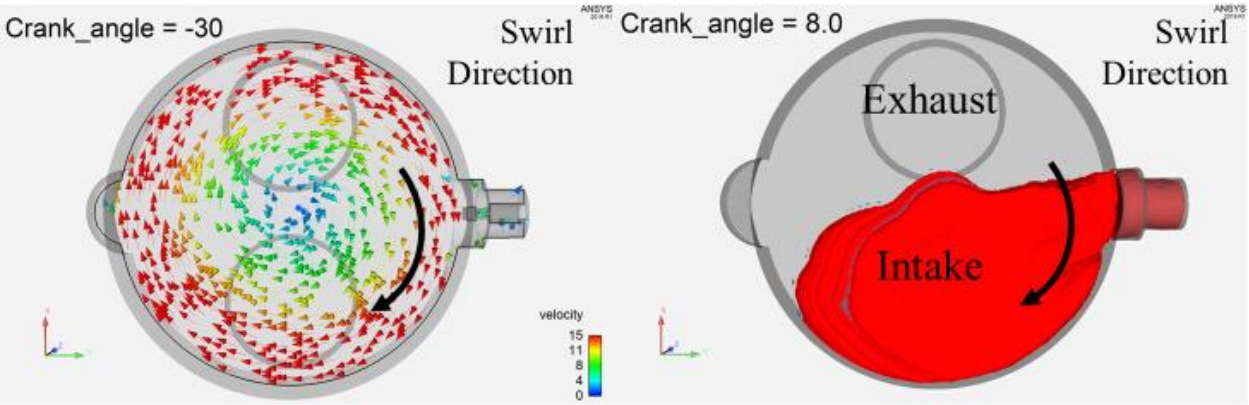

Figure 20: Velocity vector profile at -30° ATDC (left) compared to the flame propagation at 8° ATDC (right) indicated by an Iso-surface at 2000 K (Red)

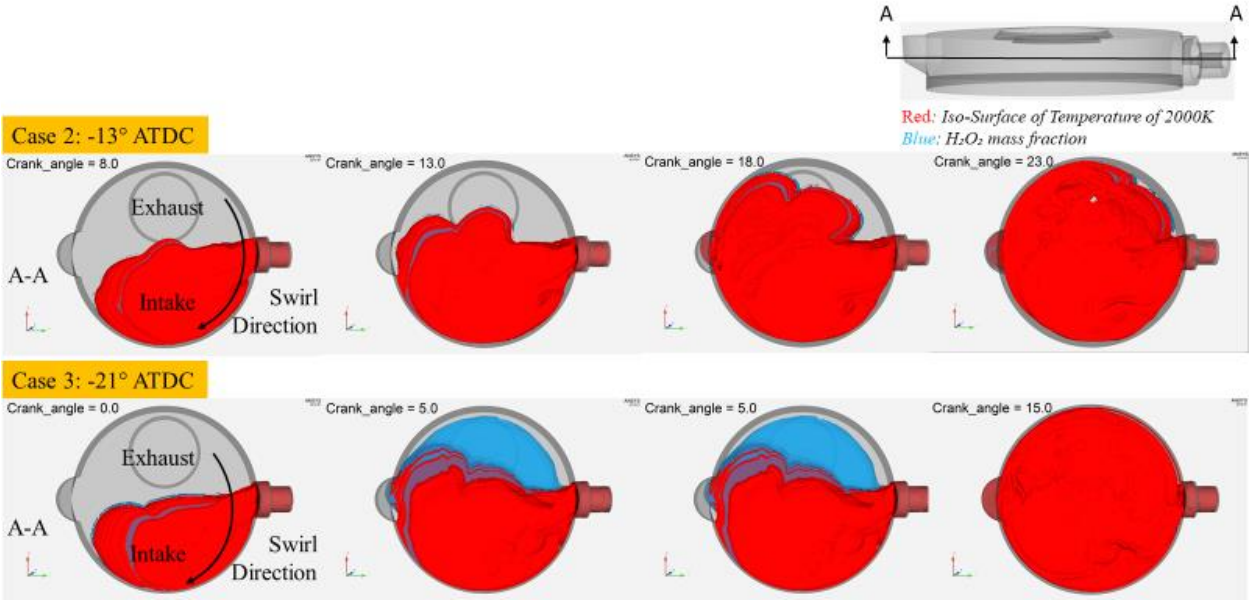

Figure 21: Temperature Iso-surface at 2000 K (red) to represent flame propagation and average H_2O_2 mass fraction Iso-surface (blue) for cases 2 (top) & 3 (bottom) with case 2 crank angle images advance by 8° to compare accurately with the spark timing of case 3

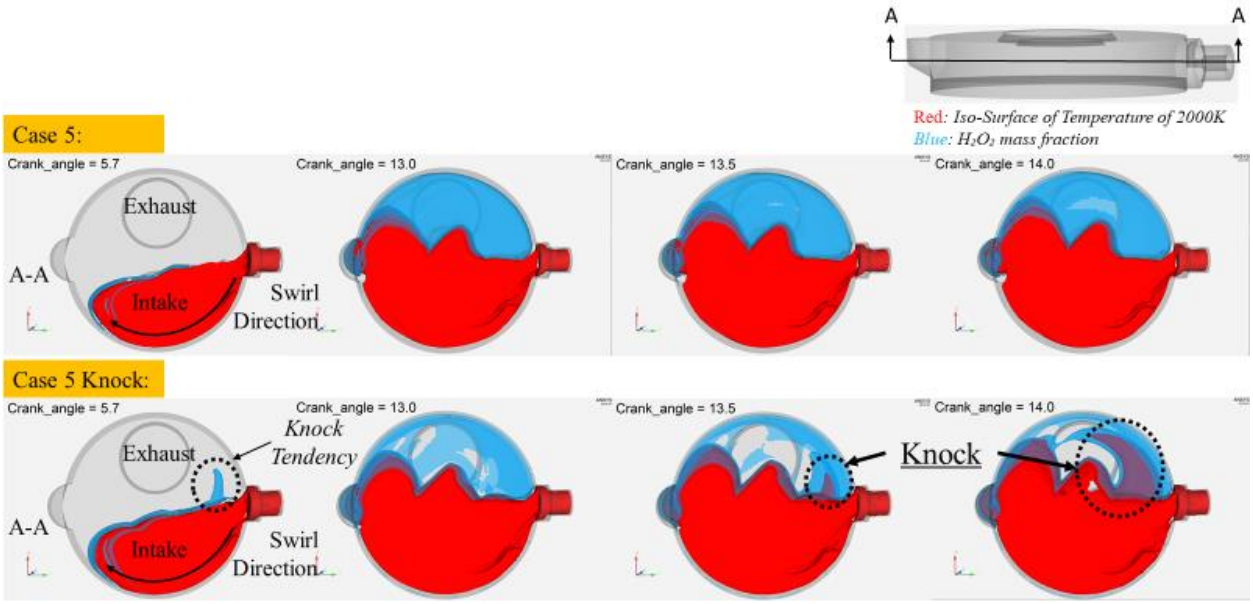

Figure 22: Temperature Iso-surface at 2000 K (red) to represent flame propagation and average H_2O_2 mass fraction Iso-surface (blue) for cases 5 with (bottom) and without knock (top)

The knowledge and techniques taken from the CFD modeling of the CFR engine will be taken and applied to the gasified Kohler engine modeling that will be discussed further in the upcoming section.

4.4 Kohler anode tail-gas engine: CFD approach

This work's goal was to retrofit a compression ignited diesel engine into a spark ignited anode tail gas engine, as discussed in Braun et al. [44]. This work was carried out simultaneously with experimental testing and GT Power modeling of the retrofitted Kohler engine, which is discussed more in-depth in Countie et al. [51] Through a partnership with Kohler Power Co. on this project, the 993L Kohler engine was selected and provided by them, the specifications of which are listed in Table 6. Again as was concluded from the previous work, NUIG 2017 mechanism best represented the fuel in terms of combustion and knock tendencies; thus, it was selected again to represent the chemical reaction in CFD simulations of the anode tail gas. [49]

All the simulations were performed using the 40° C fuel blend since it was best represented in the CFR engine simulations.

Table 6: KDW993T Original Engine Characteristics

Displacement [cc]	993
Configuration	Inline 3 Cylinder
Compression Ratio	21:1
Injection	Unit pump injector with swirl pre-chamber
Forced Induction	Turbocharger with internal wastegate
Power [kW] at 4500 RPM	41.9
Torque [N*m] at 3800 RPM	96.5
Minimum BSFC [g/kWh] at 2600 RPM	238.6
Maximum Speed	4600 RPM

The Kohler Power Co. provided the 3-D geometric model for the Kohler engine in SOLIDWORKS and incorporated many realistic geometry features like intake ports, turbocharger, etc. The engine model was drastically reduced to integrate only the components necessary for a single cylinder. Then the mold feature was used in SOLIDWORKS to create a shell of the engine. This shell was then imported into CONVERGE and the geometry cleanup discussed in Chapter 3: General CFD Methods was conducted to prepare the model for engine simulations. The final product of the model can be seen in Figure 23. The temperature and pressure for the initial conditions of three regions (Intake, Cylinder, Exhaust) were established from GT Power at the simulation start time of -385° ATDC, right before intake. The spark source diameter used at the gap was 0.5 mm, and the spark timing was set at -23° ATDC because

GT power identified this spark timing for the most efficient point from the research performed in Countie et al. [51]

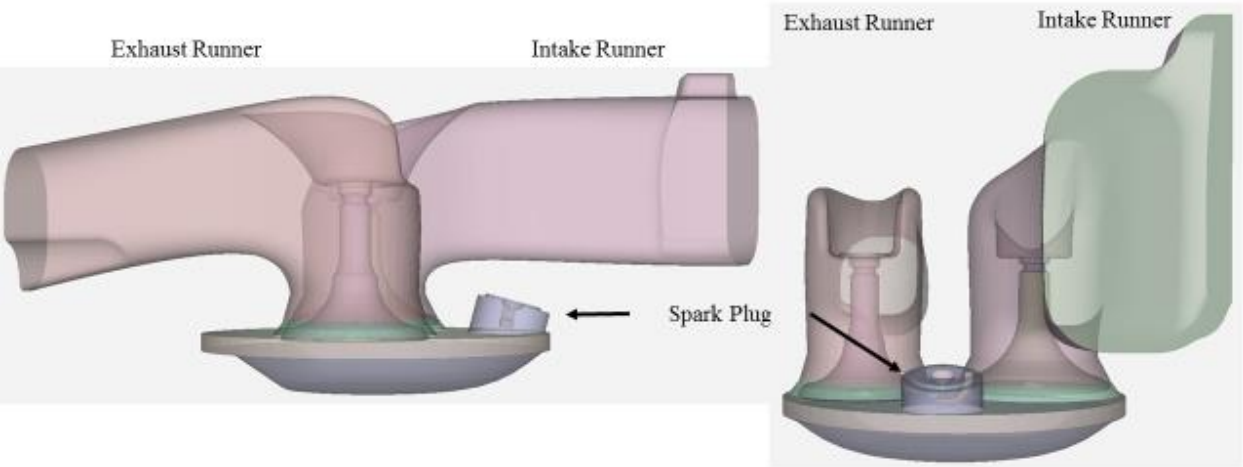

Figure 23: Transparent view of the Kohler engine 3-D geometry with key geometric features highlighted

The original CR of the engine was 21; however, in Countie et al., a CR sweep was performed to determine the CR with the greatest efficiency and operation knock margin. For that reason, a new piston was designed by Davinvi Engineering to meet a CR of 17. Through model validation in GT Power, it was noticed that the simulation error was greater at high speeds, and Kohler Power Co. mentioned that high-speed operation was not desirable due to the decreased bearing life. The case that matched experimental data the best was at 1600 rpms with a spark timing of -23° ATDC. The engine parameters in Table 7 were selected for CFD simulations and engine design investigations through the help of GT Power and experimental data.

Table 7: CFD Kohler engine parameters

Compression Ratio	Speed [RPM]	Sparking Timing [ATDC]	Intake Pressure [Bar]	Intake Temperature [K]	Exhaust Pressure [Bar]	Exhaust Temperature [K]
17	1600	-23°	1.51	323	1.61	874

The maximum CFL limits used in all the intake and exhaust simulations were 2, 2, and 50 for convection, diffusion, and Mach, respectively. The maximum CFL limits used in all the compression and combustion simulations were 5, 2, and 50 for convection, diffusion, and Mach, respectively. Both lift profiles for intake and exhaust valve can be seen in Figure 24. A base mesh 4 mm was used for all simulations with boundary embedding placed two layers thick on all boundaries to reduce cell sizes to either 0.5 mm or 1 mm depending on piston stroke timing. During intake, the boundaries in direct and initial contact to the flow, like the intake valves, received a 0.5 mm embedding and everything else received a 1 mm embedding. During combustion, everything received a 1 mm embedding. A course (0.5 mm) and fine (0.25 mm) spherical embedding was placed at the spark plug during compression to capture the flow velocities accurately.

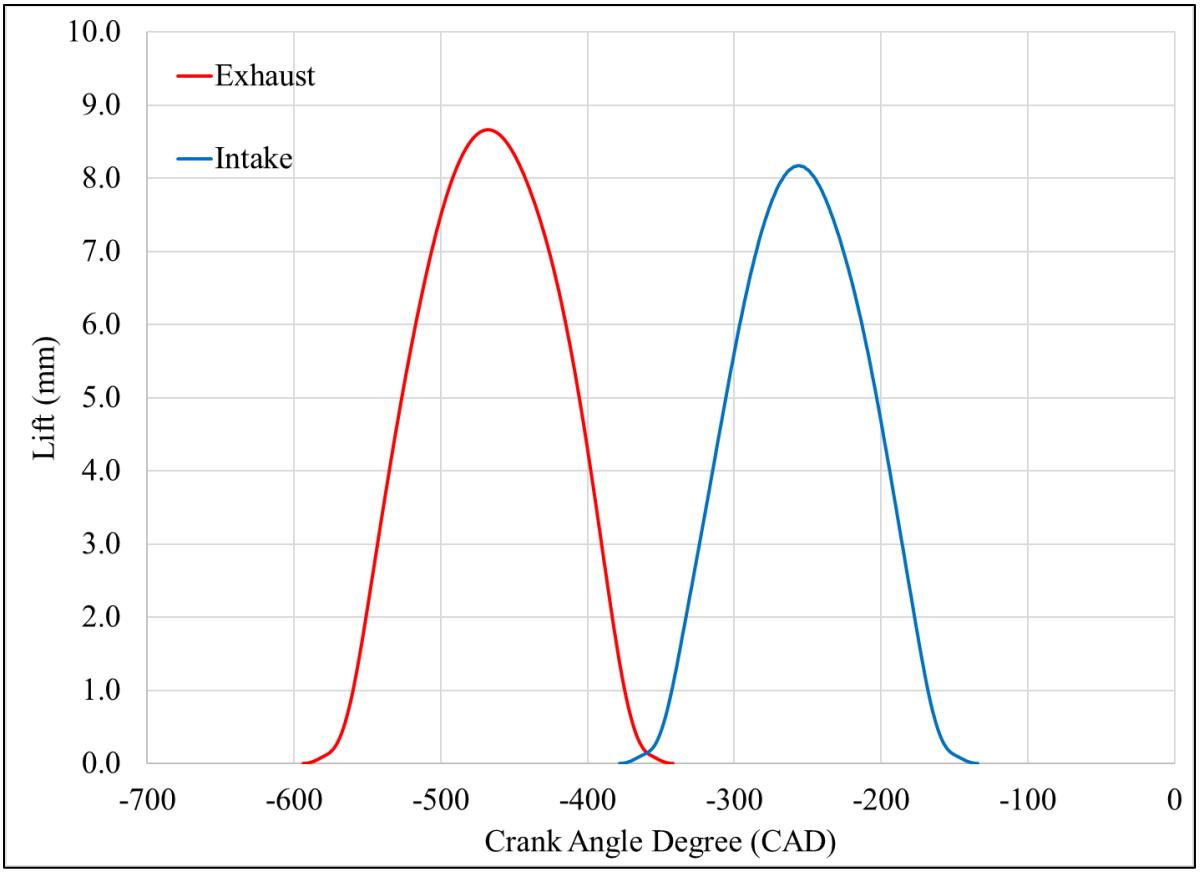

Figure 24: Valve lift profile for both intake and exhaust (Blue & Red Solid lines)

In Countie et al., the maximum brake efficiency achieved was at 31.25%; however, the system efficiencies need to be closer to 35 %, creating a need to update geometry, which is not accounted for in GT Power. With that in mind, the plan is to develop piston and spark plug design investigations in CFD to further increase efficiency that could offset possible errors down the line.

4.5 Kohler engine piston design: Results and Discussion

4.5.1 Spark Plug investigation

The spark plug was not centered because the fuel injector port was retrofitted to fit the spark plug. When first looking at the flow velocities in the combustion chamber, one thing stood out about the spark plug location. Figure 25 shows how the spark plug orientation causes the ground electrode to obstruct the swirl direction in the combustion chamber, which would inhibit flame propagation. Thus, the first spark plug configuration investigated is to rotate the spark plug 90°, as seen in Figure 26, to allow the flow to pass through the ground electrode, promoting flame kernel development.

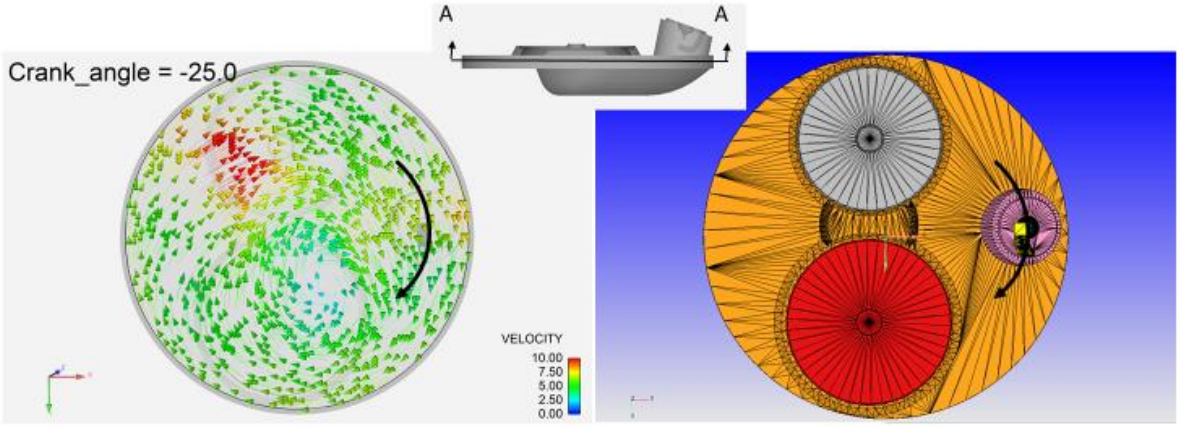

Figure 25: Flow velocities in the combustion chamber with the swirl direction indicated by a black line (left), Cross-sectional cut out of the combustion chamber with the swirl direction highlighting the plug orientation (right)

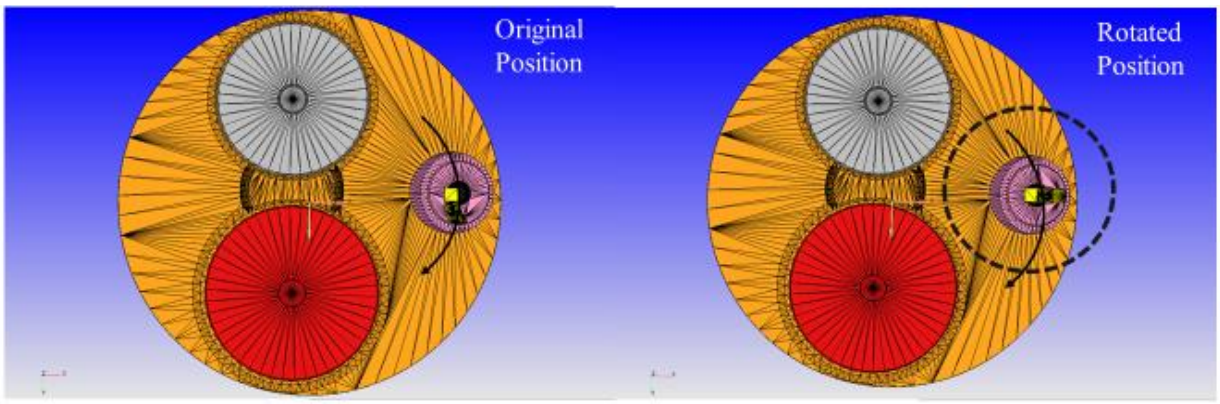

Figure 26: Cross-sectional cut out of the combustion chamber with the original spark plug orientation with the swirl direction indicated by a black line (left), the combustion chamber with the proposed spark plug orientation rotated by 90°

Another concern about the original spark plug orientation is that it is recessed into the combustion pre-chamber, potentially reducing performance due to flame quenching since the flame temperature may be reduced due to wall interaction before propagating into the combustion chamber. Figure 27 shows how the original spark plug extrudes out the combustion chamber, and it also shows how far the spark plug could impinge into the combustion chamber before colliding with the piston bowl. Three spark plug orientations were investigated to determine if they could improve the engine's performance and efficiency. The first is to rotate the spark plug by 90°, as indicated by Figure 26. The second is to lower the spark plug by 4 mm, as illustrated by Figure 27 (mentioned as LSPK), and the last one would be a combination of the two, which is to lower the spark plug and rotate it by 90° (mentioned as LSPK90). These three investigations were performed using the original 21 CR piston and the 17 CR piston developed by reducing the CR21 squish surface area. By lowering the spark plug, the CRs slightly increased, making the new CRs 21.96 and 17.62.

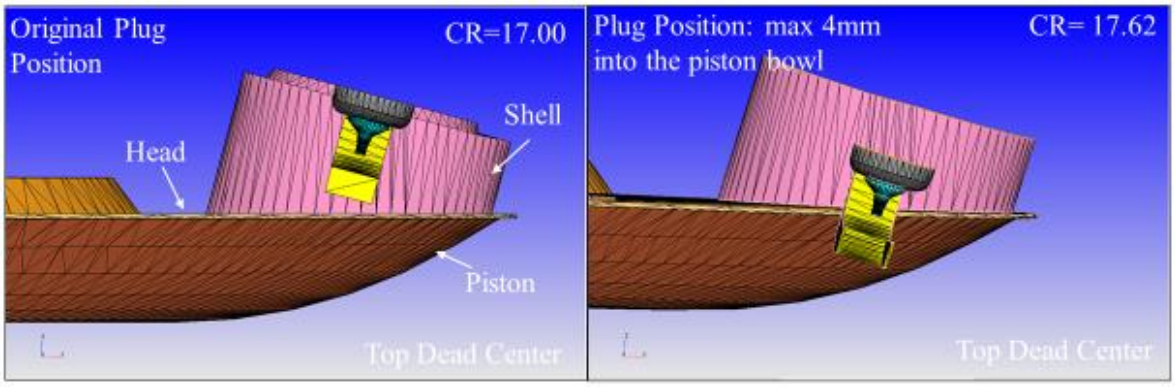

Figure 27: cross-section of the Kohler engine spark plug with the original plug position at TDC (left), a cross-section of the spark plug with the maximum allowable extraction into the combustion chamber at TDC (right)

Figure 28 and Figure 29 show that by simply rotating the spark plug by 90°, the combustion improved for both the CR17 and CR21 cases. This is due to the improved magnitude and direction of flow at the spark plug, shown in Figure 30, which shows the flow velocities at the spark plug for both spark plug configurations at CR17. Improving the spark plug's flow characteristics helps improve the flame kernel development and allows the flame to escape the spark plug shell quicker, resulting in a faster, more robust flame. This is better illustrated in Figure 31, which shows a red iso-surface at 2000 K, representing flame propagation in an IC engine from two different views. From the first view B, which is a zoomed-in view of the pre-chamber where the flame in the rotated plug configuration escapes first at -12° ATDC. The rest of the images in Figure 31 have an A-A view, a cross-sectional cut in the middle of the combustion chamber, and better depicted by the image at the figure's corner. The key takeaway from these images is that the flame is propagating faster for the rotated plug configuration at and it is better portrayed by a dotted black line at 4° ATDC.

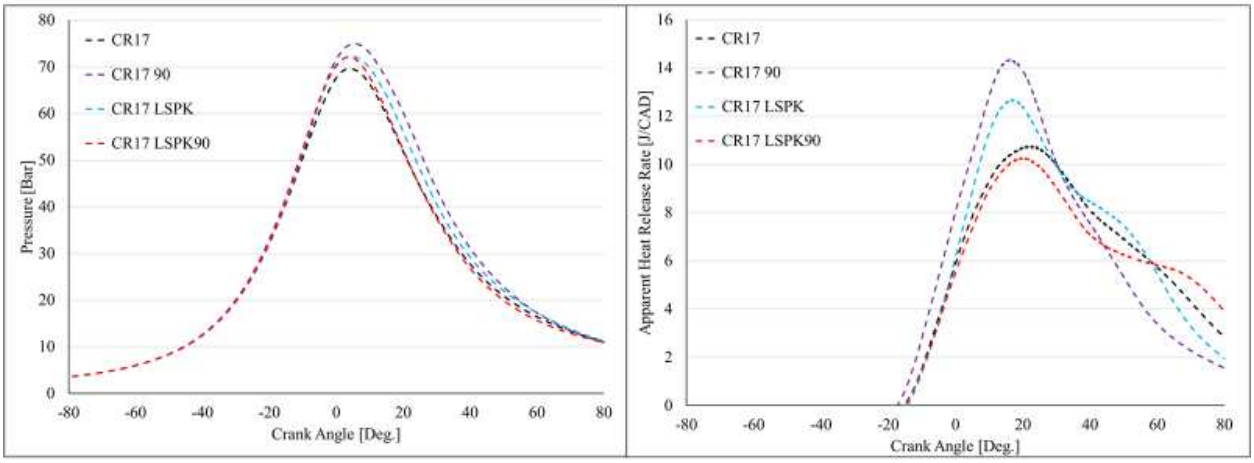

Figure 28: Pressure and AHRR curves for the four spark plug configuration with the CR17 Piston investigation with the original spark plug orientation (black), 90° rotated plug (purple), lowered spark plug (blue), and 90° rotated lowered plug (red)

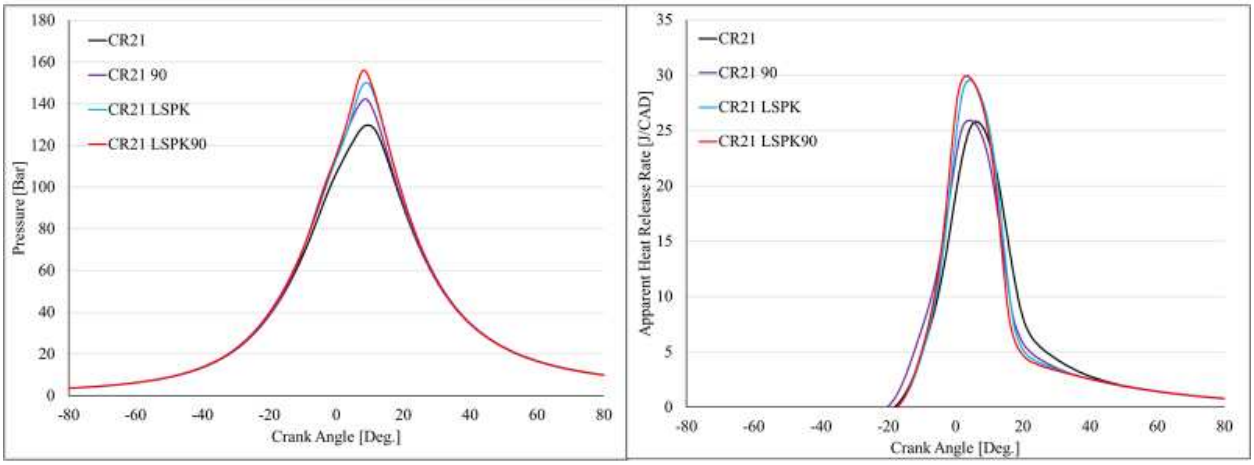

Figure 29: Pressure and AHRR curves for the four spark plug configuration with the CR21 Piston investigation with the original spark plug orientation (black), 90° rotated plug (purple), lowered spark plug (blue), and 90° rotated lowered plug (red)

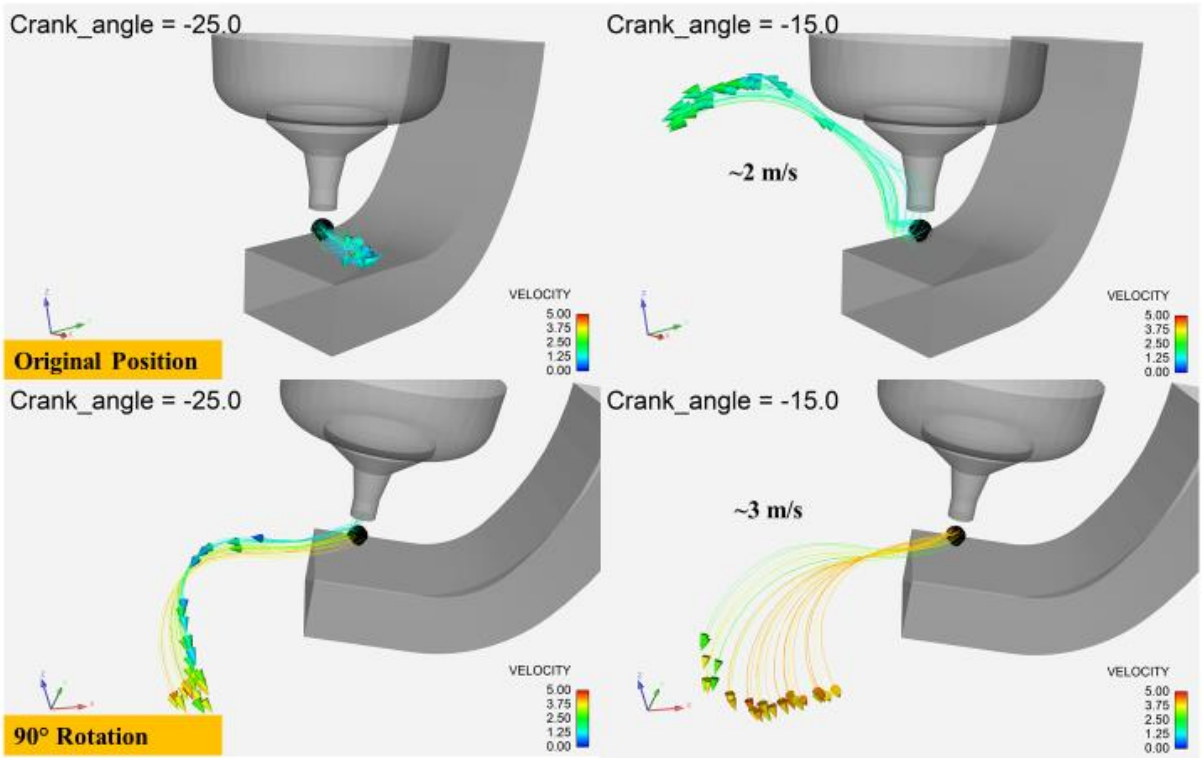

Figure 30: Flow velocities at the spark plug gap for the original (top) and 90 rotation spark plug configurations (bottom) at CR17. Spark timing is -23 ATDC

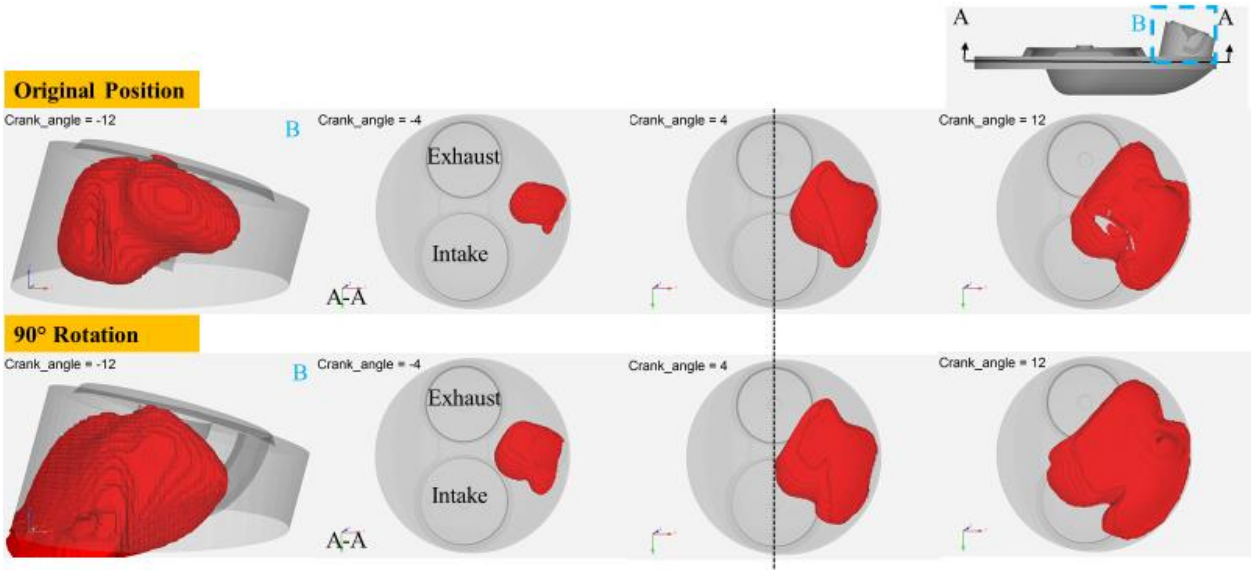

Figure 31: Temperature Iso-surface at 2000 K (red) to represent flame propagation for the original (top) and 90 rotation (bottom) spark plug configurations at CR17 from two different views: view B is a zoomed-in view of the spark plug (leftmost), view A-A is a cross-sectional cut at the middle of the combustion chamber indicated at the top right corner

When looking at Table 8 and Table 9, it is clear that the rotated spark plug configuration had a much greater improvement for the CR17 piston than for the CR21 piston, which increased efficiency by 3.36 percentage points (pts) versus only a 0.16 pts increase for CR21. Another thing that is very different from the spark plug investigations performed at CR17 and CR21 is the conflicting results seen from the lower spark plug configurations. As can be seen in Table 9 and Figure 29, there is a continuous improvement in engine performance from the original spark plug orientation to the most efficient case, which is the lowered rotated plug configuration at CR21 with an efficiency of 37.3 %. On the other hand, from Table 8 and Figure 28, the lower spark plug configuration shows an improvement to engine performance compared to the original configuration at CR17. However, it hinders performance when compared to just the rotated plug configuration. It is also notable that the least efficient case for the CR17 is the lowered rotated plug with an efficiency of 25.86 %. This could be because the flow velocities are much different for the CR17 piston since the squish area is smaller than the CR21 piston, but further investigation is required to determine the difference in performance.

Table 8: Indicated efficiency for the four spark plug configurations at 17 CR

	CR17	CR17 90	CR17 LSPK	CR17 LSPK90
η [%]	26.85%	30.21%	28.67%	25.86%

Table 9: Indicated efficiency for the four spark plug configurations at 21 CR

	CR21	CR21 90	CR21 LSPK	CR21 LSPK90
η [%]	36.18%	36.34%	37.19%	37.30%

One improvement from rotated and/or lowering the spark plug for both CR cases is the possible improvement in coefficient of variation (COV) due to the more uniform velocity magnitudes and direction at the spark plug gap. This is clearer from Figure 32, Figure 33, and Figure 34, which compares the velocity fields at the spark plug gap for the original vs. the rotated configuration, the original vs. the lower plug configuration, and the lower plug vs. the lower rotated plug configuration, respectively. Figure 32 shows that a vortex formulates around the center electrode for the original spark plug configuration, which could cause flame kernel stagnation and the varying speeds from 1.25 to 5 m/s could lead to an increase in COV. On the other hand, by rotating the spark plug, the vortex disappears and the flow is uniform in a single direction. Although the velocities still vary, the flame propagation will be more consistent. Figure 33 shows that the original spark plug configuration is now compared to the Lower spark plug configuration, which demonstrates a similar improvement in flow direction as the rotated plug configuration and displays a slight improvement in velocity variation from 1.25 to 3.75 m/s. Figure 34 shows that the lower spark plug configuration is now compared to the Lower rotated spark plug configuration, which displays similar uniform velocity direction and a tremendous increase in velocity magnitude consistency at 5 m/s. With more uniform velocity magnitudes and direction, more consistent flame kernel development and propagation can be expected in the engine to reduce COV.

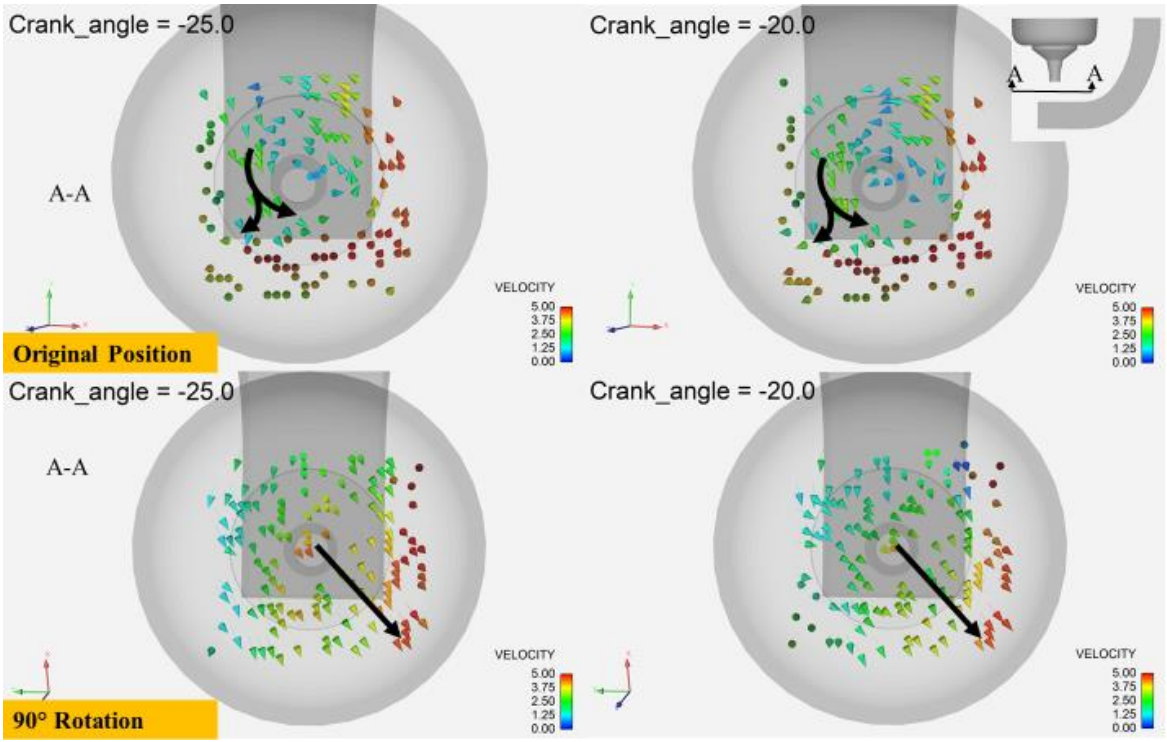

Figure 32: Flow velocity field at the spark plug gap for the original (top) and 90 rotation spark plug configurations (bottom) at CR17 with black arrows clarifying flow direction. Spark timing is -23 ATDC.

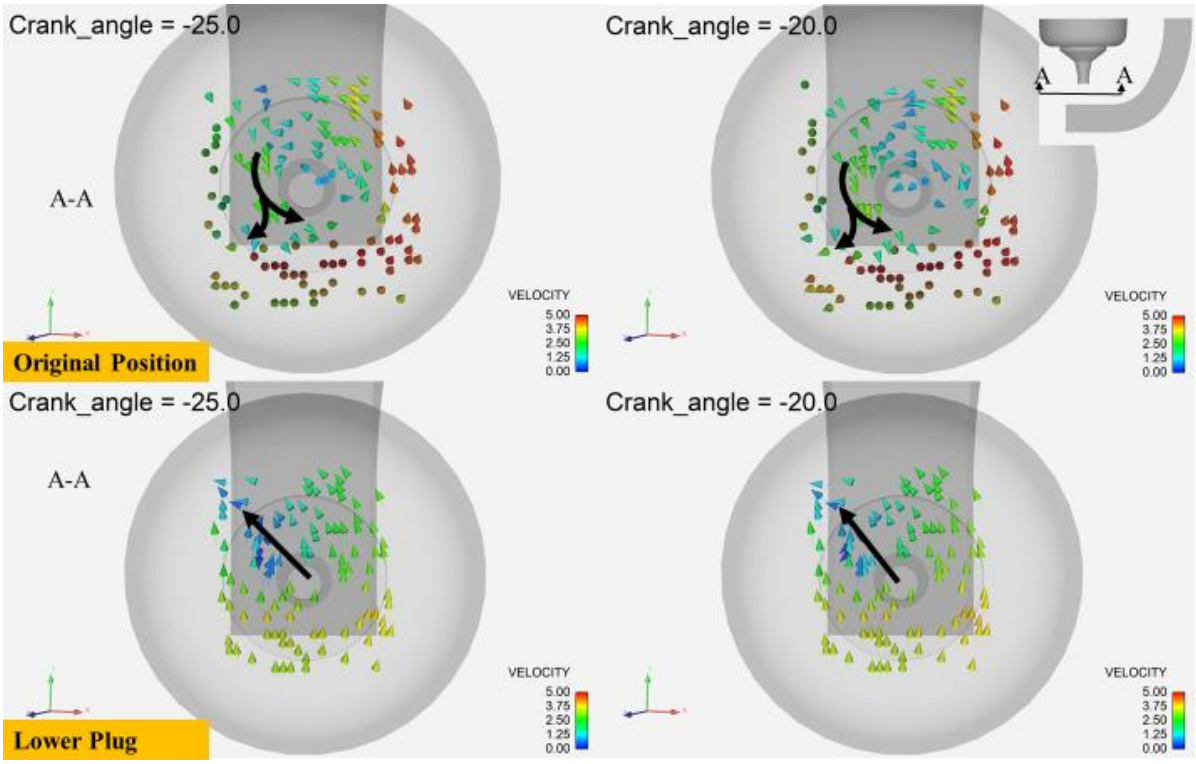

Figure 33: Flow velocity field at the spark plug gap for the original (top) and lower spark plug configurations (bottom) at CR17 with black arrows clarifying flow direction. Spark timing is -23 ATDC.

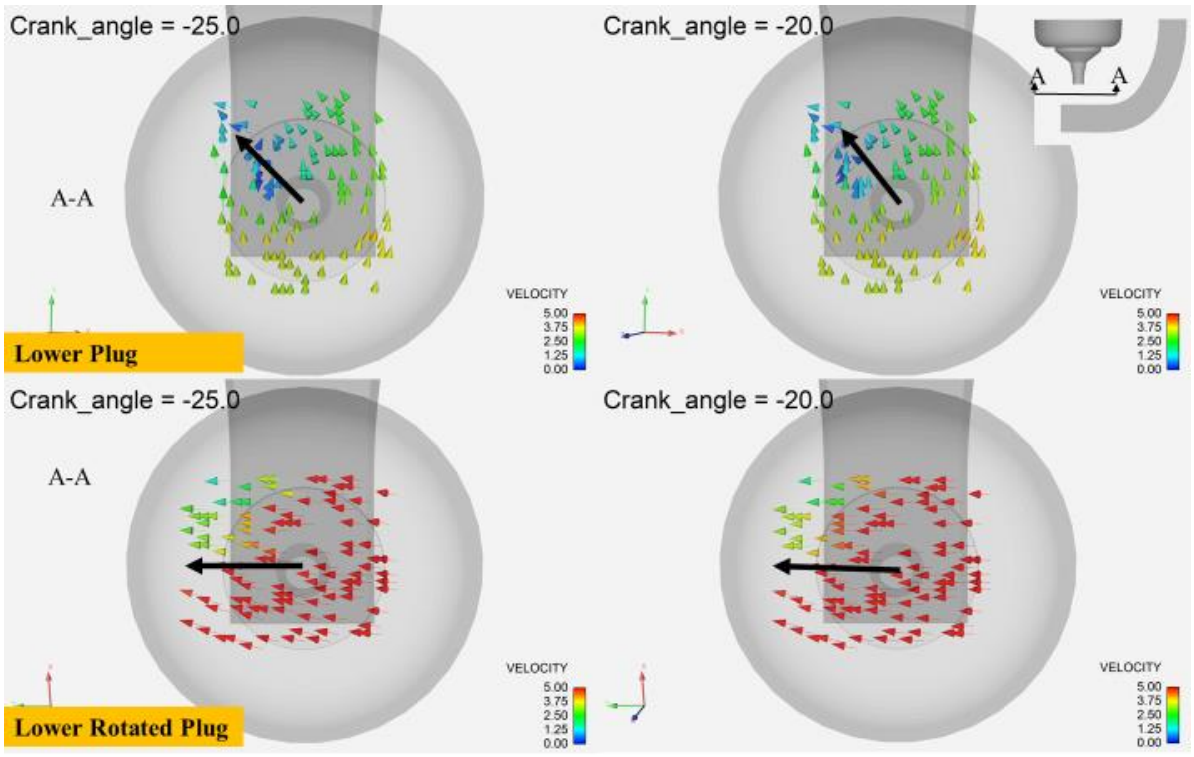

Figure 34: Flow velocity field at the spark plug gap for the lower (top) and lower rotation spark plug configurations (bottom) at CR17 with black arrows clarifying flow direction. Spark timing is -23 ATDC.

Future work should also focus on trying different levels of lowering the spark plug since only the 4 mm distance was investigated because it was the maximum allowable distance. However, with future improvements on piston bowl designs, this may not always be the case, and even a flush spark plug configuration should be studied.

4.5.2 1st Piston Investigation

For the first set of piston design investigations to improve efficiency, three common piston design parameters will be investigated: clearance height (Hcl), bowl depth, and squish size, indicated by the surface area of the flat piston region. The investigation setup is for two additional pistons to be designed by keeping at least one design parameter constant from the default piston designs and manipulating the other two parameters to still roughly holding a CR of

17. Figure 35 and Figure 37 show the images of 2 completely different piston designs used in the investigations for the three common piston design parameters.

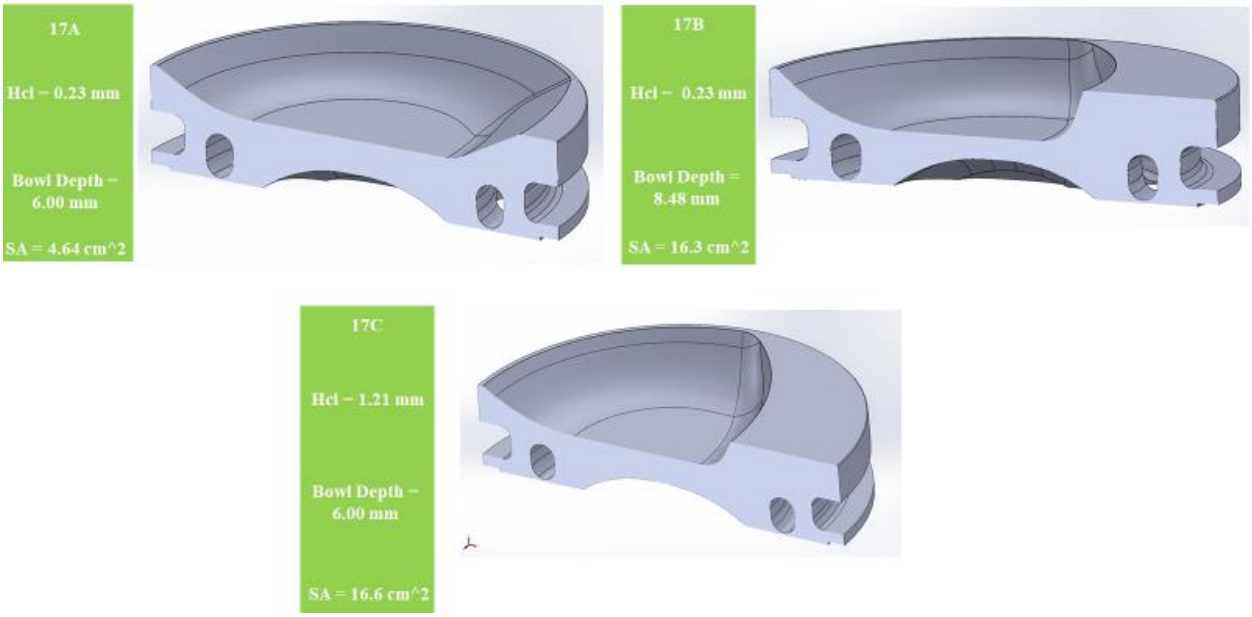

Figure 35: CR17 Piston investigation with clearance height in mm, bowl depth in mm, and surface area in cm^2 for 17A (top left), 17B (top right), 17C (bottom)

In the first investigation, the original CR17 piston from Davinvi Engineering (Figure 35: top left) had the bowl depth increased from 6.00 to 8.48 mm, and the squish surface area increased from 4.64 to 16.3 cm^2 to develop the piston design named “17B”. The piston called “17C” was created by increasing the clearance height from 0.23 to 1.21 mm and increasing the squish surface area from 4.64 to 16.6 cm^2. The Pressure and AHRR results from this investigation can be seen in Figure 36, where a black dotted line indicates CR17 design, a red line indicates 17B, and a blue line characterizes 17C. Figure 23 shows that 17B height and 17C both outperformed the 17A design in pressure and AHRR, and this is because they both had an increase in the squish area. However, when comparing 17B and 17C, it is difficult to determine which piston design was better by looking at pressure. The combustion in 17A is quicker, which is noted by

the higher AHRR, and it had better efficiency, as seen in Table 10 making 17B the better piston design. From Table 10 shows that the indicated efficiencies predicted by the CFD are lower than the brake efficiencies suggested by GT Power. This can be chalked up to the CFD and GT power models not being fully validated to experimental data causing the difference in the efficiencies. The Kohler GT Power model derived its turbulent flame speed model from the CFR engine GT Power model, which is a very big assumption since turbulent flame speed models are unique to every engine. This might explain why the brake efficiencies are higher from GT Power compared to the CFD data. Although this is subject to future work, it does not impact the results and conclusions in this study since we are only interested in improving the relative efficiencies.

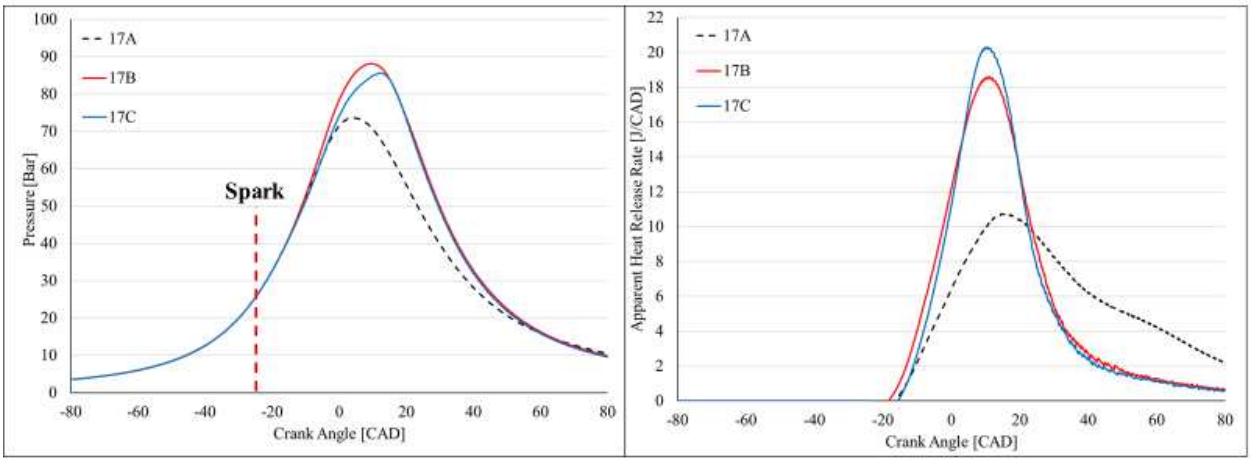

Figure 36: Pressure and AHRR curves for the three CR17 Pistons investigation with the original CR17 piston bowl design in black dotted line

Table 10: Indicated Efficiencies for the CR17 piston investigation

	η [%]
17A	26.85 %
17B	32.22 %
17C	31.76 %

4.5.3 2nd Piston investigation

The second piston investigation uses the original CI design piston from the Kohler engine, which has a large squish area of 30.3 cm^2 and is kept fixed for this investigation to obtain a better view of how clearance height and bowl depth play a role in combustion. The CI 17A piston is modified by increased the bowl depth from 4.25 to 6.00 mm and slightly decreasing clearance height from 2.93 to 2.45 mm to develop the piston design named "CI 17B". The piston named "CI 17C" was developed by drastically decreasing the clearance height from 2.93 to 0.17 mm and increasing the bowl depth from 4.25 to 15.1 mm. The Pressure and AHRR results from this investigation can be seen in Figure 38, where CR17 design is indicted by a black dotted line, CI 17B is indicated by a red line, a blue line indicates CI 17A, and CI 17C is

characterized by a purple line. Figure 25 shows that CR17 CI Squish outperformed all the other designs in pressure and AHRR because it has a much smaller clearance than the other CI piston designs a greater squish area than the CR17 piston. The past two-piston investigations give a clear picture that a large squish area and a small clearance height are causes for improved peak pressure and AHRR due to the faster combustion. However, the last parameter of bowl depth is not so explicit in how it improves combustion. Bowl depth could be determined if another piston investigation is performed, but for this investigation, bowl depth must be large to account for the large squish area and a small clearance height while still trying to keep the same CR. One thing to be cautious of is even though a large squish area and small clearance height demonstrate to improve combustion. These piston design parameters can also have the opposite effect and cause high pressures and temperatures at the end gas, which could lead to knock conditions, although no knock was detected in these cases.

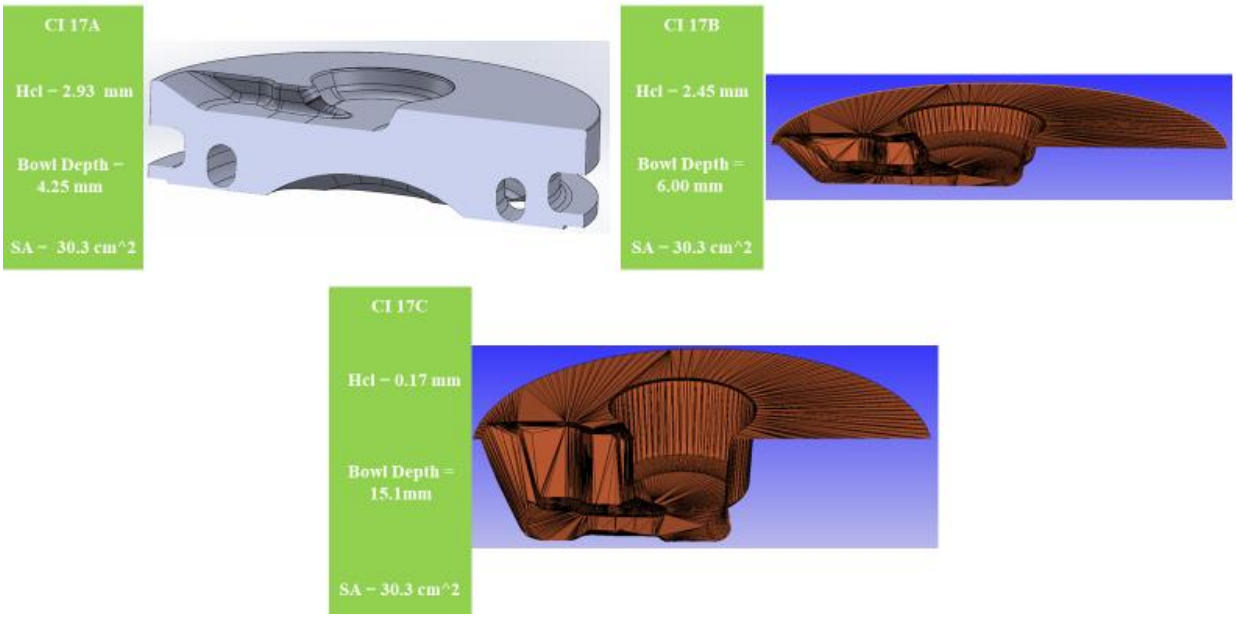

Figure 37: CR17 CI Piston investigation with clearance height in mm, bowl depth in mm, and surface area in cm^2 for CI 17A (top left), CI 17B (top right), CI 17C (bottom)

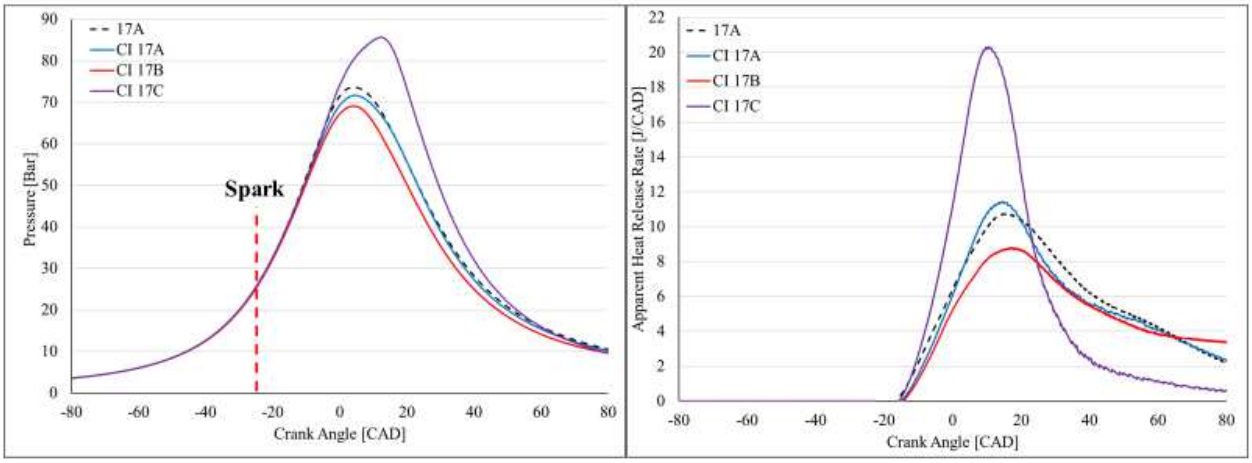

Figure 38: Pressure and AHRR curves for the three CR17 CI Pistons investigation with the original CR17 piston bowl design in black dotted line

Table 11: Indicated Efficiencies for the CR17 CI piston investigation compared to the CR17 Piston

	η [%]
17A	26.85 %
CI 17A	25.73 %
CI 17B	22.55 %
CI 17C	31.05 %

4.5.4 3rd Piston investigation

While running the experimental tests, backfires were noticed in the intake manifold, and after looking into the AHRRs, preignitions were also detected at -60 ATDC. These combustion issues were chalked up to heat spots, resulting in flame initiation prior to the spark or

experimental errors including uncertainty with the hydrogen flow rates resulting in fuel blend mixtures containing more hydrogen than expected; however, after further investigation, no promising source was found for the cause of these issues. More about the specifics of these issues can be found in Countie et al. The development of these issues created a need for a new piston design with a much lower CR of 14. Figure 39 shows the four initial piston designs for CR 14 modified from the CR17 piston and the lessons learned from the previous piston investigations. The 17A piston from Davinvi Engineering had a slight decrease to the squish area from 4.64 to 4.00 cm^2, and the clearance height increased from 0.23 to 1.29 to develop the piston design named “14A”. The piston called “14B” was created by expanding the bowl depth from 6.00 to 7.57 mm. The piston named “14C” was developed by having two different bowl depths so that the second bowl would fit in between the oil ports inside the piston. The first bowl depth was the same as CR17 and the second bowl of smaller diameter had a bowl depth of 10 mm from the top of the piston. The piston named “14D” was developed by increasing the squish area from 4.64 to 12.5 cm^2 and then drastically modify the bowl parameters so that a bowl depth from 6.00 to 10.00 mm would still fall within the oil ports. The Pressure and AHRR results from this investigation can be seen in Figure 40, where a black dotted line indicates 17A design, a purple line indicates 14A, 14B is indicated by a blue line, 14C is indicated by a red line, and 14D is indicated by an orange line. Figure 30 shows that the 14D had the best combustion, which is indicated by its higher peak pressure and AHRR values.

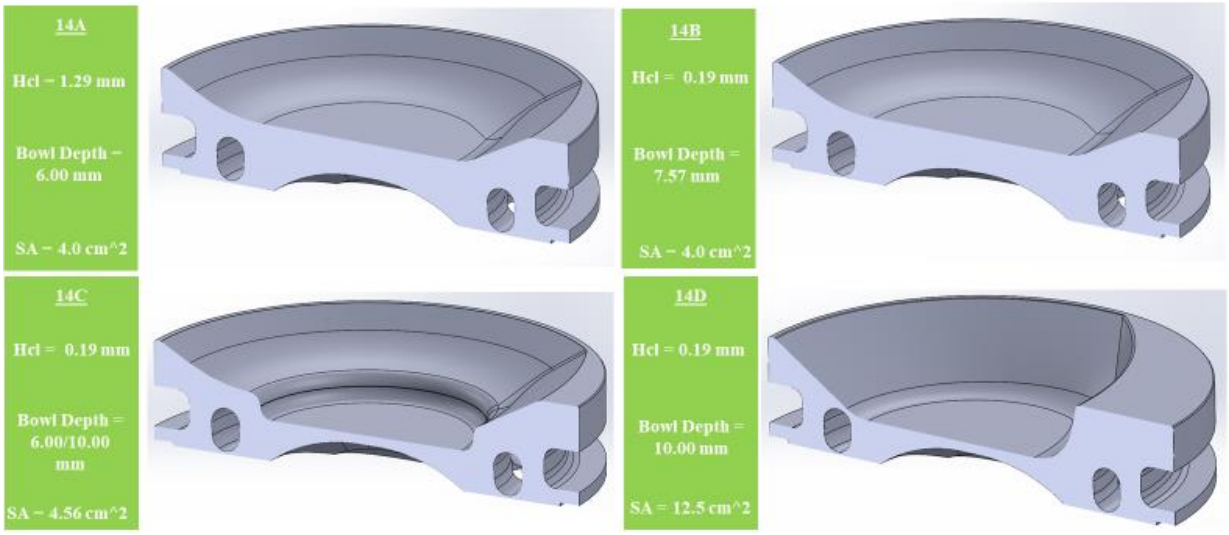

Figure 39: CR14 piston designs for backfire prevention with clearance height in mm, bowl depth in mm, and surface area in cm^2 for 14A (top left), 14B (top right), 14C (bottom left), and 14D (bottom right)

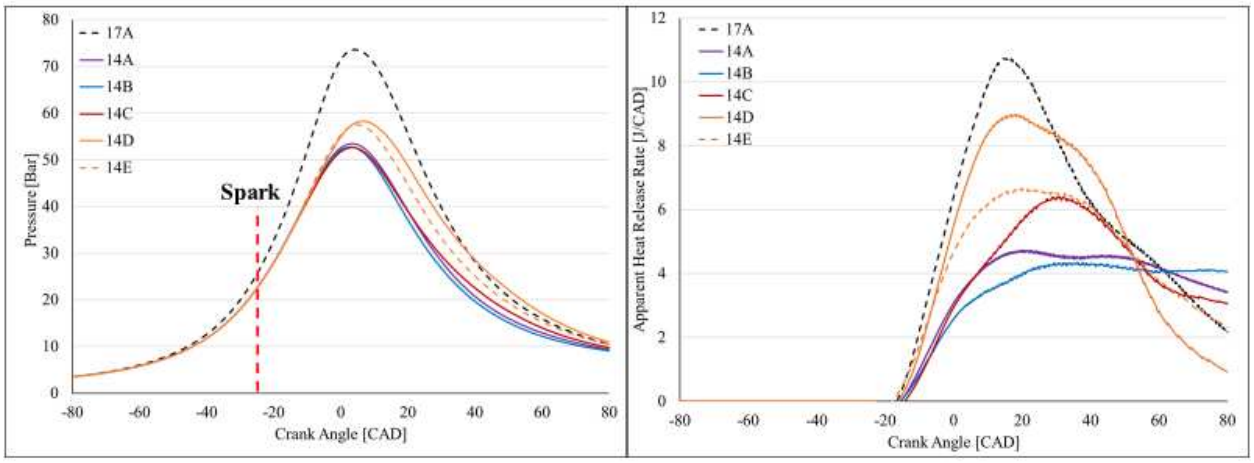

Figure 40: Pressure and AHRR curves for the CR14 Pistons designs and the original 17A design (black dotted line) with a spark at -23° ATDC

For the new CR 14 piston, the design was tested with a finite element analysis (FEA) software called “ANSYS Workbench” to see if the piston could withstand the stress and strain applied to it in an engine. Figure 41 and Table 12 show the terminology and constraints used to understand how the pistons were analyzed in the FEA software. Statical structural analysis was

assumed to depict how the piston behaves at a small instance where the most strain would be applied, which is at peak pressure. The cylinder pressure of 90 bars was placed at the top of the piston bowl while the piston was held in place by two frictionless supports to act as the piston rod and cylinder wall. Frictionless support is when "the body cannot move or rotate or deform in the normal direction, but free to move, or rotate in the tangential direction." The conditions set for the FEA modeling was for a worst-case scenario since none of the CR14 pistons achieved a peak pressure of 90 bar and to have consistency when comparing positions to each other.

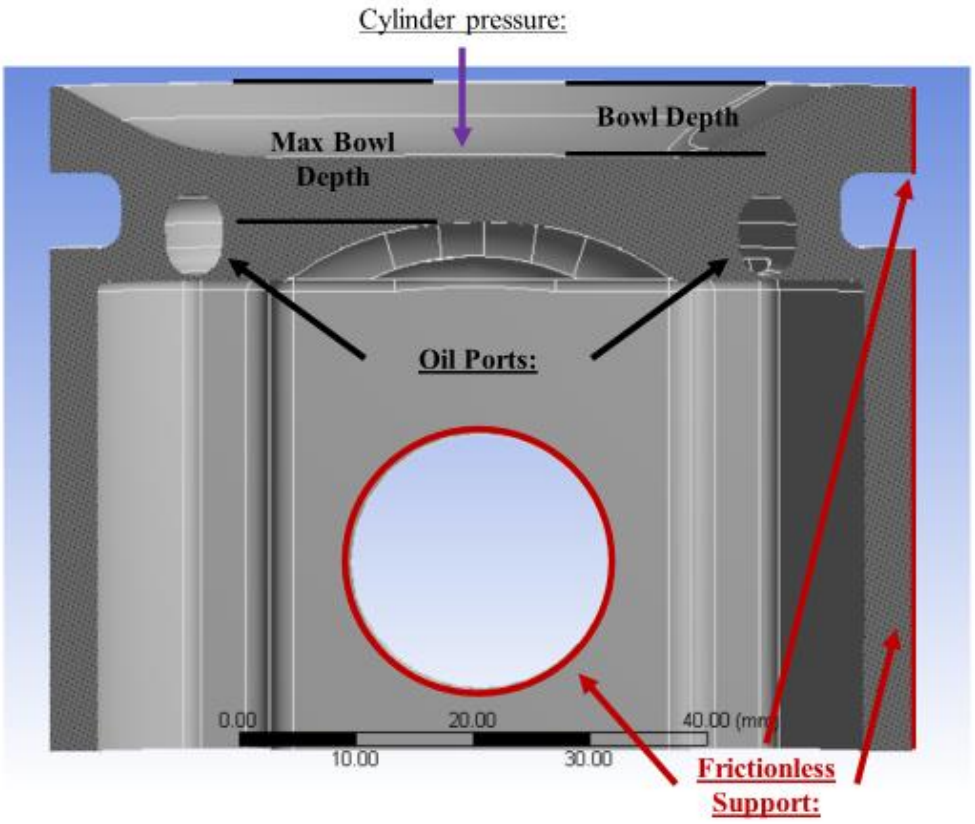

Figure 41: FEA study constraints diagram and piston terminology

A safety factor of 4 was used to determine whether the new piston design would withstand engine operations. This safety factor was determined because the original CR 17 piston achieved a safety factor of 4.6. Safety factor (SF) is calculated using equation (21), where

the maximum stress is from the FEA analysis, and the Ultimate Tensile strength can be found in Table 12 for aluminum alloy in ANSYS material database at room temperature. The material mechanical properties can be improved upon in the future to account for the real temperature that the piston experiences in the combustion chamber.

$$\text{SF} = \frac{\text{Ultimate Tensile Strength}}{\text{Maximum Stress}} \tag{21}$$

Table 12: FEA study values and Aluminum mechanical properties at room temperature

Bowl Depth	Varied
Cylinder Pressure [Bar]	90
Maximum Bowl Depth [mm]	9.34
Material	Aluminum
Young's Modulus [Mpa]	71,000
Tensile Yield Strength [Mpa]	280
Ultimate Tensile Strength [Mpa]	310

The 14D piston had a safety factor of 2.6 and was deemed unable to withstand operation in the Kohler engine. A high-stress concentration was noticed in the 14D piston at the center where a thin section separates the piston's bottom and the top of the piston rod and can be seen in Figure 42. However, this thin section is a simple fix by adding a dip on top of the high-stress

concentration area and reducing the squish area from 12.5 to 10.1 cm^2; another piston bowl is named “14E” was developed. Figure 43 shows the 14E piston, while Figure 42 shows the FEA analysis compared to the 14D piston. The new piston achieved a safety factor of 4, and the high-stress concentration was gone. However, the 14E piston was not as good as its predecessor but was still better than all the other piston designs, so it was selected to be manufactured. Table 13 shows the efficiencies for all the CR14 piston designs compared to 17A, with the 14D achieving the maximum efficiency.

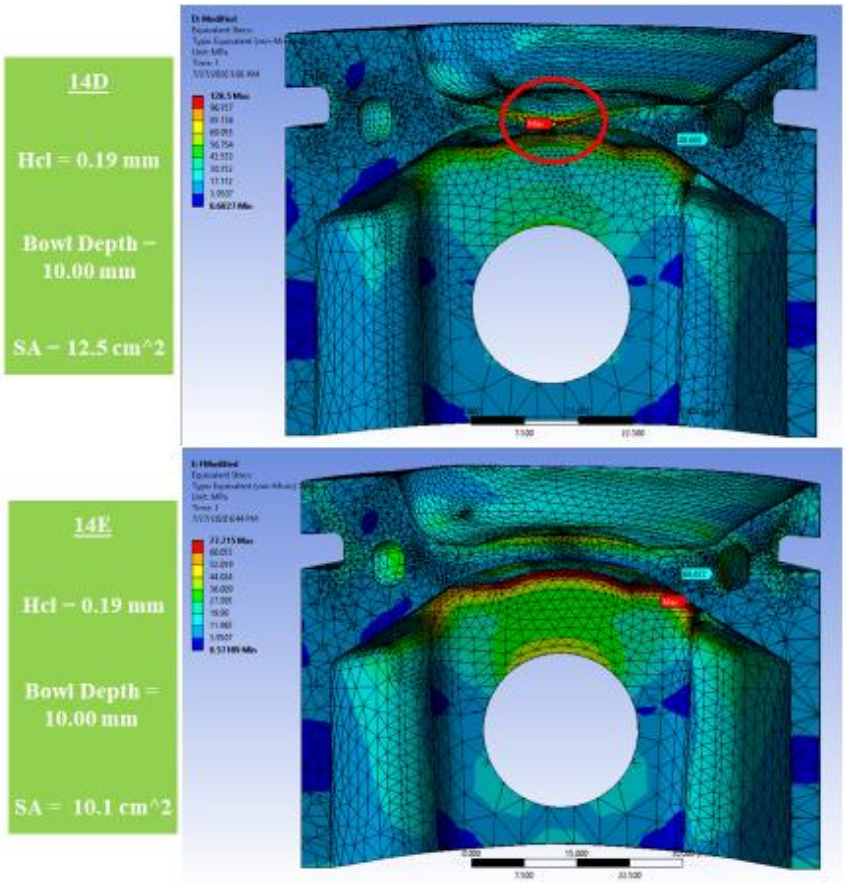

Figure 42: Equivalence stress results for 14D (top) and 14E (bottom) piston designs

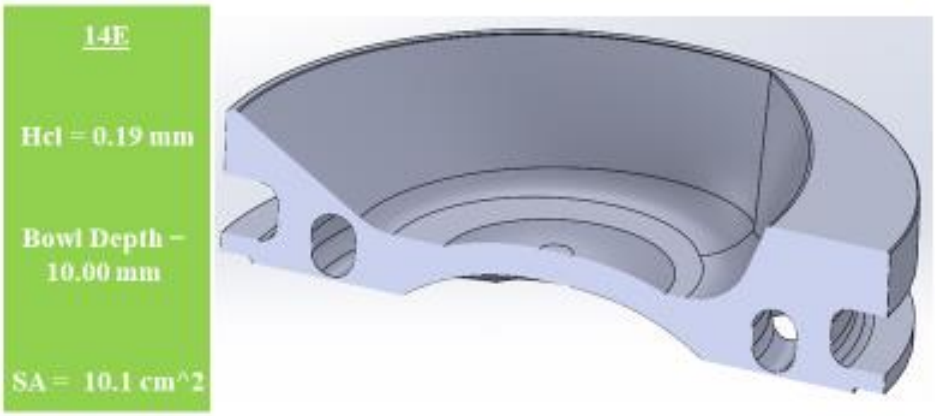

Figure 43: Best piston design for CR14 when it comes to performance and durability

Table 13: Indicated Efficiencies for all the CR14 piston designs compared to 17A piston

	η [%]
17A	26.85 %
14A	18.63 %
14B	17.13 %
14C	20.32 %
14D	27.70 %
14E	23.93 %

4.5.5 4th Piston investigation

The last piston investigation examines the location of the squish area relative to the spark plug. Figure 44 shows the Kohler engine's top view with the 14E pistons and indicates the form

in which the pistons will be identified. For instance, Piston CR14 clockwise 55° is the piston rotated 55° in the clockwise direction indicated by the picture in Figure 44. The pistons were either rotated clockwise (CW) or counterclockwise (CCW) and for either 55° or 27°. Again, it is hard to tell by the pressure curves in Figure 45 which rotated piston configuration is better. Still, the AHRR curve showed that all the piston rotation configurations outperformed the original CR14 piston with no rotation. This becomes even more clear when looking at Table 14 that shows improved efficiency from all the rotations, with clockwise 27° piston rotation having the greatest increase in efficiency. Figure 46 shows the flame propagation is faster in the clockwise 27° piston version then the original 14E piston, and it all has to do with the fact that the squish area is now closer to the spark plug. Meaning that the counterclockwise rotated pistons have a disadvantage to the clockwise rotated pistons because it rotates the squish area further from the spark plug instead of closer to the spark plug. However, the counterclockwise rotated pistons still receive an increase in efficiency because even though the squish area is further from the spark plug, it is no longer blocking the intake value port anymore, which causes better airflow better

combustion. For that same reason, clockwise 55° piston has worse combustion than clockwise 27° because the squish area blocks the intake valve more during intake.

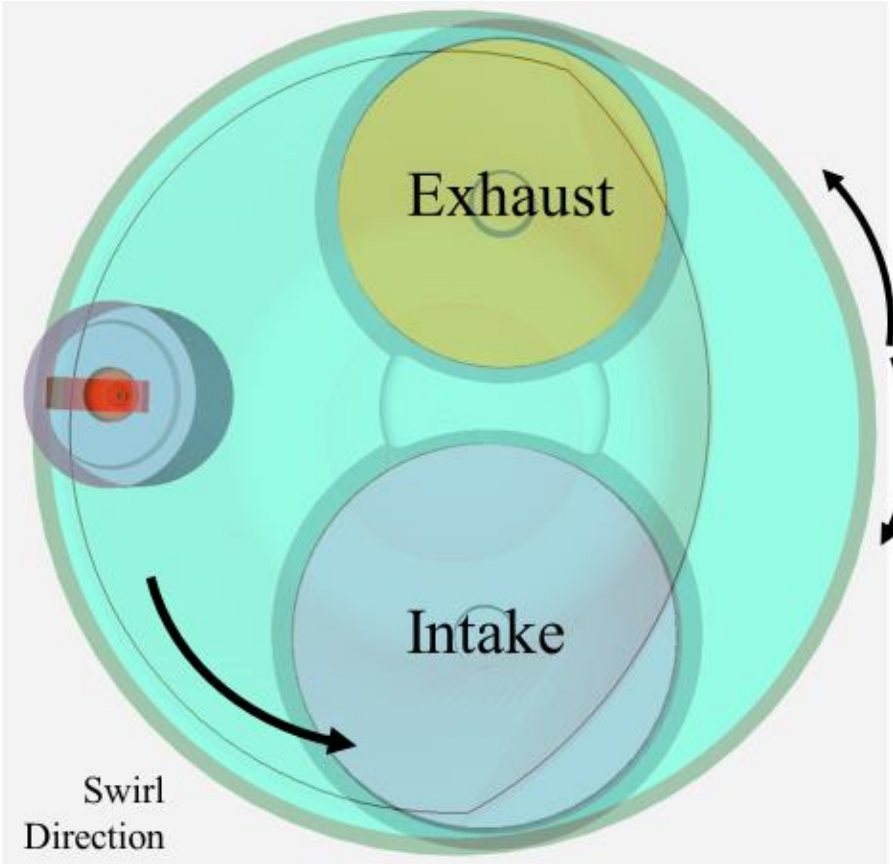

Figure 44: Top view of Kohler engine with the 14E piston with piston rotation investigation terminology labeled

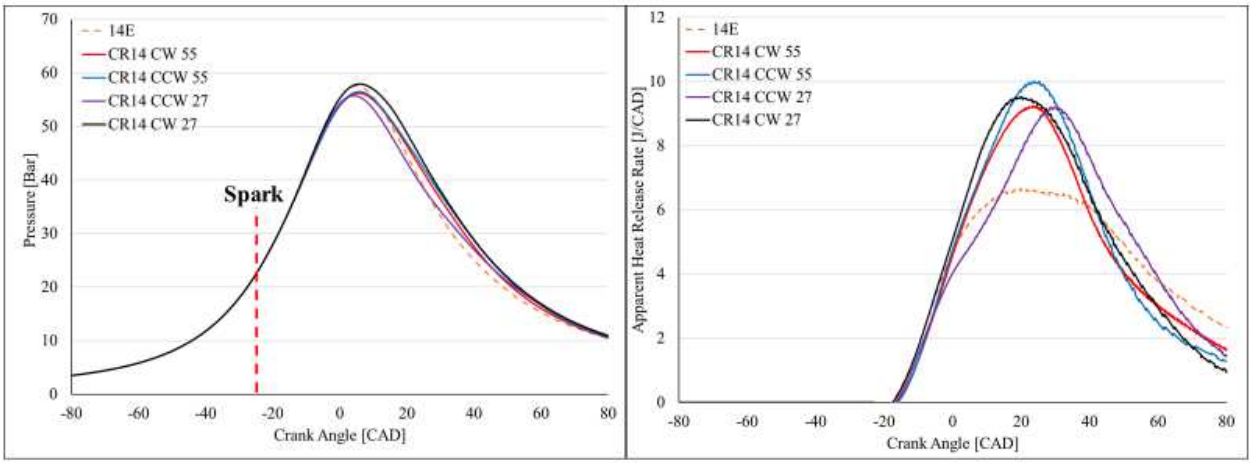

Figure 45: Pressure and AHRR curves for the CR14 piston rotation investigation

Table 14: Indicated efficiencies for CR14 piston rotation investigation compared to the 14E Piston with no rotation

Piston Name	η [%]
14E	23.93 %
CR14 CW 55°	25.82 %
CR14 CCW 55°	26.81 %
CR14 CW 27°	27.55 %
CR14 CCW 27°	25.57 %

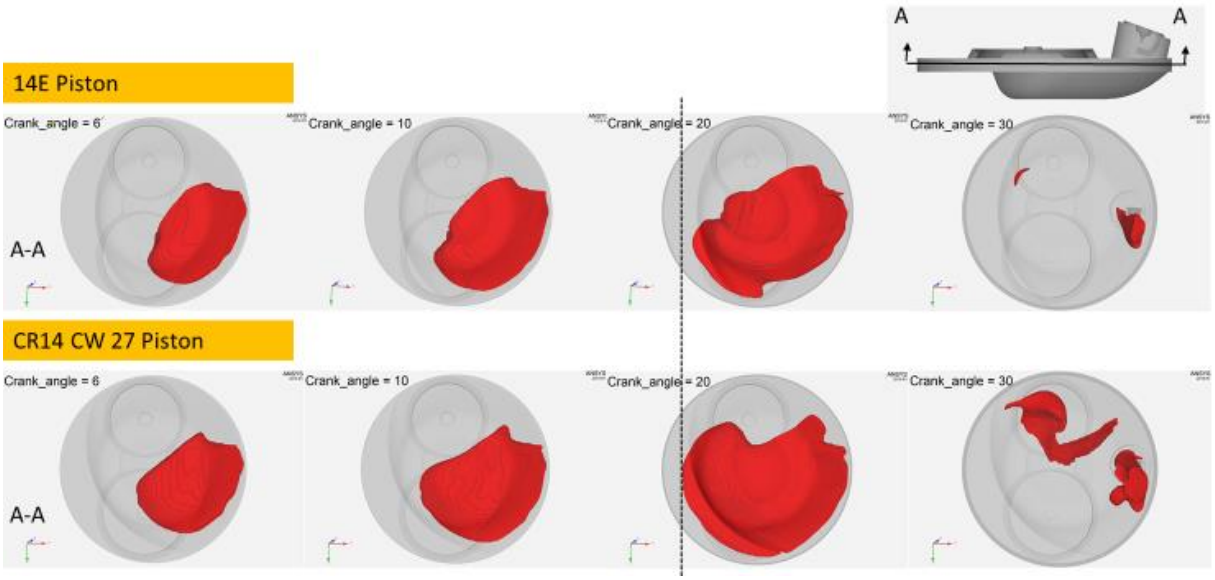

Figure 46: Temperature Iso-surface at 2000 K (red) to represent flame propagation for 14E piston (top) with no rotation and CW 27 rotation (bottom)

4.6 Manuscript Conclusion

Using experimental data and GT Power modeling for a CFR engine, it was possible to perform a single cycle simulation to predict engine performance with a non-traditional fuel like anode tail-gas. This was done by replicating five experimental test points with the CFD predicted pressure, AHRR, IMEP, CA10, and CA50. Through CFD and an adequate chemical mechanism, it was even possible to mimic engine knock in the two test points that observed engine knock. Both fuel blends (40° C and 90° C) were achieved model validation; however, the 90° C fuel blend did have the most error than the other four test point cases.

A similar CFD engine methodology was taken for the Kohler engine, and although the engine model is still not validated like the CFR engine. The CFD model was still helpful in performing three spark plug configurations and four-piston bowl investigations to achieve the maximum indicated efficiency. The three spark plug configurations showed that the spark plug flow could be improved, leading to better engine performance and lower COV. The four-piston

bowl investigations revealed that smaller clearance height, larger squish areas, and deeper bowl depths allow for better combustion and greater efficiencies. It was also possible to design a lower CR piston to reduce backfire and preignition possibilities while optimizing performance. The investigations demonstrated that the magnitude of the squish area and the squish area's location are important. By rotating the squish area closer to the spark plug, the indicated efficiency increased from 18.55 % to 21.37 %; however, this is a push and pull battle; if the piston is rotated too much, efficiency will begin to decrease.

With the help of the work carried out in the CFR and Kohler engine, there is now a well-built foundation for future work to be carried out in the pursuit of achieving an anode tail-gas gasified engine that operates at 35 % efficiency and produces 14 kW.

4.7 Future Work

This project's future work should focus on finding better spark modeling methods to improve the CFR engine test data's predictability. It should also focus on investigating cycle to cycle variation with the CFR engine to validate further the CFD model and its ability to predict knock. All that work could then be applied to the Kohler engine once reliable experimental data is available to validate the CFD model. With the model validated, the current experiments should then be re-investigated, and even more, cases should be looked into until the 35% efficiency goal is met.

Chapter 5: UAV Engine Model (Manuscript 2)

5.1 Background

The US military spends millions of dollars a year on fuels to power their vehicles and buildings. [52] The military's three primary fuels are jet fuel (propellant), gasoline, and diesel fuel. During times of deployment, the military must spend additional funds to transport each of these fuels. Additional funds are required to transport highly volatile fuels such as gasoline due to the safety considerations related to the high ignition tendency at standard conditions. The other fuels (including jet and diesel fuel) are less volatile, safer, and cheaper to transport. Transportation of gasoline is still vital for the military because it supplies power to essential equipment such as generators and Unmanned Aerial Vehicles (UAVs). Ideally, by running these pieces of equipment on a less volatile fuel, the military would avoid the increased cost and safety risks of transporting gasoline.

The US military recognizes the Single-Fuel Policy benefits, as several studies have been conducted to analyze this policy's feasibility. The Single-Fuel Policy states that "the military can only use a single fuel when deployed." [53] The biggest positive of the military only using a single fuel is transportation. "During Operation Desert Shield/Desert Storm, the US military used five different fuels (Jet A-1, JP-4, JP-5, diesel, and automotive gasoline)." This meant that at least five different tankers were needed to transport the five different fuels since each fuel has unique characteristics requiring them to be segregated. [53] If five tankers were not available, then the same tanker would be used to transport two fuels. This meant that at the end of transporting one fuel, the tanker had to be cleaned before transporting a different fuel to ensure that the fuels were not mixed in any way. This process was very inefficient, but with the Single-

Fuel Policy, such problems would not exist. There would also be fewer regulations on how fuels must be stored. The other benefit of having a single fuel is the ability to be resourceful with that fuel. For example, if supplies and the ability to receive supplies were limited, a vehicle's fuel could be used to power a generator or vice versa.

The Single-Fuel Policy is not a new concept. The Single-Fuel Policy was first introduced and applied to the military in 1934 when a former Army Air Corps pilot tried to get military aircrafts to switch to a 100-octane fuel. [53] In 1986, there was another big push for a single fuel because of two particular problems with Air Force aircraft fuel fires and army vehicle fuel freezing in cold weather. [53] In 1990, the Single-Fuel Policy was implemented with JP-8 in Fort Bliss and Jet A-1 in Desert Storm. Some problems were detected with equipment components like pumps, injectors, and filters not working correctly or at full capacity since no research was carried before implanting the policy. [54] Even today, there is still little to no universal Single-Fuel Policy in the military. Further research must be conducted to modify all military equipment to run optimally with a single fuel. [54]

Heavy hydrocarbon fuels, such as JP-8, are likely candidates for the Single-Fuel Policy because of its increase in safety and low freezing point. Both the Air Force and the Army saw JP-8 as a possible solution to their problems in 1986. However, there was no evidence to prove that it would work just as well as JP-4 in aircrafts or as well as diesel fuel in tanks. For that reason, many studies are currently exploring the implementation of heavy hydrocarbon fuels like JP-8 into diesel vehicles because they have similar physical properties. [55] JP-8 is very similar to diesel fuel and can be easily replaceable with slight modifications to the engine/hardware. However, the military still uses gasoline to power very important equipment like generators and UAVs. JP-8 is very different from gasoline and would not be as simple to implement into vital

gasoline-powered equipment. These are the reasons why there has not been a universal Single-Fuel Policy yet in the military.

Meaning that the biggest obstacle the Single-Fuel policy will need to overcome is the use of JP-8 in gasoline-powered vehicles. However, since JP-8 is less volatile and has shorter ignition delays, it is more prone to cause engine knock during combustion. This will be one of the biggest challenges in converting a traditional gasoline-powered UAV engine to operate with JP-8. UAV engines are traditionally small two-stroke SI engines powered by a premixed fuel because of the high specific power possible for their size, which allows for lightweight and the ability to drive a propeller at high speeds. However, challenges exist as two-stroke engines typically operate at high RPMs and require proper fuel mixing to achieve the best possible performance. This means that the direct injection approach must be fast and provide proper atomization for the less volatile JP-8 to evaporate and mix with the air ahead of combustion.

Previous research conducted by the Air Force Research Laboratory found that JP-8 could be used in UAV engines at High speeds; however, at low speeds or start-up/idling speeds, JP-8 was less reliable since it required a lot of knock mitigation.[12] Now stratified combustion is being used to reduce engine knock probability in SI engines by promoting conventional combustion propagation from the point of ignition (spark plug) down to the piston. Stratified combustion is achievable by modifying the fuel injector parameters to change the injection rate shape and obtain a stratified mixture like in Figure 5. Due to the unique characteristics of JP-8 fuel, extensive research must be conducted to find the best parameters for proper ignition in a gasoline two-stroke UAV engine. This can be accomplished by using simulation approaches to identify the optimal

fuel injector design to get the desirable stratified combustion that promotes flame propagation while avoiding knock.

5.2 Methods

To the best of our knowledge, this is the first study attempting to develop a 3-D engine simulation for a small two-stroke engine like those used in UAVs. On top of this being the first attempt at CFD engine modeling, there is currently very little experimental on UAV engine. That is why this project's success depends on the engine's 3D model and the ability to obtain experimental engine data. The engine platform selected for this research was a 3w-28i engine used in class 2 UAVs. [11] The engine's specifications can be found in Figure 47; it is a spark-ignited single-cylinder two-stroke engine with two scavenging ports and a boost port in crossflow. It was selected because of the available experimental data from Oregon State University and the Air Force Research Laboratory (AFRL). [12], [56]

Descriptions	Measurements
Cylinder Capacity (cc)	28.5
Power (hp)	2.75
Bore Diameter (mm)	36
Stroke (mm)	28
Maximum Speed (rpm)	8500
Compression Ratio	10:1

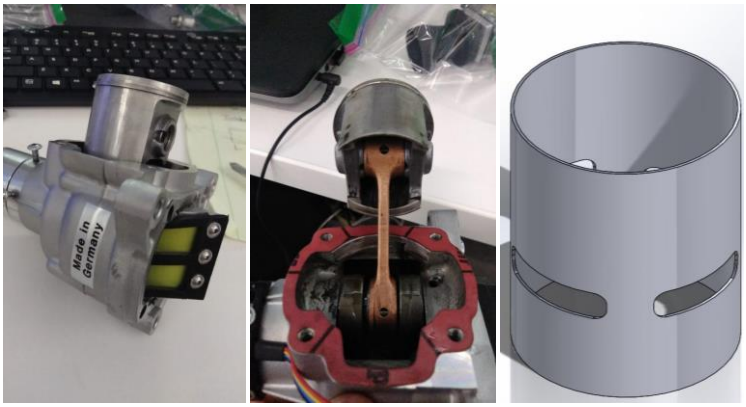

Figure 47: 3w-28i Engine Specs [57], disassembled 3w-28i engine, Piston and connecting rod exposed, and SOLIDWORKS model of the cylinder with three intake ports and an exhaust port

A 3w-28i engine was procured, disassembled, and dimensioned to create a 3D model in SolidWorks and Figure 47 shows the results of this. [57] The shell was then imported into CONVERGE, and the geometry was cleaned up, as discussed in Chapter 3: General CFD Methods

to prepare the model for engine simulations. The crankcase and muffler were eliminated from the model to minimize computational time, thereby maintaining the model's appropriate structural and thermodynamic characteristics. The emphasis was placed on modeling the intake and exhaust conditions to maximize the accuracy of the model. Figure 48 shows the cross-section views of the 3D model created for the 3w-28i engine in CONVERGE CFD.

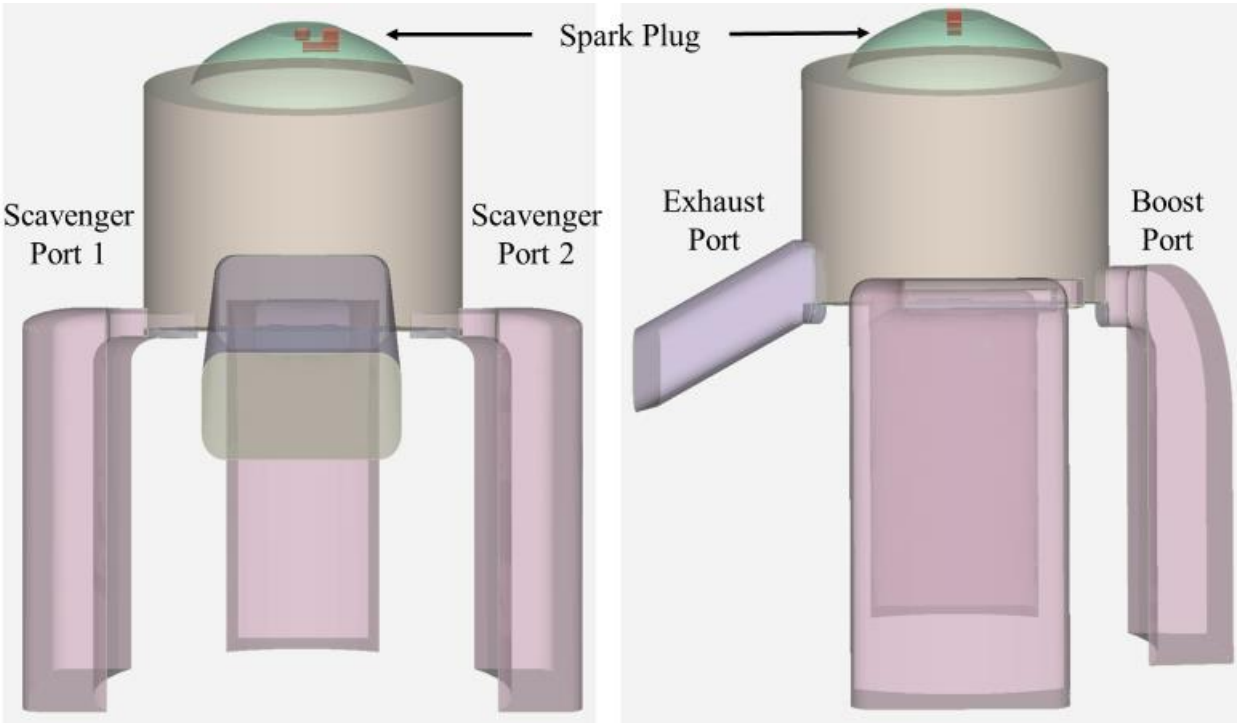

Figure 48: 3w-28i Engine model in CONVERGE with intakes, exhaust, and spark plug highlighted

The fluid dynamic conditions experienced during the intake/exhaust stroke are crucial in a two-stroke engine. A base mesh ranging from 1.8 to 2.1 mm was used for all simulations with boundary embedding placed two layers thick on all boundaries to reduce cell sizes to 0.45 or 0.525 mm depending on the base mesh size. Box embedding (like spherical embedding, just different shapes) was used at both intake and exhaust ports to refine the base mesh size as small as 0.225 mm. In addition, similar AMR conditions were used to resolve the flow characteristics.

This project's hypothesis states that if the traditional premixed gasoline fuel used in a UAV engine were replaced with a premixed stoichiometric JP-8 mixture, knock would be observed. Meanwhile, if the premixed gasoline fuel were replaced with properly direct-injected JP-8, then the stratified mixture would reduce the knock intensity, or the engine knock all together. To prove this hypothesis, three test cases in CONVERGE were setup. The initial simulations were carried out using iso-octane as a surrogate for Gasoline to simplify the model and reduce computational time.[30] A primary reference fuel (PRF) mechanism from Lui et al. consisting of 49 species and 152 reactions was used. [58] A second simulation was carried out under the same conditions used for premixed iso-octane (100 ON), however, now using n-dodecane as a surrogate for JP-8 to check the first part of the hypothesis. The mechanism used for n-dodecane has 54 species and 269 reactions developed by Yao et al. [59] The final simulation was of the fuel being supplied employing multiple direct injects to replicate equivalence ratio stratification in the cylinder that would lead to stratified combustion and hopefully reduce knock intensity. However, before these simulations were carried out, the JP-8 surrogate's validity was investigated using CONVERGE's chemical kinetic solver to compare the ignition delay and flame speeds against other verified JP-8 surrogates. Reduced mechanisms were used on top of the surrogates to further reduce computational time. The species and reactions comparison for the reduced mechanism to other PRF and JP-8 mechanisms can be found in Table *15*.

Table 15: Reduced mechanism comparison [58]–[61]

Mechanism	Species	Reactions
Reduced JP-8	54	269
JP-8	231	5741
Reduced PRF	48	152
PRF	108	435

The surrogates selected for a JP-8 comparison were 20 ON with PRF, which came from Ausserer et al., JP-8 surrogate C from Bravo et al., JP-8 Princeton from Edwards et al., dodecane, and dodecane with the reduced mechanism.[12], [34], [62] Figure 49 depicts the similarity in flame speed for all the JP-8 surrogates at experimental spark conditions of about 20.5 bar and 800 K with a stoichiometric mixture. However, from Figure 49, it is also notable that all the surrogates vary somewhat when it comes to ignitability, which ranges from 0.4 to 1.65 ms at 800 K. It is reasonable to use dodecane as a JP-8 surrogate since it has similar results as other JP-8 surrogates; however, it should be noted that since this surrogate has the lowest ignition delay at spark timing conditions the results might be a worst-case scenario.

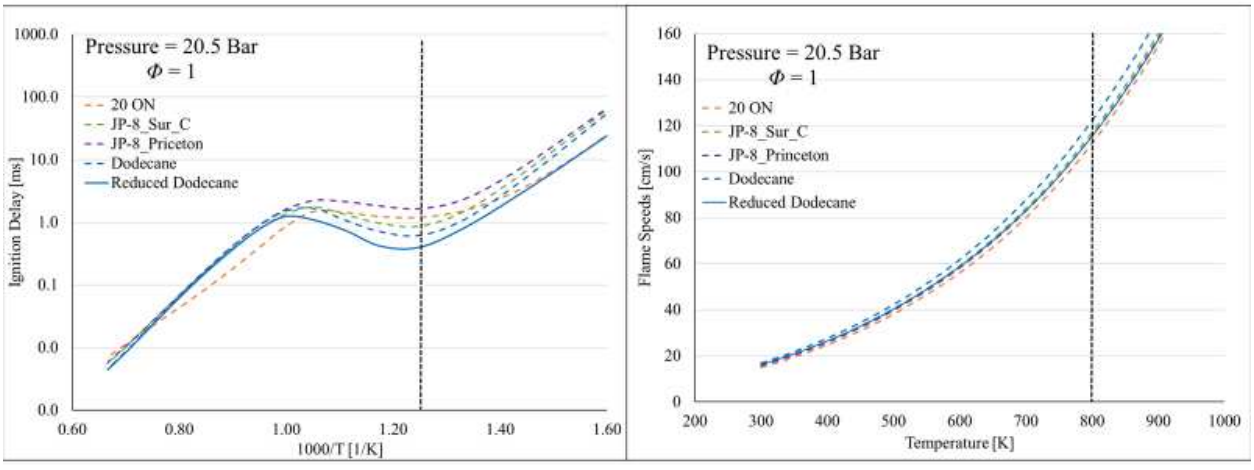

Figure 49: Ignition Delay and Flame speed curves of various JP-8 surrogates at 20.5 bars with a stoichiometric mixture

On top of checking the JP-8 surrogate's validity, the reduced mechanisms' validity was also examined with ignition delay and flame speed curves. Figure 50 shows excellent agreement in ignition delay and flame speed comparison of the reduced mechanism to another base mechanism with more species and reactions. Another take away from Figure 50 is that dodecane has greater ignitability and faster flame speeds than 100 ON fuel, causing knock tendencies in the engine.

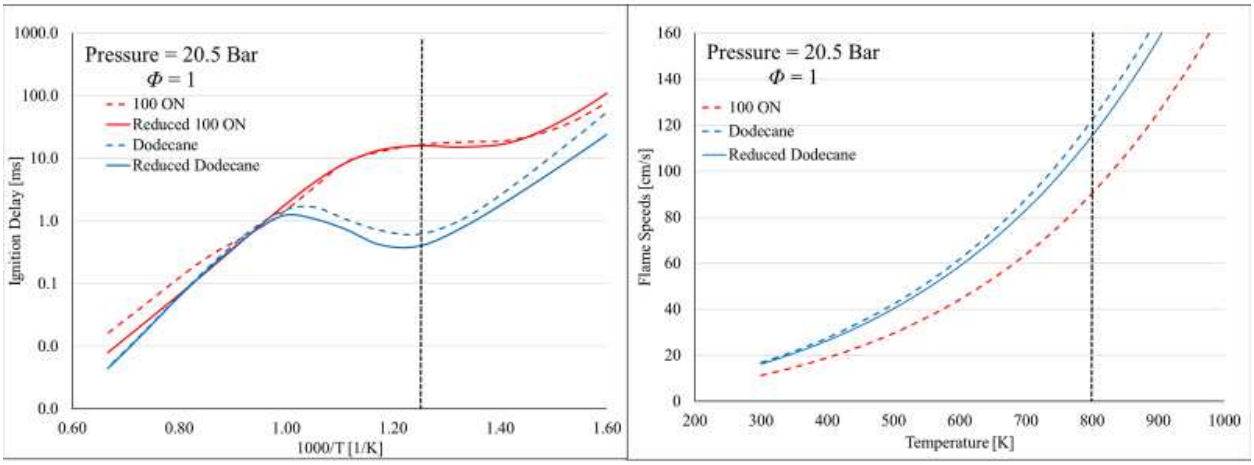

Figure 50: Ignition Delay and Flame speed comparison for 100 ON (red lines) and dodecane at 20.5 bars with the stoichiometric mixture using both a base (dashed lines) and reduced mechanism (solid lines)

The simulations' start was set to -262° ATDC when all the ports are closed and right before the piston began to open the exhaust port. A spark source of 0.2 mm at -13° ATDC was used for all simulations. Since the intake ports in a two-stroke engine receive a boost pressure from the crankcase, it is tough to predict the intake data. With no experimental intake or exhaust data, the pressures were held at a constant 2 bar and 1.5 bar for intake and exhaust, respectively. The intake pressure value was assumed from the in-cylinder pressure at -180° ATDC, and the exhaust value came from the fact that exhaust pressures are slightly above atmospheric pressure. However, since

these are very big assumptions, future work should develop a GT Power model to present better intake and exhaust pressure assumptions. The maximum CFL limits used in all the simulations were 2, 5, and 50 for convection, diffusion, and Mach, respectively. A Mach CFL limit of two was used after spark timing to reduce the time step and better capture the rapid increases during knock. The maximum diffusion CFL limit for these simulations was a little high compared to other simulations, which is acceptable since most of the mixtures were premixed with minimal species. However, this may be a cause of concern during the direct injection simulations where fuel and air mixture occurs throughout the simulations. It may also be a concern if a different JP-8 surrogate will be used later, at which point the CFL limit should be reduced to two or lower.

Similar thermodynamic conditions used for the premixed iso-octane and n-dodecane cases were used for the spray studies of n-dodecane. Four parameters (injection timing, number of injections, amount of mass per injection, and droplet size) were investigated on their effect of formulating stratified combustion that could reduce knock intensity. The injection timing was constrained by piezoelectric not actuating at >80% of their resonant frequency of >1250 Hz, making the average piezo timing ~1 ms, which at standard UAV operating condition of 6500 RPM, is about 50°CA. [11] The number of injections can range from four to a total of eight.[11] The amount of fuel mass entering the combustion chamber per injection can also be tuned to create stratified combustion while maintaining the mass to achieve a stoichiometric mixture. [11] Droplet size plays a significant role in assisting evaporation, and so typical injector droplet diameters of 10 to 20 μm were varied to study its influence on combustion performance. [11] The spray configuration was duplicated from the design of a Ski-Doo snowmobile two-stroke engine. [63] The different combinations of the four parameters were studied to find an optimized strategy that mitigates knock to negligible or not existent points. To help find the optimal combinations of

injector parameters, an investigation was carried to understand how the equivalence ratio affects both ignition delay and flames speeds. This investigation is also carried out to find the ideal stratification profile like the one seen in Figure 5; however, with set ranges of equivalence ratios to achieve the best possible flame propagation while avoiding knock. Figure 41 shows that as the equivalence ratio increases, the ignition delay is shorter for both 100 ON and n-dodecane. It is also clear from figure Figure 51 that the sweet spot for fast flame speeds is near the stoichiometric mixture. Both these points support the assumption depicted in Figure 5 that the mixture near the spark plug should be stoichiometric/rich, and the mixture near the piston should be lean to promote flame propagation and reduce knock tendency characteristics. With the help from Figure 51, another image like Figure 5 was constructed with ideal equivalence ratio values for mixtures near the spark plug and piston, which can be seen in Figure 52.

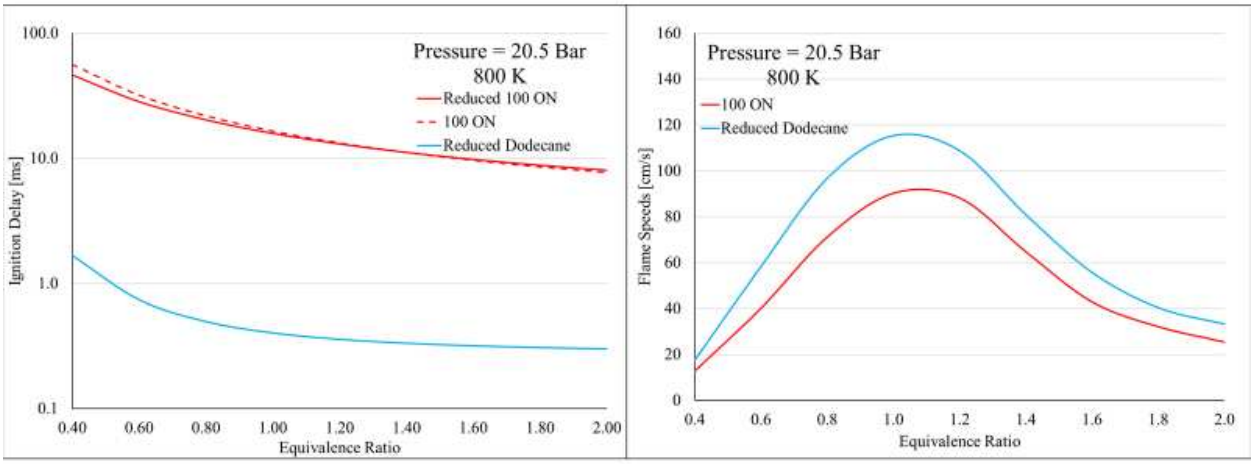

Figure 51: Ignition delay and flame speed vs. equivalence ratio for both 100 ON fuel (red) and n-dodecane (blue) at 20.5 bar and 800 K

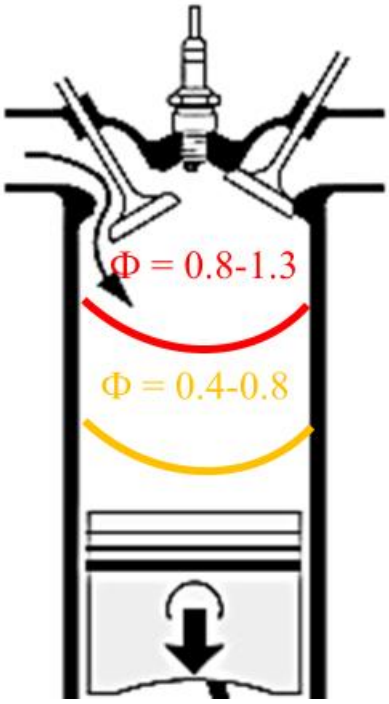

Figure 52: Stratified mixture with indicated ideal equivalence ratio ranges to promote flame propagation and avoid engine knock

5.3 Results and Discussion

For Phase I of this project, proof of concept study, demonstration, and initial simulations were carried out based on experience and knowledge of expected intake/exhaust boundary conditions in two-stroke internal combustion engines.

A study was performed on the intake/exhaust stroke to validate that the model's geometry was correct, and the fluid dynamics of the intake/exhaust stroke were representative of that of a two-stroke engine. From Figure 53, it is clear to see one of the two characteristics commonly seen in two-stroke engines: backflow and unburned fuel mass transferred through the exhaust.[5] The backflow is due to the initial pressure difference between the cylinder and intake ports. Intake flow into the cylinder can begin only when the in-cylinder pressure equalizes to the intake pressure. A

large amount of fuel mass is wasted through the exhaust port, which is typical for two-stroke engines since the exhaust port is directly facing the intake port.

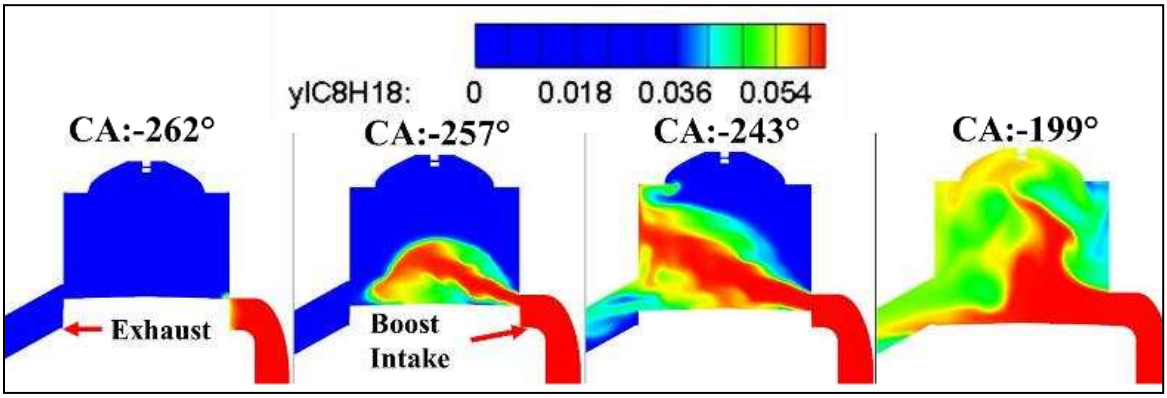

Figure 53: Cross-sectional view of the fuel flow in the cylinder, intake, and exhaust ports during the intake/exhaust stroke with an emphasis on exhaust fuel waste

5.3.1 Iso-Octane Combustion

Unfortunately, the model was never validated with experimental data without intake and exhaust pressure data, as shown in Figure 54. As was noted in the methods section, the intake and exhaust pressure data were assumed to be 2 bar and 1.5 bar. However, since this project focused mainly on proof of concept, mimicking similar trends like peak pressure was deemed acceptable for the first phase of the project with the intent to validate the model later when more extensive experimental data was available. Besides, since all the simulation case setup values were identical with only the fuel being varied, any trends are likely to occur in experimental data.

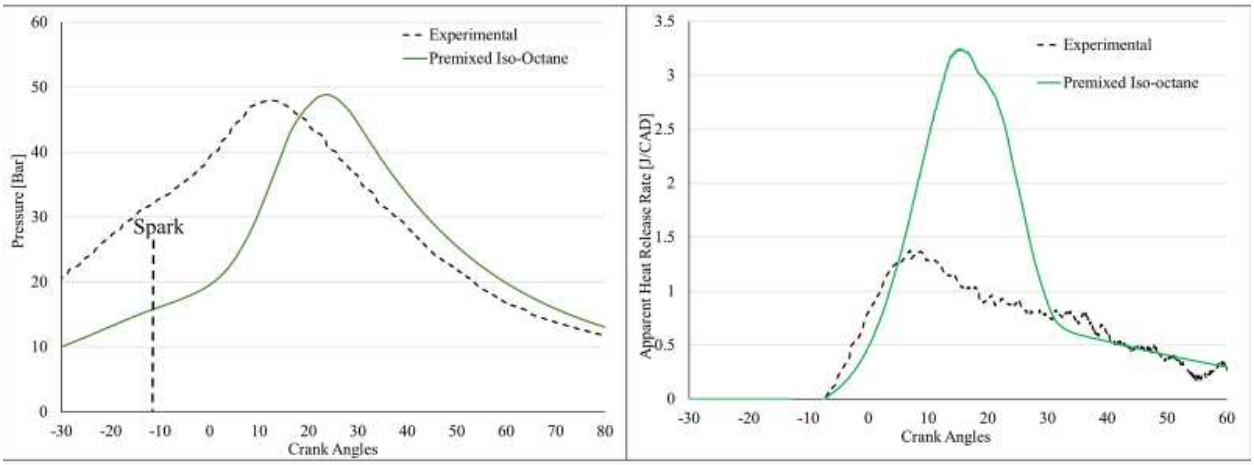

Figure 54: Pressure trace (left) and AHRR (right) for Premixed Iso-octane (green) and experimental data (black) with spark timing indicated

The heat release, which is small in magnitude, is visible in Figure 55 for a premixed stoichiometric Iso-octane mixture at typical operating speeds of 6500 RPM and a -13 ATDC spark timing. This indicates that the engine's thermodynamic conditions are such that the combustion is on the verge of becoming unsteady. A series of flame snapshots highlighting the iso-octane flame propagation is visible in Figure 56. Combustion propagates in the dome area near the electrode and spreads towards the squish area of the engine. Simulations with iso-octane do not show any signs of heavy end gas auto-ignition. Flame kernel growth is robust, and no signs of flame kernel quenching were observed during the initial flame kernel growth for premixed iso-octane.

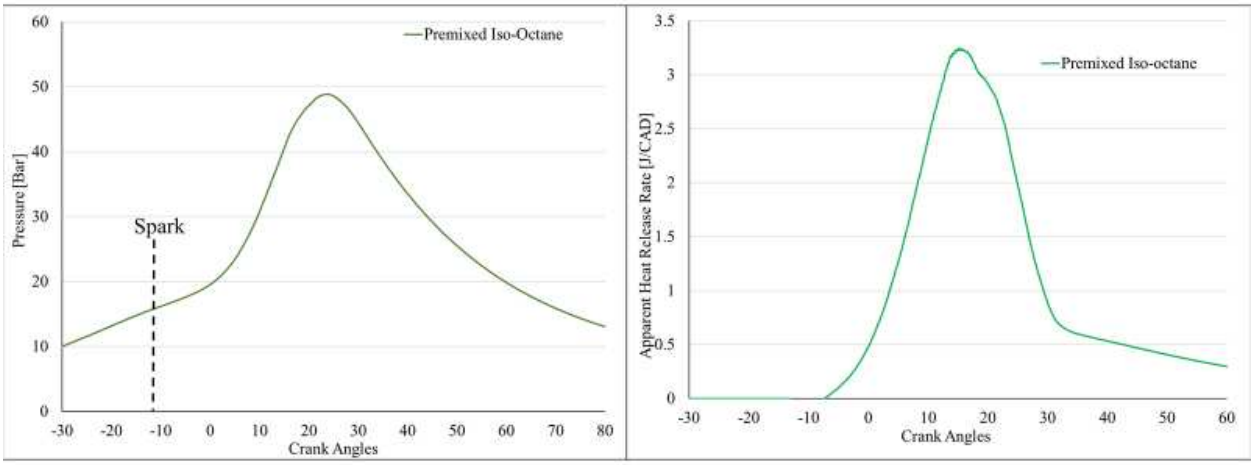

Figure 55: Premixed Iso-octane pressure trace with spark timing indicated (left) and AHRR (right)

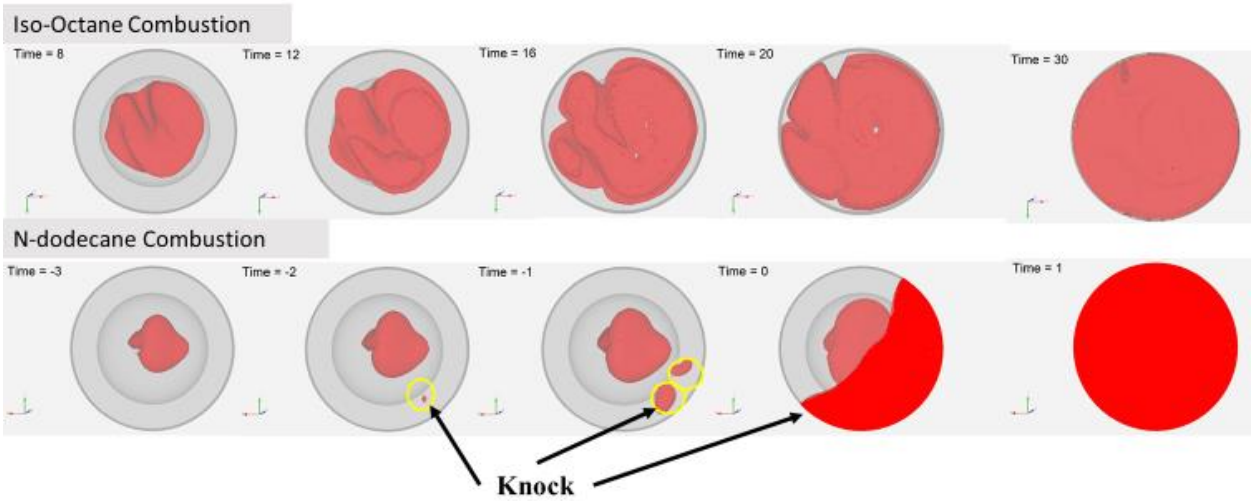

Figure 56: Cross-sectional image of an Iso-surface at 2000 K for both premixed stoichiometric Iso-octane and n-dodecane with knock indicated

5.3.2 n-Dodecane Combustion

In the case of premixed n-dodecane, a heavy end gas auto-ignition/knock was observed in the premixed n-dodecane case. Figure 57 shows the clear indication of severe end gas auto-ignition/knock with a sharp increase in the heat release and pressure rate indicated by the purple line. The auto-ignition takes place near the exhaust side as the exhaust port is hotter than the

intake side. This early onset of auto-ignition results in a heavy knocking series occurring in the squish area domain and causes a rapid rise in heat release, which further triggers engine knock for the premixed n-dodecane case.

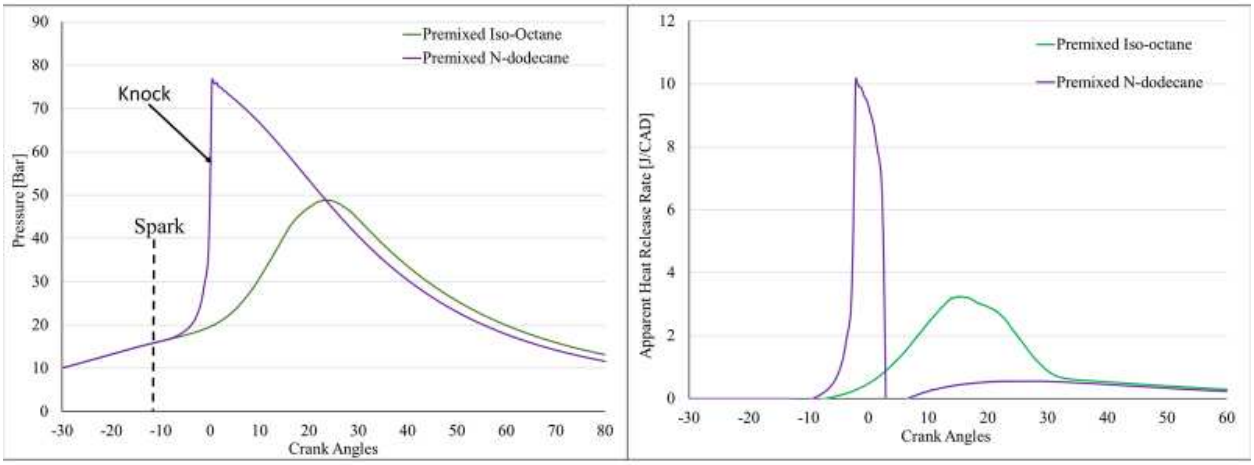

Figure 57: Premixed Iso-octane and premixed n-dodecane pressure trace with knock indicated (left), and heat release rate (right)

The iso-octane simulations were configured to operate at the borderline knock conditions. That is why when the fuel was replaced with n-dodecane, a severe engine knock occurred because n-dodecane has a shorter ignition delay compared to iso-octane. It is clear from the simulation data that there is a need to inject n-dodecane into the 3w-28i engine in a calculated manner, which can produce adequate power and reduce engine knock. One way to do this is to add the fuel with multiple injections such that the fuel remains rich near the dome area/spark plug and is leaner near the squish area where the onset of knock is likely to occur.

5.3.3 Spray Modeling Combustion

An investigation was executed using n-dodecane as the fuel to understand how the number of injections and droplet size influences the air/fuel mixture stratification ahead of combustion in a two-stroke engine. Four to eight injections (i.e., at 4 - 8 kHz) were performed in

a two-stroke model case, all equally distributed over 50 CA starting at -90° ATDC, which amounts to ~1.3 ms at 6500 RPMs. Both Injections had 10 µm diameter droplets, and the total mass was divided equally for each injection while maintaining an overall stoichiometric equivalence ratio. Figure 58 demonstrates this fuel injection strategy composed of a series of eight fuel-injection events at 8 kHz in which the fuel mass per injection is held constant. Alternatively, any rate shaping profile can be simulated in CONVERGE, providing one the ability to control the number of injections, the fuel per injection, and the time between injections. From these simulations, it is noticeable that less fuel vaporization occurs with fewer injections executed, with most of the fuel mass locating on the piston surface due to spray-piston impingement. This is seen in Figure 59, where the equivalence ratio histogram for eight injections is distributed between five different equivalence ratio bins. In comparison, at four injections, it is only distributed between three equivalence ratio bins. This is more clearly seen in the inset CFD images taken immediately after the last injection, noting that both scenarios' first and last injection occurs at the same CAD. After the last injection of the 4 kHz injection strategy, the equivalence ratio contour indicates extremely fuel-rich regions near the piston and hardly any fuel-lean in the cylinder volume.

In contrast, in the 8 kHz case, much more air/fuel mixing has occurred. This is likely due to poor atomization resulting in more wall impingement with the more extended injection events experienced in the 4 kHz injection case than the 8 kHz injection strategy. To operate a spark-ignited engine with jet fuel, it will be necessary to evaporate the low vapor pressure fuel rapidly, and it will also be critical to stratify the charge to prevent the auto-ignition of the end gas ahead of the flame. Although these tests have yet to include combustion, one can see the advantages of

operating at high injection frequencies by examining the increased evaporation of the n-dodecane and the level of fuel stratification when operating the injector at 8 kHz compared to the 4 kHz.

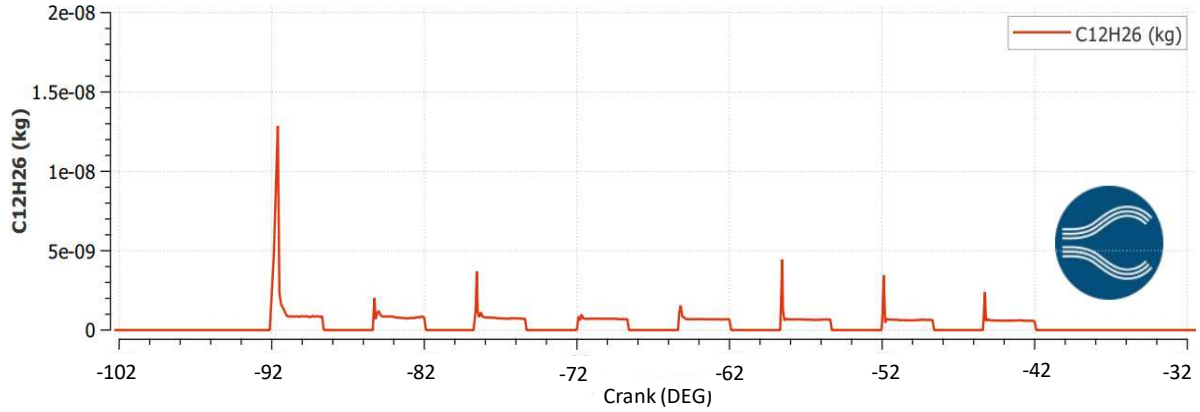

Figure 58: Injection train of the 8 kHz injection strategy of n-dodecanes, with results in Figure 59

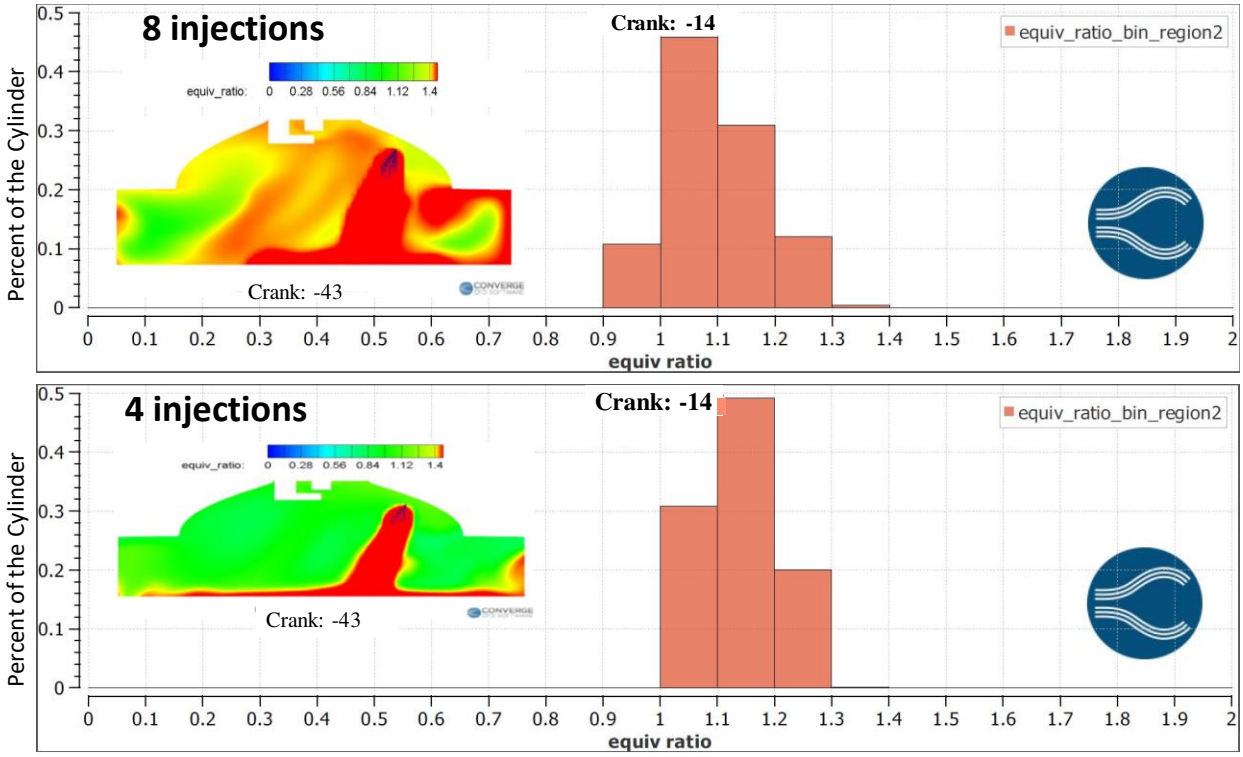

Figure 59: Equivalence ratio histogram for the cylinder at -14° ATDC corresponding to the start of the spark with 8 kHz injections of n-dodecane (top) and 4 kHz of n-dodecane (bottom). Also included are images depicting slices centered in the cylinder during the two-stroke engine simulation showing the equivalence ratio's spatial distribution at the last injection.

A similar investigation was performed to understand the sensitivity of droplet size on the fuel-air mixing of n-dodecane in a direct-injected two-stroke engine. In Figure 60, the instantaneous equivalence ratio distribution from the 8 kHz injections with a mean droplet diameter of 10 µm is compared to the equivalence ratio from 8 kHz injections with a mean droplet diameter of 20 µm. As seen in both the histogram and the inset images, the 20 µm droplet simulation predicts a greater distribution in equivalence ratios than the 10 µm droplet case. One would imagine that the 10 µm droplet case would have a better distribution because it would vaporize quicker and achieve better mixing. However, for that very reason, the 10 µm droplet case has lower distribution because when it vaporizes, it begins to quickly mix into a homogeneous mixture before spark. In comparison, the 20 µm case does not have enough time before the spark to mix, giving it a greater distribution. Since less fuel vapor is seen, it suggests that a higher occurrence of wall impingement and less vaporization of the n-dodecane occurs at larger droplet sizes.

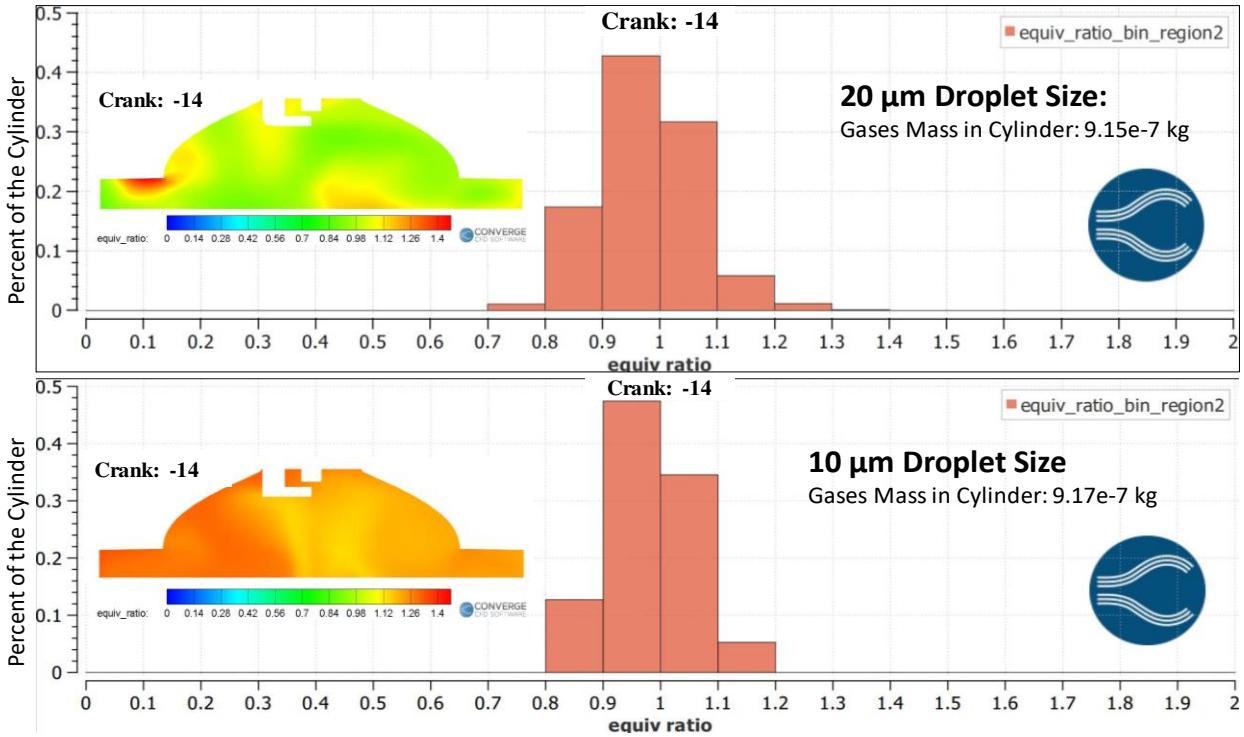

Figure 60: Equivalence ratio histogram for the cylinder at spark initiation with 8 kHz injections and 20µm diameter droplets (top) and equivalence ratio histogram for the cylinder at spark initiation with 8 kHz injections and 10µm diameter droplets (bottom). Also included are CFD images of slices centered in the cylinder of a two-stroke engine showing the distribution in equivalence ratio at spark timing

The motivation to have an excellent stratified distribution with the rich mixture in the dome region and leaner in the squish is because rich fuel mixture is more prone to auto-ignition. Figure 61 shows the 8 kHz injections (black dots) with the contour of equivalence ratio and velocity vectors mapped on it for a 20 µm droplet simulation.

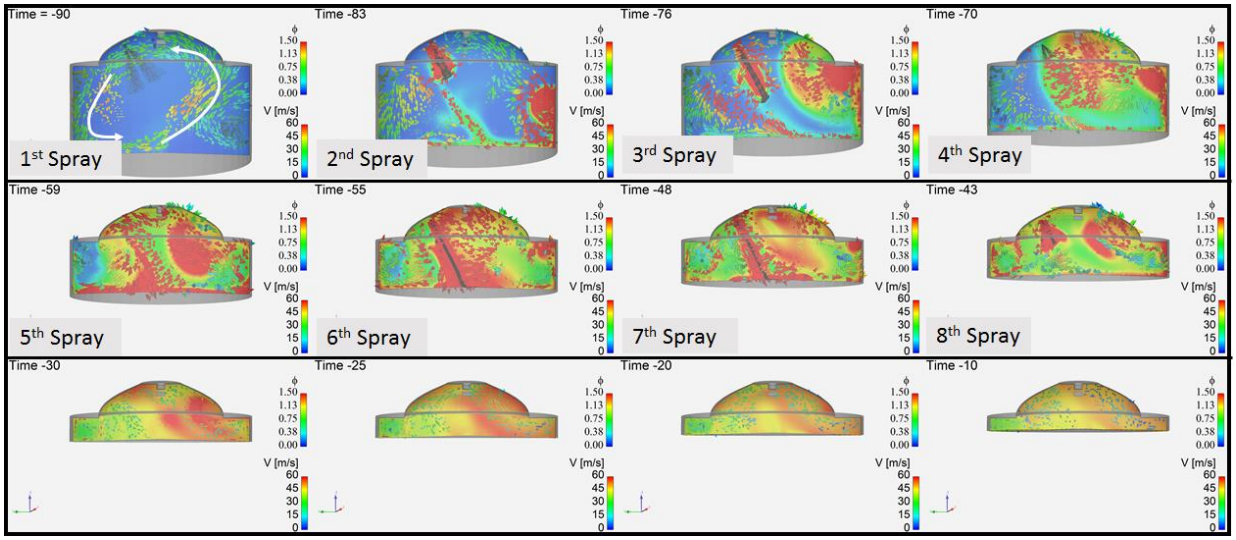

Figure 61 Contour of Equivalence Ratio, which is mapped with velocity vectors showing the development of the stratified distribution of fuel/air mixture

In Figure 61, the formation of a stratified mixture in the combustion chamber can be seen. In this injection strategy, though, the global equivalence ratio is 1.15, and the introduction of liquid n-dodecane is at a temperature of 62° C. The high-temperature introduction's primary motivation was to evaporate the complete liquid n-dodecane fuel and potentially see if the model can capture the low-temperature chemistry predominantly seen with n-dodecane fuel. However, this may be hotter than seen in the engine and will be a subject for future investigation if a more robust engine test cell is created (Phase II). A tumble circulatory flow caused the fuel to move around the domain and recirculate back near the electrode. This configuration helps during ignition as the mixture in the electrode gap is rich enough and will not result in a misfire. However, we see a rich mixture on one side of the squish region, which still results in heavy end gas auto-ignition, as seen by the heat release rate curves in Figure 62.

Interestingly, the knocking event's magnitude is less than in the premixed n-dodecane case when the fuel is introduced by way of a high-frequency spray into the combustion cylinder

despite all other conditions remaining the same. This is a positive outcome and suggests that an injection strategy could alleviate knocking of JP-8 in a spark ignited IC engine. Furthermore, the conditions tested here were aggressive, as iso-octane was shown to be on the verge of knocking (Figure 55). Running the engine at less severe/typical conditions will likely show more stable combustion and will be the subject to future investigation once the model can be better validated with experimental data. This will be the motivation behind the CFD tasks in Phase II of the project.

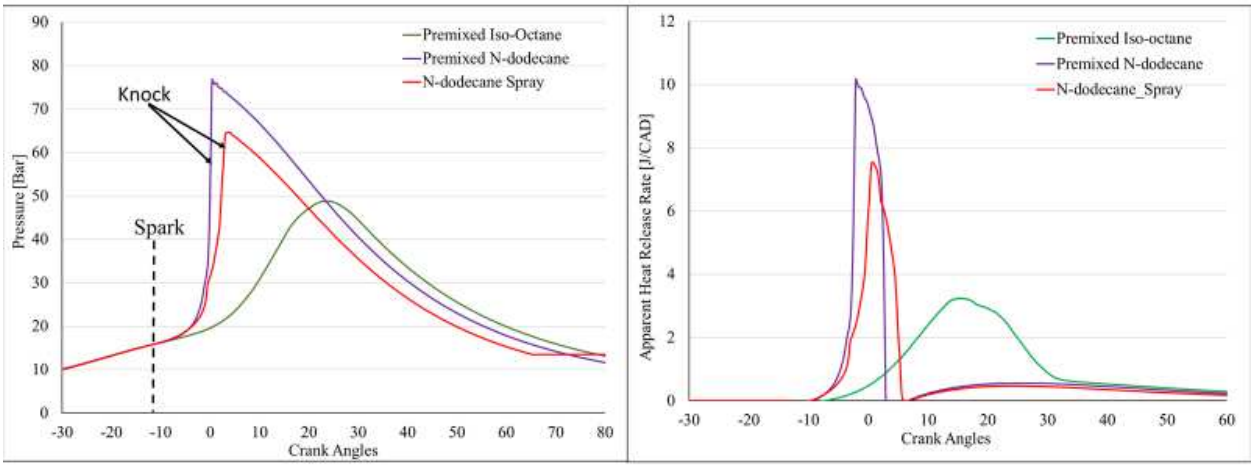

Figure 62 Simulation Pressure and Heat Release Rate for Premixed Iso-Octane, premixed n-dodecane and spray injection of n-dodecane

5.4 Manuscript Conclusion

In conclusion, this work is the first to report on a UAV engine's modeling, installing a direct injector in a traditional premixed system and the substitution of a heavy hydrocarbon fuel. The results show a comprehensive CFD model developed to simulate the combustion inside a small two-stroke 3w-28i UAV engine. In traditional carbureted operation, no-knock was seen while using iso-octane (gasoline surrogate). On the other hand, as expected, heavy knock is observed when n-dodecane (jet fuel surrogate) is used. The onset of end gas auto-ignition occurs in the squish region,

a region with high-temperature fuel stagnation. It should be carefully considered when attempting to develop an injection strategy to mitigate knock. A successful spray simulation helped to show that with a proper spray injection strategy, involving the location of the injector, correct mass, correct droplet size, correct timing, and the correct number of injections, there is a possibility to have optimized combustion. This is possible through fuel stratification, which can help achieve normal engine operations using heavy hydrocarbon fuels in a spark-ignited combustion model.

5.5 Future Work

Phase I of this project served as a proof of concept and made up most of the work presented. Phase II modeling tasks will first improve the model fidelity by tuning the simulations using improved engine test data with additional measurements of the intake and exhaust thermodynamic conditions taken from ideally a new engine test stand. However, a validated GT Power model with already obtained experimental data would be second best if not possible. Having a more constrained model with additional test data will enhance predictability. Once the model has been optimized, injector location, injection timing, fuel delivery rate shaping, and injection temperature will be explored through parametric studies to optimize stratified fuel distribution in the combustion chamber needed to achieve steady combustion with n-dodecane. Injection strategies will be constrained by the injector technology's range of capabilities and will explore early injection and late (post-combustion onset) injection strategies to target stable combustion. Also, since the intake and exhaust ports are crucial in a two-stroke engine, developing a more precise and better representation of the 3D model would only improve simulation validation. Knock was easily noticeable in these simulations because of the aggressive engine condition. However, as the model is validated and other engine conditions are investigated, it will be harder to distinguish when knock occurs. That is why developing or implementing a knock index would be an essential

next step. Another key numerical technique that should be investigated is a system or formula that numerically determines which injection design is better. The plan is to consider the knock index, engine performance, and the equivalence ratio's distribution/ location to achieve the ideal stratified combustion conditions.

Chapter 6: Conclusion

CAE tools, including CONVERGE CFD and GT Power, validated with experimental data, were used to investigate and inform the design of two energy conversion platforms when powered by non-traditional fuels. These simulation and modeling tools were used to ultimately identify strategies and geometrical designs to permit high-efficiency energy conversion of a dilute syngas-like fuel cell anode tail gas fuel in a gasified Kohler spark-ignited engine and the stable utilization of a high cetane jet propellant within a UAV two-stroke SI-ICE.

The first non-traditional fuel investigation was designing a JP-8 directed injected two-stroke UAV engine that traditionally was gasoline-powered. Through this research, the following key points were made:

- A baseline model was created in CONVERGE CFD to achieve the same peak pressure as a premixed stoichiometric gasoline-powered 3w-28i UAV engine at 6500 rpms and -13° ATDC sparking timing. The model was observed to be at borderline knock conditions.
- The baseline model was then altered to operate with a premixed JP-8 stoichiometric mixture, which leads to extreme knock occurring.
- The model was then altered to include a JP-8 spray injector to perform studies on four injection parameters: injection timing, injection quantity, amount of mass per injection, and droplet size. An injection rate shape of 8 kHz injections performed in 50 crank angles with equal mass each and 20 μm droplets was found to mitigate the engine knock observed for the premixed JP-8 case by controlling fuel stratification.

- It was found that more injections and larger droplet size improved the equivalence ratio distribution in the combustion chamber, thus leading to more stable combustion
- Future work will focus on validating a 3w-28i engine model to experimental data, investigating more injector parameters, and developing numerical techniques like a knock index and equivalence ratio stratification numerical technique to determine the optimal injection profile for a JP-8 powered UAV engine.

The second investigation explored the design of a SI engine (converted from a Kohler diesel engine) to operate off a highly dilute low calorific value fuel exhausted through the anode of a SOFC. The anode tail gas was first investigated with the CFR engine to better understand the fuel combustibility and provide model development for the subsequent gasified Kohler engine design. The key outcomes form this study and suggested future work are summarized here:

- Five single cycle cases were validated using the CFR engine's experimental data with two different anode tail-gas fuel blends that used dewpoint temperature to drop out water from the high dilute fuel blend (40° and 90° C fuel blend).
- The CFR engine model was able to detect knock in two validated cases, which was also present in the experimental data.
- The Kohler engine model was created from previous GT Power work to serve as a base case for engine design investigations. The baseline model had a CR17 piston bowl design with a speed of 1600 RPMS and a spark timing of -23° ATDC.
- Three spark plug configurations were investigated with the baseline model and the previous CR21 piston design, revealing that spark plug orientation can improve

performance and reduce COV by improving upon the flow characteristics at the spark plug.

- Multiple piston designs were investigated with the baseline model, revealing that smaller clearance height, larger squish areas, and larger bowl depths promote combustion and increase engine performance. Additionally, a further increase in engine performance could be achieved by merely rotating the piston slightly to decrease the squish area and spark plug distance. However, over-rotation would obstruct the intake valve and hinder engine performance.
- Through the knowledge learned in the piston investigations, a new piston design was developed at a lower CR of 14 to investigate the possibility of reducing backfiring and preignition conditions observed in experimental testing.
- Future work will develop better spark modeling techniques, improve heat transfer models, and validate the Kohler model using experimental data void of any backfires or pre-spark heat release.

References

[1] *U.S. Energy Information Administration - EIA - Independent Statistics and Analysis*. U.S. Energy Information administration, 2020.

[2] C. Goldenstein, *Advance Combustion Engines*. 2011.

[3] *Clean Air Act Text*. Environmental Protection Agency, 2017.

[4] *Summary of the Energy Policy Act*. Environmental Protection Agency, 2019.

[5] J. B. Heywood, *Internal combustion engine fundamentals*. New York : McGraw-Hill, [1988] ©1988, 1988.

[6] C. Y. A, M. A. Boles, and K. Mehmet, *Thermodynamics an engineering approach*. McGraw-Hill, 2020.

[7] P. Pal *et al.*, *Development of a Virtual CFR Engine Model for Knocking Combustion Analysis*. 2018.

[8] Z. Yue and S. Som, "Fuel property effects on knock propensity and thermal efficiency in a direct-injection spark-ignition engine," *Appl. Energy*, p. 114221, Nov. 2019, doi: 10.1016/j.apenergy.2019.114221.

[9] J. K. Ausserer, M. D. Polanka, P. J. Litke, and J. A. Baranski, "Experimental Investigation of Fuel Anti-Knock-Index Requirements in Three Small Two-Stroke Engines for Remotely Piloted Aircraft," *J. Eng. Gas Turbines Power*, vol. 141, no. 5, 2019, doi: 10.1115/1.4040520.

[10] C. Forte, E. Corti, G. M. Bianchi, S. Falfari, and S. Fantoni, “A RANS CFD 3D Methodology for the Evaluation of the Effects of Cycle By Cycle Variation on Knock Tendency of a High Performance Spark Ignition Engine,” Apr. 2014, doi: https://doi.org/10.4271/2014-01-1223.

[11] N. Demmons, “Project Proposal.”

[12] J. K. Ausserer, M. D. Polanka, P. J. Litke, and J. A. Baranski, “The Control Space for Knock Mitigation in Two-Stroke Engines for 1P 25 kg Remotely Piloted Aircraft,” *J. Eng. Gas Turbines Power-Trans. Asme*, vol. 141, p. 091010, 2019.

[13] S. O. B. Shrestha and G. Narayanan, “Landfill gas with hydrogen addition – A fuel for SI engines,” *Fuel*, vol. 87, no. 17, pp. 3616–3626, 2008, doi: https://doi.org/10.1016/j.fuel.2008.06.019.

[14] M. A. Devine, *Biogas Comes of Age*. Catepillar, 2013.

[15] J. Mann, L. Wilder, G. Zarus, and R. Nickel, *Landfill Gas Primer*. 2001.

[16] Z. Zhang, H. Zhang, T. Wang, and M. Jia, *Effects of tumble combined with EGR (exhaust gas recirculation) on the combustion and emissions in a spark ignition engine at part loads*, vol. 65. 2014.

[17] S. Gururaja Rao, S. H V, D. S., P. Paul, R. N K S, and H. Mukunda, “Development of producer gas engines,” *Proc. Inst. Mech. Eng. Part -J. Automob. Eng. - PROC INST MECH ENG -J AUTO*, vol. 219, pp. 423–438, 2005, doi: 10.1243/095440705X6596.

[18] U. Babu and L. Kumararaja, “A Research on Producer Gas in Internal Combustion Engines,” *Int. J. Recent Technol. Eng.*, vol. 8, no. 1S4, pp. 2277–3878, 2019.

[19] R. Chacartegui, M. Torres, D. Sánchez, F. Jiménez, A. Muñoz, and T. Sánchez, "Analysis of main gaseous emissions of heavy duty gas turbines burning several syngas fuels," *Fuel Process. Technol.*, vol. 92, no. 2, pp. 213–220, 2011, doi: https://doi.org/10.1016/j.fuproc.2010.03.014.

[20] U. Azimov, E. Tomita, N. Kawahara, and Y. Harada, "Effect of syngas composition on combustion and exhaust emission characteristics in a pilot-ignited dual-fuel engine operated in PREMIER combustion mode," *Int. J. Hydrog. Energy*, vol. 36, no. 18, pp. 11985–11996, 2011, doi: https://doi.org/10.1016/j.ijhydene.2011.04.192.

[21] C. Arcoumanis, Z. Hu, C. Vafidis, and J. H. Whitelaw, "Tumbling Motion: A Mechanism for Turbulence Enhancement in Spark-Ignition Engines," Feb. 1990, doi: https://doi.org/10.4271/900060.

[22] J. Liu and C. E. Dumitrescu, "Limitations of Natural Gas Lean Burn Spark Ignition Engines Derived From Compression Ignition Engines," *J. Energy Resour. Technol.*, vol. 142, no. 12, 2020, doi: 10.1115/1.4047404.

[23] M. Amann, T. Alger, B. Westmoreland, and A. Rothmaier, "The Effects of Piston Crevices and Injection Strategy on Low-Speed Pre-Ignition in Boosted SI Engines," Apr. 2012, doi: 10.4271/2012-01-1148.

[24] "High Performance Quick Reference Guide," *Fed. Mogul TEC*, [Online]. Available: https://www.gsparkplug.com/media/wysiwyg/technical-information/champion/High_Performance_Quick_Reference_Chart.pdf.

[25] P. R. Chitragar, K. Shivaprasad, and G. Kumar, "Use of hydrogen in internal combustion engines: A comprehensive study," *J. Mech. Eng.*, vol. 1, no. 3, pp. 84–96, 2016.

[26] "All About Spark Plugs," *Corolla Performance*. http://corollaperformance.com/TechInfo/sparkplugs.html.

[27] L. P. Tozzi, D. T. Lepley, M. E. Sotiropoulou, J. M. Lepley, and S. B. Pirko, "Time-varying spark current magnitude to improve spark plug performance and durability," Feb. 04, 2020.

[28] P. O. Witze, "The Effect of Spark Location on Combustion in a Variable-Swirl Engine," 1982, doi: 10.4271/820044.

[29] S. R. Turns, *An introduction to combustion: concepts and applications*, 3rd ed. New York: McGraw-Hill, 2012.

[30] M. C. Drake, T. D. Fansler, and A. M. Lippert, "Stratified-charge combustion: modeling and imaging of a spray-guided direct-injection spark-ignition engine," *Proc. Combust. Inst.*, vol. 30, no. 2, pp. 2683–2691, Jan. 2005, doi: 10.1016/j.proci.2004.07.028.

[31] W. Lucas, "Fuel Injectors," *Clemson Vehicular Electronics Laboratory: Fuel Injectors*, 2011. https://cecas.clemson.edu/cvel/auto/AuE835_Projects_2011/Lucas_project.html.

[32] J. Burgoyne and L. Cohen, "The effect of drop size on flame propagation in liquid aerosols," *Proc. R. Soc. Lond. Ser. Math. Phys. Sci.*, vol. 225, no. 1162, pp. 375–392, 1954.

[33] R. L. Fink and N. Jiang, "Electrostatic atomizing fuel injector using carbon nanotubes," Aug. 21, 2012.

[34] L. Bravo, M. Kurman, C. Kweon, S. Wijeyakulasuriya, and P. Senecal, "Lagrangian Modeling of Evaporating Sprays at Diesel Engine Conditions: Effects of Multi-Hole Injector

Nozzles With JP-8 Surrogates," ARMY RESEARCH LAB ABERDEEN PROVING GROUND MD VEHICLE TECHNOLOGY DIRECTORATE, 2014.

[35] *SOLIDWORKS 2018*. Dassault Systèmes Corporation, 2002.

[36] K. J. Richards, P. K. Senecal, and E. Pomraning, *CONVERGE*. Madison, WI: Convergent Science, 2020.

[37] T. Badawy, X. Bao, and H. Xu, "Impact of spark plug gap on flame kernel propagation and engine performance," *Appl. Energy*, vol. 191, p. 311–327, 2017, doi: 10.1016/j.apenergy.2017.01.059.

[38] C. Angelberger, T. Poinsot, and B. Delhay, "Improving Near-Wall Combustion and Wall Heat Transfer Modeling in SI Engine Computations," Oct. 1997, doi: https://doi.org/10.4271/972881.

[39] F. Berni, G. Cicalese, and S. Fontanesi, "A modified thermal wall function for the estimation of gas-to-wall heat fluxes in CFD in-cylinder simulations of high performance spark-ignition engines," *Appl. Therm. Eng.*, vol. 115, pp. 1045–1062, 2017, doi: https://doi.org/10.1016/j.applthermaleng.2017.01.055.

[40] A. Dayal, M. Shrivastava, R. Upadhyaya, and L. S. Brar, "Numerical study using detailed chemistry combustion comparing effects of wall heat transfer models for compression ignition diesel engine," *SN Appl. Sci.*, vol. 1, no. 9, p. 1005, Aug. 2019, doi: 10.1007/s42452-019-1033-z.

[41] X. Yang, A. Solomon, and T. Kuo, "Ignition and Combustion Simulations of Spray-Guided SIDI Engine using Arrhenius Combustion with Spark-Energy Deposition Model," *SAE Tech. Pap.*, Apr. 2012, doi: 10.4271/2012-01-0147.

[42] *EnSight 2019 R1*. Ansys, 2020.

[43] V. V. Krishnan, "Recent developments in metal-supported solid oxide fuel cells," *WIREs Energy Environ.*, vol. 6, no. 5, p. e246, Sep. 2017, doi: 10.1002/wene.246.

[44] R. J. Braun *et al.*, "Development of a Novel High Efficiency, Low Cost Hybrid SOFC/Internal Combustion Engine Power Generator," *ECS Trans.*, vol. 91, no. 1, pp. 355–360, Jul. 2019, doi: 10.1149/09101.0355ecst.

[45] A. Balu, "Analysis of Simulated Dilute Anode Tail-Gas Combustion Characteristics on a CFR Engine," MS Thesis, Colorado State University, 2020.

[46] "The San Diego Mechanism," *Chemical Mechanism: Combustion Research Group at UC San Diego*. http://web.eng.ucsd.edu/mae/groups/combustion/mechanism.html.

[47] "GRI Mechanism," *GRI-Mech Home Page*. http://combustion.berkeley.edu/gri-mech/.

[48] Y. Zhang, O. Mathieu, E. L. Petersen, G. Bourque, and H. J. Curran, "Assessing the predictions of a NOx kinetic mechanism on recent hydrogen and syngas experimental data," *Combust. Flame*, vol. 182, pp. 122–141, Aug. 2017, doi: 10.1016/j.combustflame.2017.03.019.

[49] G. Padhi, "Modelling and Simulation of Combustion of Dilute Syngas Fuels in a CFR Engine," MS Thesis, Colorado State University, 2019.

[50] Z. Yue, K. Edwards, S. Sluder, and S. Som, "Prediction of Cyclic Variability and Knock-Limited Spark Advance (KLSA) in Spark-Ignition (SI) Engine," 2018, doi: 10.1115/ICEF2018-9605.

[51] M. Countie, “PREDICTIVE MODELING AND TESTING OF A DIESEL DERIVED SOLID OXIDE FUEL CELL TAIL GAS SPARK-IGNITION ENGINE,” MS Thesis, Colorado State University, 2020.

[52] P. Hoy, “The World’s Biggest Fuel Consumer,” *Forbes Media, LLC*, Jun. 05, 2008.

[53] R. K. Garrett, “Is a single fuel on the battlefield still a viable option. Research report, August 1992-April 1993,” 1993.

[54] M. Le Pera, “The reality of the single-fuel concept,” *Army Logist.*, vol. 37, no. 2, pp. 41–43, 2005.

[55] G. Fernandes, J. Fuschetto, Z. Filipi, D. Assanis, and H. McKee, “Impact of military JP-8 fuel on heavy-duty diesel engine performance and emissions,” vol. 221, Aug. 2007, doi: 10.1243/09544070JAUTO211.

[56] S. Brown, “Design and Optimization of a 1kW Hybrid Powertrain for Unmanned Aerial Vehicles,” Oregon State University, 2017.

[57] “3W-28i Classic 3W-28i 3W 01 : Classic : Aircraft International.” www.aircraftinternational.com/Home/ProductDetailsMotor/tabid/130/ProdID/12/RtnTab/83/PageIndex/1/CatID/85/Default.aspx.

[58] Y.-D. Liu, M. Jia, M.-Z. Xie, and B. Pang, “Enhancement on a Skeletal Kinetic Model for Primary Reference Fuel Oxidation by Using a Semidecoupling Methodology,” *Energy Fuels*, vol. 26, no. 12, pp. 7069–7083, Dec. 2012, doi: 10.1021/ef301242b.

[59] T. Yao, Y. Pei, B.-J. Zhong, S. Som, T. Lu, and K. H. Luo, “A compact skeletal mechanism for n-dodecane with optimized semi-global low-temperature chemistry for diesel engine simulations,” *Fuel*, vol. 191, pp. 339–349, Mar. 2017, doi: 10.1016/j.fuel.2016.11.083.

[60] E. Ranzi, A. Frassoldati, A. Stagni, M. Pelucchi, A. Cuoci, and T. Faravelli, “Reduced Kinetic Schemes of Complex Reaction Systems: Fossil and Biomass-Derived Transportation Fuels,” *Int. J. Chem. Kinet.*, vol. 46, pp. 512–542, 2014.

[61] H. Wang, D. DelVescovo, Z. Zheng, M. Yao, and R. D. Reitz, “Reaction Mechanisms and HCCI Combustion Processes of Mixtures of n-Heptane and the Butanols,” *Front. Mech. Eng.*, vol. 1, p. 3, 2015, doi: 10.3389/fmech.2015.00003.

[62] J. T. Edwards, “Reference Jet Fuels for Combustion Testing,” 2017.

[63] *E-TEC Engine Technology for Ski-Doo Snowmobiles*. 2011.

Appendix

Equations (A1) - (A10) are Turn's Mechanism equations used to calculate the chemical kinetic values for SAGE combustion solver in CONVERGE CFD. [29]

$$\sum_{m=1}^{M} V'_{m,r} X_m \leftrightarrow \sum_{m=1}^{M} V''_{m,r} X_m \tag{A1}$$

$$\dot{w}_m = \sum_{r=1}^{R} V_{m,r} q_r \tag{A2}$$

$$V_{m,r} = V''_{m,r} + V'_{m,r} \tag{A3}$$

$$q_r = k_{fr} \prod_{m=1}^{M} [x_m]^{V'_{m,r}} - k_{rr} \prod_{m=1}^{M} [x_m]^{V''_{m,r}} \tag{A4}$$

$$k_{fr} = A_r T^b e^{\left(-\frac{E_r}{R_u T}\right)} \tag{A5}$$

$$k_{rr} = \frac{k_{fr}}{k_{cr}} \tag{A6}$$

$$k_{cr} = k_{pr} \left[\frac{P_{atm}}{RT}\right]^{\Sigma_{m=1}^{M} V_{m,r}} \tag{A7}$$

$$k_{pr} = e^{\left(\frac{\Delta S_r^\circ}{R} - \frac{\Delta H_r^\circ}{RT}\right)} \tag{A8}$$

$$\frac{\Delta S_r^\circ}{R} = \sum_{m=1}^{M} V_{m,r} \frac{S_m^\circ}{R} \tag{A9}$$

$$\frac{\Delta H_r^\circ}{RT} = \sum_{m=1}^{M} V_{m,r} \frac{H_m^\circ}{RT} \tag{A10}$$